ABSTRACT

BYRNS, BRANDON RAYE. Design and Characterization of a Coaxial VHF Plasma Source for Use in Atmospheric Applications. (Under the direction of Steve Shannon).

Plasma discharges have been used for a wide variety of applications for many years, including semiconductor and integrated circuit manufacturing, textile treatment, and surface modification. Plasmas provide a mechanism for developing novel chemistries that allow for material processing that cannot be achieved by any other known method. Atmospheric plasmas have opened up many new applications of research in industry as the need for applications that cannot be performed in vacuum chambers are being realized. In this work a coaxially driven VHF plasma source for atmospheric air plasmas has been built and characterized. Electrical and optical characterization of this source present a unique operating regime when compared to state of the art atmospheric systems such as dielectric barrier discharge, pulsed dc, microwave, or ac blown arc discharges. This is achieved via a VHF ballasting affect where the high drive frequency used prevents an arc from forming by creating a negative feedback loop where plasma resistance increases with increasing electron density. Diagnostics used include optical emission spectroscopy, B-loop probe, and impedance measurements. Optical emission characterization allows for determination of species present in the plasma as well as gas temperature measurements using peaks from the emissions of OH. Impedance measurements are used to calculated plasma impedance due to the simple structure of the device, which is used for electron density and sheath thickness calculations.

Several applications are investigated in this work including water treatment and material surface treatment. For water treatment the NO_x species formed in the plasma are absorbed in the water allowing for significant levels of nitrate and nitrite in solution. Using this as a means to produce an on demand water based fertilizer is shown to produce observable results although at a significant energy cost. The removal of harmful chemicals from water streams is also examined by testing the removal efficiencies for two different compounds: 1,4-dioxane and PFOS. Mixed results are seen as dioxane is removed while PFOS experiments show very little effective reduction in concentration. Material processing is performed on paint samples from US Navy battleships. Paint removal is achieved, but the

mechanism for removing paint material is physical and not based on the unique chemistry in the plasma. In order to scale applications for further development, a design to run two plasma sources in parallel is achieved with a similar array of diagnostics used for characterization.

© Copyright 2014 Brandon Byrns

All Rights Reserved

Design and Characterization of a Coaxial VHF Plasma Source for use in Atmospheric Applications

by
Brandon Raye Byrns

A dissertation submitted to the Graduate Faculty of
North Carolina State University
in partial fulfillment of the
requirements for the degree of
Doctor of Philosophy

Nuclear Engineering

Raleigh, North Carolina

2014

APPROVED BY:

_____	_____
Steven Shannon Committee Chair	Mohamed Bourham
_____	_____
John Gilligan	Griff Bilbro

DEDICATION

To my family.

BIOGRAPHY

Brandon Raye Byrns was born in Mt Juliet, TN on January 16 1987. He attended the University of Tennessee Knoxville, where he received a Bachelor of Science in Engineering Physics in 2009. He joined North Carolinas State University's Nuclear Engineering program in the fall of 2009.

ACKNOWLEDGMENTS

I would like to thank my advisor, Steve Shannon, for all the help and guidance for this work both academically and personally. Also to Rick and Terry and all the other staff in the NCSU Precision Machine Shop for assisting in building and modifications needed, even when we need things ASAP. To my friends and family for all of their support and keeping me sane throughout the last few years, Thank you.

TABLE OF CONTENTS

LIST OF TABLES vii
LIST OF FIGURES viii
Chapter 1: Introduction 1

Chapter 2: Background 5
2.1 Plasma 5
2.2 Water Treatment 12
2.2.1 Nitrogen Fixation 12
2.2.2 1,4-Dioxane 13
2.2.3 Perfluorooctanesulfonic Acid (PFOS) 14
2.3 Paint Removal from Surface 15

Chapter 3: Source Design 17
3.1 Coaxial Device Circuit 18
3.2 Plasma Equivalent Circuit 20
3.2.1 Collision Frequency 21
3.2.2 Reactive Components 23
3.3 VHF Ballasting 25

Chapter 4: Plasma Characterization 29
4.1 Optical Emission Spectroscopy 29
4.1.1 Experimental Setup 31
4.1.2 Gas Identification 32
4.2 Gas Temperature Measurements 39
4.2.1 Experiment 42
4.2.2 Spatially Resolved Rotational Temperatures 46
4.3 Electrode Damage 51
4.4 Electrical Measurements 53
4.4.1 Validation of the Model 54
4.4.2 Plasma Impedance Measurements 56
4.4.3 Electron Density and Sheath Thickness Calculation 67
4.4.4 B-Loop Probe 71
4.5 RF Matching Network 73
4.5.1 Q-Value 73

Chapter 5: Simultaneous Operation of Multiple Devices 82
5.1 Parallel Combination of Sources 82
5.2 Frequency Response of Devices 85
5.2.1 Multiple Device Frequency Response 87
5.2.2 Multiple Device Plasma Testing 91
5.3 Electron Density Calculation 95
5.4 Comparison to Data from Single Device 96
5.5 OES 97

5.5.1 OH Temperature Measurement....99
5.6 Conclusions....101

Chapter 6: Applications....102
6.1 Water Treatment....102
6.1.1 Plasma-Water Characteristics....104
6.1.2 Nitrogen....106
6.1.3 Fertigation....116
6.2 Chemical Removal....123
6.2.1 1,4-Dioxane....124
6.2.2 PFOS....127
6.3 Surface Treatment....129
6.3.1 Paint Removal....129
6.3.2 HDPE Removal....130
6.3.3 Paint Samples....133

Chapter 7: Conclusions and Future Work....144

REFERENCES....148

LIST OF TABLES

Table 2.1 Comparison of Different Types of Plasmas 11

Table 4.1 Comparison of Network Analyzer Data and Calculated Model Data 55

Table 4.2 Impedances Measurements at Generator Input for a Variety of Gases 60

Table 4.3 Calculated Plasma Impedances for different Gases 66

Table 5.1 Calculated Lengths for Series and Shunt Legs For Optimum Dual System Impedance Matching 84

Table 5.2 VNA Data for both Individual Devices 86

Table 5.3 VNA Data for Dual Sources Compared With Corresponding Model Data 88

Table 5.4 Impedances and Electron Densities Calculated with Dual Sources 96

Table 5.5 P/R branch Ratio for Each Device 100

Table 6.1 Flow Rate for Each Type of Stream Type from Sprayer 116

Table 6.2 Effects of the Addition of Baking Soda at Different Times 117

Table 6.3 Summary of PFOS Degradation Experiments 129

LIST OF FIGURES

Figure 1.1: a) Photograph of Assembly b) Image Down Barrel of 500W Air Discharge 2
Figure 2.1: Plasma Density and Temperature for Various Types of Plasmas 6
Figure 2.2: Typical Schematic for a DBD; (1) metal electrodes, (2) dielectric barrier. Taken from Shutze [10] 8
Figure 2.3: Schematic of a Typical Corona Discharge. Taken from Shutze [10] 9
Figure 2.4: Schematic of a transferred arc device. Taken from [Shutze 10] 10
Figure 2.5: Typical Schematic of Atmospheric pressure plasma jet. Taken from Shutze [10] 11
Figure 3.1: Diagram of Atmospheric Source 17
Figure 3.2: Circuit Representation of Plasma 20
Figure 3.3: Plasma Resistance vs. Electron Density 26
Figure 3.4: Comparison of Low Frequency vs. High Frequency Response to Density Perturbations 27
Figure 3.5: Frequency Dependence of the Ballasting Effect 28
Figure 4.1: Diagram of OES Experiment 31
Figure 4.2: Normalized Spectra for Air Plasma for Different Powers 32
Figure 4.3: Air Emission Spectra 33
Figure 4.4: Spectroscopy Data for Multiple Flow Rates 34
Figure 4.5: Normalize Spectra for Flow Rate Sweep 34
Figure 4.6: Carbon Dioxide Emission Spectra 36
Figure 4.7: Nitrogen Emission Spectrum 37
Figure 4.8: Helium Spectra 37
Figure 4.9: Argon Spectra 38
Figure 4.10: Argon Plasma; a.) Full Plasma Photo b.) Close up of the Patter formed on the Electrode 39
Figure 4.11: Ratio of P and R branches vs. Rotational Temperature (Laux) 40
Figure 4.12: Optical thickness times water vapor mole fraction that would result in 4% self-absorption of P-branch peak (Laux) 41

Figure 4.13: Power Sweep of the Gas Temperature Spectroscopy Measurements for 3.5 scfm 43
Figure 4.14: Raw Spectroscopic Data Normalized to the P-branch 44
Figure 4.15: Rotation Temperature vs. Input Power for 3.5 scfm 45
Figure 4.16: Rotational Temperature vs. Calculated Electron Density 45
Figure 4.17: Rotational Temperature vs. Power for multiple air flow rates 46
Figure 4.18: Experimental setup for Spatially Resolved Temperature Measurements 47
Figure 4.19: Spatial OH Temperature Measurement Spectra 49
Figure 4.20: Spatially Resolved Temperature Measurements for 490W 49
Figure 4.21: Spatially Resolved Spectroscopy Data 50
Figure 4.22: Normalized Spatially Resolved Spectra 51
Figure 4.23: Damage Occurring on the Surface of the Electrode after Sustained Operation with High Delivered Power 52
Figure 4.24: Spectrum for Plasma When Electrode is Damaged 53
Figure 4.25: Resonant Frequency Changes with Series and Shunt lengths 56
Figure 4.26: Illustration of how the Impedance is Calculated Down the Device 57
Figure 4.27: Comparison of Experimental and Model Generator Impedances for Air 62
Figure 4.28: Comparison of Experimental and Model Generator Impedances for CO_2 63
Figure 4.29: Comparison of Experimental and Model Generator Impedances for He 64
Figure 4.30: Comparison of Experimental and Model Generator Impedances for Nitrogen . 65
Figure 4.31: Electron Density vs. Delivered Power for All Gases 68
Figure 4.32: Plasma Resistance Vs Electron Density for Air and Nitrogen 69
Figure 4.33: Plasma Resistance vs. Electron Density for He and CO_2 70
Figure 4.34: Plama Reactance vs. Electron Density for Air and Nitrogen 70
Figure 4.35: Plasma Reactance vs. Electron Density for He and CO_2 71
Figure 4.36: Oscilloscope Data Taken With B-loop Probe 72
Figure 4.37: Device Electrical Response without Plasma for Different Q Values of the System 74
Figure 4.38: Illustration for the Changing of the Lengths of the Series and Shunt Segments 75

Figure 4.39: Comparison of the Q value of the circuit with Delivered Power and Electron Density 76
Figure 4.40: Cross Sectional Cut Showing Diameters of Inner and Outer Conductors 76
Figure 4.41: Reflection Coefficient vs. Electron Density for Various Device Characteristic Impedances 77
Figure 4.42: Illustration of Change in Electrode Size 77
Figure 4.43: Response of Device with Changing Electrode Diameter Assuming Plasma Diameter Changes Accordingly 79
Figure 4.44: Response of Device with Changing Electrode Diameter Assuming Plasma Diameter Remains Constant 79
Figure 4.45: Reflection Coefficient vs. Collision Frequency for Different Q values 81
Figure 4.46: Q Value vs. Relative Polarizability 81
Figure 5.1: Frequency Response of Device with Different Ground Plate Resistances 86
Figure 5.2: Comparing Single Devices and Dual Devices 89
Figure 5.3: Comparing Single and Dual Devices with Different Series Lengths 89
Figure 5.4: Comparison of Frequency Response with Small Change in Shunt Length 91
Figure 5.5: Image of the Dual Sources in Operation 92
Figure 5.6: Resistance and Reactance of Initial Duel Source Setup 93
Figure 5.7: Impedances of Dual Sources for Two Different Lengths Compared to Model Data 94
Figure 5.8: Comparison of Electron Densities for Single and Dual Sources 97
Figure 5.9: Simultaneous Spectra for Each Device with Air as the Feed gas 98
Figure 5.10: OH Temperature Measurements for Device #1 99
Figure 5.11: OH Temperature Measurements for Device #2 100
Figure 6.1: Plasma Water Treatment. 104
Figure 6.2: OES Data for Plasma Treatment of Water Surface at 500W 4scfm 105
Figure 6.3: Nitrate and Nitrite Production with Input Power 107
Figure 6.4: Nitrate and Nitrite Production with Input Power for Distilled Water 108
Figure 6.5: Nitrate Concentration with Air Flow Rate 109

Figure 6.6: Schematic of Electrode Nozzle Design 110
Figure 6.7: Setup for Spraying Water through the Plasma 111
Figure 6.8: Power Sweep of Nitrogen Concentration for Tap and Distilled Water at 3 scfm and Stream 2 113
Figure 6.9: How Water Stream Effect Nitrogen Concentration 113
Figure 6.10: Effects of Number of Passes through Plasma on Nitrogen Concentration..... 114
Figure 6.11: Effect of Flow Rate on Nitrogen Concentration 115
Figure 6.12: Effect of Delaying the Addition of Baking Soda to Treated Water 119
Figure 6.13: Plants During the Growth Phase: PP (top), CP (left), PP (right) 120
Figure 6.14: Comparison of Plant Sizes Between the Experimental Groups 121
Figure 6.15: Average Shoot Mass for Each Plant Type and Group..... 122
Figure 6.16: Average Root Mass for Each Plant Type and Group 122
Figure 6.17: Dioxane Concentration after Air Plasma Treatment 125
Figure 6.18: Percent of Dioxane Remaining after Treatment for Air and Argon Plasmas... 126
Figure 6.19: Paint Samples Exposed to Plasma..... 133
Figure 6.20: Cross Sectional Representation of Plasma Treatment of Sample 135
Figure 6.21: Removal Rate of Paint as a Function of Power for Different Gases 136
Figure 6.22: Removal Rates for Nitrogen for Various Distances between the Plate and the End of Device 138
Figure 6.23: Removal Rate for Air for Multiple Distances between Plate and Device..... 138
Figure 6.24: Removal Rate for Air at 4.5 scfm with pt=0.76cm and Multiple et Distances 139
Figure 6.25: Removal Rate vs. Total Distance between Electrode and Sample..... 140
Figure 6.26: Removal Rate for Air with Varying Flow Rate 141
Figure 6.27: Removal Rate vs. Plate Movement Speed..... 142

Chapter 1: Introduction

Plasma discharges have been used for a wide variety of applications for many years, including semiconductor and integrated circuit manufacturing, textile treatment, and surface modification. Plasmas provide a mechanism for developing novel chemistries that allow for material processing that cannot be achieved by any other known method. Atmospheric plasma discharges have opened up a new world of applications for plasma enhanced modification of materials [1]. The absence of a vacuum system has reduced the overall cost of plasma application systems and the ability to run at ambient pressure has enabled the treatment of materials that could not withstand these vacuum conditions. Medical applications such as sterilization [2, 3], wound treatment [4] and surgical instrumentation [5] are some of the fastest growing plasma applications and have been largely enabled by advances in atmospheric source technology. In addition to medical applications, surface treatments of soft materials and liquids [6], and plasma modification of large scale systems (such as plasma removal of paint and coatings on vehicles and other large structures) [7] are only a sampling of the applications that now have a practical pathway via atmospheric plasma systems.

Atmospheric plasmas have large potential to improve many current processes, in both cost and speed. This helps to drive the development of new plasma sources that can perform well in various applications. The device designed in this dissertation also comes from this goal. While applications help to push new ideas, new plasma sources must be understood as completely as possible to improve their performance. For this device a generator was supplied and a simple structure was developed to ignite an atmospheric air plasma. It turns out that the operating frequency of the device plays an integral part in sustaining this plasma without the presence of arc, that allows for many potential applications where arc power densities are too high for sustained operation.

Figure 1.1 shows an image of both the assembly and the plasma in operation. This give an idea of the size of the device as the diameter of the tube is 5.1cm. With the design of

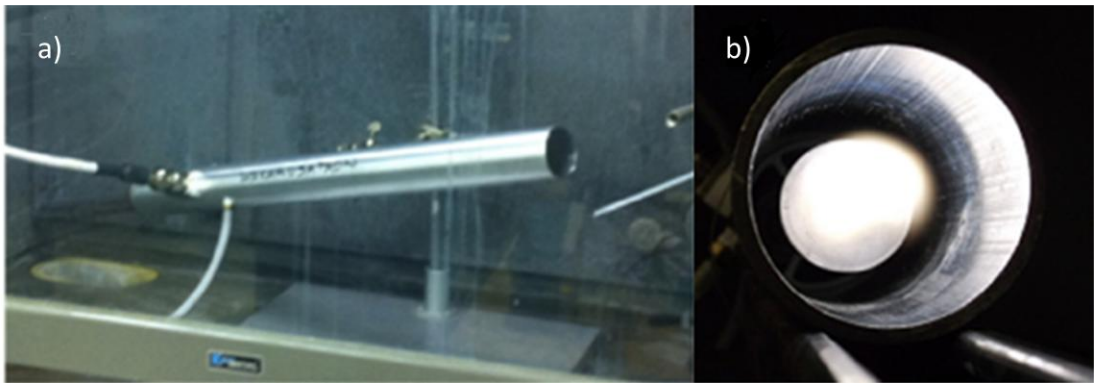

Figure 1.1: a) Photograph of Assembly b) Image Down Barrel of 500W Air Discharge

the device, there are many applications that can be addressed as the plasma is able to extend out of the barrel to come into contact with different materials

This work begins by giving a brief overview of plasmas in general. This includes a more detailed discussion on several different types of atmospheric plasmas that are currently used today. These include plasma torches, corona, dielectric barrier discharge (DBD), gliding arc, and plasma jet. A comparison of the important plasma properties such as power density, electron density and temperature between these sources and the one designed in this work are also discussed. A brief overview of the important background information for each of the applications is also presented.

This work discusses both the design process for the development of this source as well as the characterization of the plasma through the use of various diagnostics. Chapter 3 goes into detail about the physical and electrical design of the source. The physical design of the device is based simply on transmission line theory, where the coaxially design of the device acts as transmission lines that allow for optimum delivery of power. This is achieved by having the lengths of the device be on the order of the quarter wavelength for 162MHz. An equivalent circuit model for the plasma is presented that is simple and has been used for many different plasmas, both atmospheric and vacuum. The equivalent circuit of the plasma provides a pathway to sustaining the plasma without transitioning to a thermal arc due to the effects of the operating frequency of the device. This provides a negative feedback which is

referred to as VHF Ballasting. The effect causes the plasma resistance to increase with increasing electron density that acts to prevent the electron density from continually increasing to the point that an arc is created in the discharge.

Chapter 4 discusses the various diagnostics used in the characterization of the plasma. Two main diagnostic techniques are used: Optical emission spectroscopy (OES) and impedance measurements. Gas identification is one major use for OES. Through the comparison of the light emitted by a plasma to both molecular and atomic emissions of the molecules and atoms that could exist, based on the feed gas used, the species present in the plasma can be identified. In the case of an air plasma, OH is one of the most prominent peaks in the spectra. This has led to efforts to use the plasma in water treatments as OH is a highly reactive molecule that is used for the degradation of many chemicals. OES is also used to make estimates for the gas temperature of the plasma. This is done specifically in this work by looking at the ratio of two peaks emitted by the OH molecule. These measurements have resulted in gas kinetic temperatures ranging from 3000-5000K. Electrical measurements were performed to obtain the plasma impedance and from this the electron density of the discharge. Impedance measurements are made at the output of the generator, and due to the simple design of the device this value can readily be used to calculate the plasma impedance. Then, using the equivalent circuit the electron densities are found to be in the ranges of 10^{11}-10^{13} cm^{-3} for all the gases used. Measurements using a simple B-loop probe were done to ensure that the discharge is free from streamers or arcs as the current picked up from the magnetic fields was free from any spurious spikes.

After characterization of the plasma has been done the next step to improving the device is to determine its scalability. This is especially important for applications where a large amount of material must be processed. This is discussed in chapter 5 as the design and operation of two sources in parallel is discussed. Two identical devices are built and connected to the generator in parallel. Power delivered from the generator is doubled to account for the extra device. A system with two different plasma sources is successfully built and then characterized using the same set of diagnostics used for the characterization of the single device. Similar quantities for both electron density and gas temperature were

measured for the two device system and the single device. The development of the parallels sources indicate that these devices could be set up to have even more devices running simultaneously. The major constraining point would be the total amount of power that can be output by the generator and the desired input power into each device. With the current generator with an output power of 3.5kW, a total of 7 devices could potentially be operated at once with delivered power to each device of ~500W. This development is essential for the further development of the device for various applications.

Two main types of applications are discussed in this work including surface treatment of materials and the treatment of water. Water treatment is unique to atmospheric plasmas due to the constraints of low pressure plasmas. A huge industry stems from removing chemicals out of waste water before allowing it to be discharged back into the environment. With the unique chemistries present in plasmas, and the role of water chemistry in these processes the potential for applications is extremely large. For this work both the degradation of pollutants 1-4 dioxane and PFOS are examined as well as the process of nitrogen fixation in water to be used as fertilizer. In this work is shown that 1,4-dioxane can be removed from water samples after exposure to the plasma. Also it is shown that the production of fertilizer in water is also achieved through air plasma exposure to water. An experiment to test the effectiveness of the plasma treated water as fertilizer was conducted that showed up to an 80% increase in the dry weight of the plants material above ground. Experiments are also done to test methods to improve efficiency in both nitrogen fixation in water as well as degradation of compounds in water. Surface treatment applications are focused on removal of material here, with a focus on the removal of paint from metal surfaces such as naval ships. It is shown that material can be removed from the surface when exposed to the plasma but it was determined that this removal was due to physical processes instead of chemical reactions created by the plasma. There are also many other opportunities that atmospheric plasmas could be used for in surface modification.

Chapter 2: Background

The previous chapter gives a small introduction to the type of plasma being utilized in this work. It also introduces some of the applications that have been attempted with this device. This chapter focuses on the differences between the plasma generated here versus existing plasma systems. It also goes into some detail about the existing technology for some of the applications that have been experimented with this device.

2.1 Plasma

Plasmas are defined as an ionized gas consisting of charged and neutral particles that are in a quasineutral state. Another important distinction is the existence of collective motion due to the ionization of the gas. As there is always going to be some amount of ionized particles in a gas, the difference in a plasma is that the number ionized particles is large enough to have an effect on the overall behavior of the plasma. Quasineutrality assumes that the plasma is large enough so that any localized grouping of charge is screened out by competing charges. This screening results in the bulk of the plasma being free from any large potentials or fields [8].

Two main parameters to characterize plasmas are the charged particle density and the temperature of the plasma. Plasmas can vastly range in both density and temperature as shown in Figure 2.1. Sizes of plasmas also can vary extremely large amounts as plasmas developed in the lab can be as small as a micron, 10^{-6}m, they can also be the size of intergalactic nebulae on the order of 10^{25}m

Advances in the application of atmospheric plasmas have come primarily from the development of a broad array of source technologies that seek to maintain the unique conditions found in a non-equilibrium plasma at higher pressures. Atmospheric plasmas are driven at a wide range of frequencies ranging from dc to GHz. Most rely on either sustained arc-type discharges such as plasma torches [9], periodic breakdown to afterglow formation such as plasma jets [10, 11], dielectric barrier discharges (DBDs) [12], ion trapping [13], or

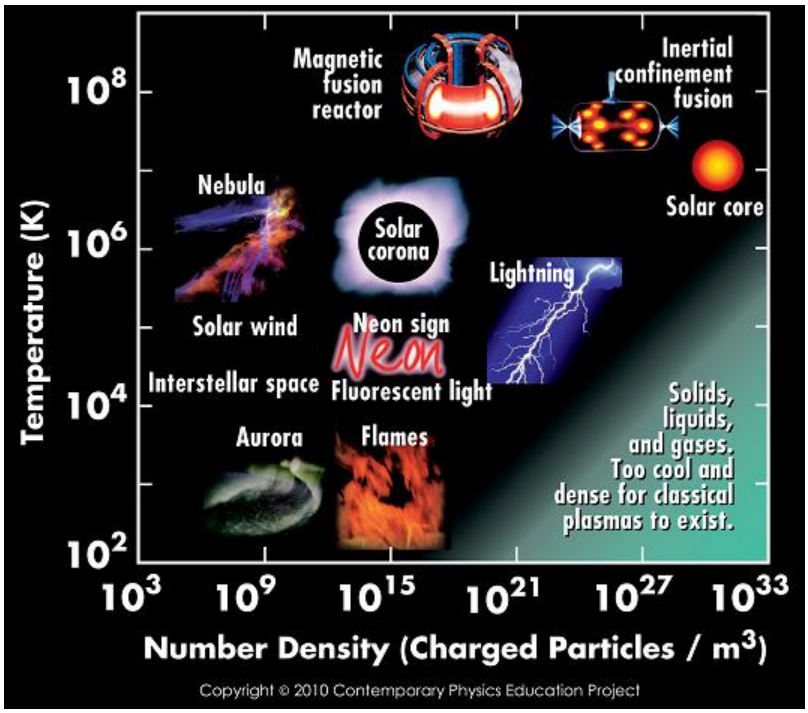

Figure 2.1: Plasma Density and Temperature for Various Types of Plasmas

wave heating systems such as microwave resonant cavity based plasma jets [14]. Many of these systems rely on helium [15] and its metastable states to sustain the discharge. One of the primary challenges in producing atmospheric plasmas with higher power densities has been the transition point between the formation of a glow or streamer dominated discharge to that of an arc discharge. Glows and streamers tend to operate under conditions that are not in thermal equilibrium, thereby providing the novel chemistries that have made atmospheric plasmas so compelling for an array of applications. As power density is increased, the stable operating regime of the plasma transitions from a nonequilibrium glow to an arc driven discharge. Under these conditions, the plasma tends to operate more in thermal equilibrium, presenting a very different interaction with surrounding material both chemically and energetically [16].

In order to push this transition to an arc driven discharge out to higher power densities, several strategies have been employed. The most common strategy is to provide

current isolation between surfaces of differing electrical potentials in order to mitigate arc formation via charge buildup and subsequent field reduction. This technique is most famously utilized in the class of atmospheric plasma sources referred to as DBDs, where a narrow gap parallel plate system with insulating layers over the plasma facing electrode surfaces generates glows and streamers at atmospheric pressure while preventing the transition to an arc discharge. Another strategy is to terminate the potential between surfaces prior to arc formation, thereby terminating the accelerating potential before an arc can form. These pulsed systems have generated a tremendous amount of interest, particularly in combustion and biomedical applications due to their non-equilibrium gas phase chemistries [17, 18] as well as their unique ability to propagate beyond the electrodes of the system via photoionization, forming what is commonly referred to as a 'plasma needle' or a 'plasma bullet' [19].

A third means for mitigating arc formation follows a similar strategy to these pulsed systems by minimizing parasitic electrical elements in the source design and modifying the potential between electrodes at a time scale much higher than the characteristic time for instabilities to manifest in the system; this is the mechanism that we seek to employ in the source detailed in this work. Electrical characterizations of atmospheric air discharges have measured instabilities timescales on the order of 200 ns, primarily due to ionization thermal instability [20]. By driving the plasma with an RF power source with a frequency that is much lower than this timescale, a mitigation pathway can be achieved that prevents the amplification of the instability to the point of arc formation, and thus loss of the discharge's non-equilibrium properties. In this dissertation, a coaxial plasma source driven at 162MHz is described in detail. Plasma sources that operate in this frequency range have had tremendous success, particularly in the area of material deposition and etching, where VHF systems have exhibited an increased ability to dissociate feed gases and generate higher electron densities and lower sheath potentials than their lower frequency counterparts; these sources have tended to operate at much lower pressures [21, 28]. This source employs a low loss, low-Q structure that provides power coupling to the plasma with minimal parasitic capacitance. The period of the RF drive (6 ns) is much shorter than the characteristic timescale for ionization

thermal instability. This structure presents an electrical pathway for instability mitigation by operating in a regime where the discharge resistance measured at the drive frequency increases with increasing electron density, thereby providing negative feedback to the system that mitigates the growth of this instability.

All of these types of atmospheric plasma vary significantly in terms of plasma characteristics and how the plasma is generated. Size is one huge difference between these plasmas. Most atmospheric DBD's tend to be very small and are considered micro discharges with sizes on the order of millimeters. Figure 2.2 shows a schematic for a typical DBD[10]. These can also have a wide varying electron density ranging from 10^{9}-10^{15}cm^{-3} [22,23]. DBD's are non thermal plasmas so they have a low gas temperature, typically on the order of 400K [24,26]. Electron temperatures have been shown to range from 1-10eV [29,25]. While DBD plasmas have a low gas temperature allowing for interaction with most surfaces, the discharges tend to be nonuniform. This limits the usefulness of the plasmas for material processing.

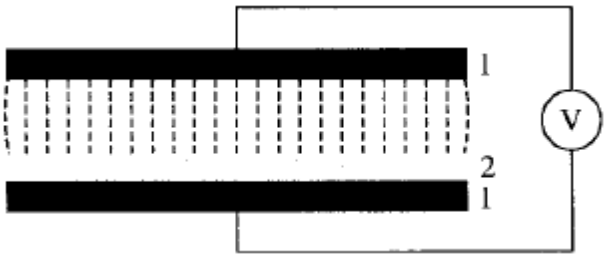

Figure 2.2: Typical Schematic for a DBD; (1) metal electrodes, (2) dielectric barrier. Taken from Shutze [10]

Corona discharges are formed around a point tip in which a highly nonuniform electric field exists. They are generated by applying a potential to a metal electrode that comes to a point some distance away from another plane electrode. Figure 2.3 is a schematic for a corona discharge system. Coronas are similar to DBD plasmas with low temperatures around 400K and with relatively low electron densities 10^{9}-10^{12}cm^{-3}. The plasma is usually

only in a small region of about 1 mm from the metal point while reactive species drift toward the planar electrode. The small area has prevented extensive use in materials processing although some arrays have been developed to improve this. Some Applications that corona discharges have been used for include activation of polymer surfaces and enhancement of SiO_2[30,31]. When oxygen is used for production of the plasma ozone is the dominant species, while atomic oxygen and its metastables are five to six orders of magnitude less [10].

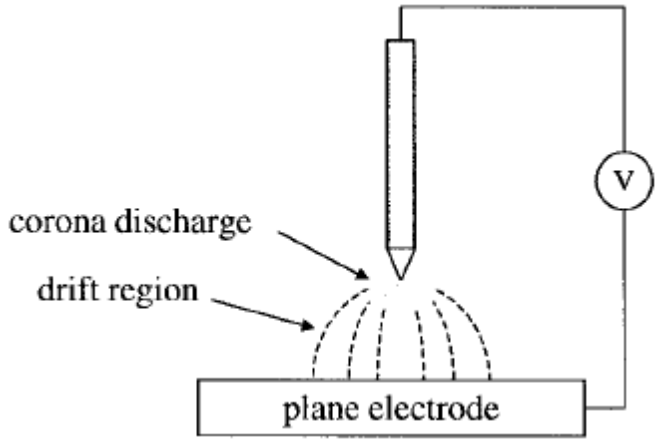

Figure 2.3: Schematic of a Typical Corona Discharge. Taken from Shutze [10]

Arc discharges are typically operated at high gas pressures. Transferred arcs are used to cut, melt and weld materials [32,33]. Figure 2.4 shows the typical schematic for a device generating this type of plasma. These plasma can be generated with high power DC or RF fields and result in high gas temperatures between 3000 and 20,000K. High gas flow rates are used to push the arc out of a nozzle at the end of the device for use in applications. Plasma torches are similar to this discharge but typically have some precursor injected into device to be used for applications such as thin film deposition[10]. Electron densities are typically very large on the order of $10^{17}cm^{-3}$ [34] Arc discharges tend to have very high energy density of about 1kW/cm[27].

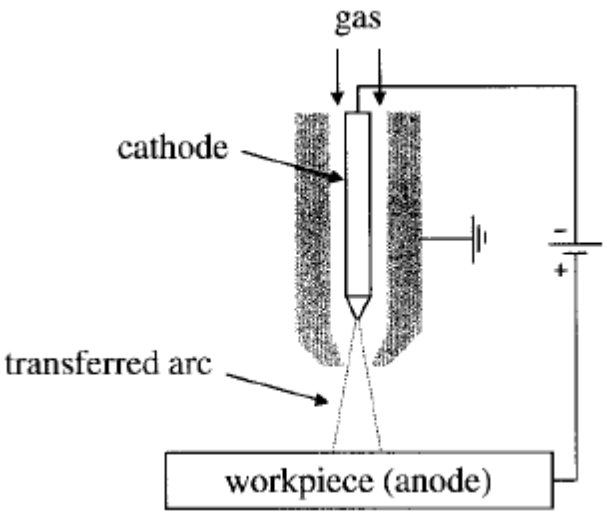

Figure 2.4: Schematic of a transferred arc device. Taken from [Shutze 10]

Another atmospheric source type is the plasma jet. It consists of concentric electrodes that create a discharge with a mixture of helium, oxygen and other gases[35]. RF power is typically used and applied to the inner electrode ionizing the gas inside the device. Gas flowing through the device then emits the plasm jet through the nozzle. Electron densities outside of the jet are relatively low and have been measured to be about $10^{10}cm^{-3}$. This is expected to be much larger in the jet itself. Inside the jet electron temperatures are between 1 and 2 eV. Large amounts of reactive species are present in the jet with concentration of ozone and atomic oxygen of up to $10^{15}cm^{-3}$[10]

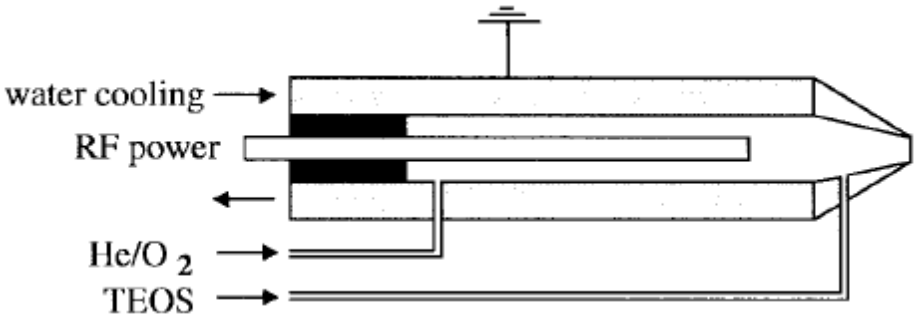

Figure 2.5: Typical Schematic of Atmospheric pressure plasma jet. Taken from Shutze [10]

To summarize these different types of plasmas Table 2.1 shows the charge species densities as well as reactive species densities for each type compared to the known quantities of the device in this work[10],[36- 40]. Reactive species densities are not currently know for this source but experiments to measure the densities are being designed currently.

Table 2.1: Comparison of Different Types of Plasmas

Source	Density (cm^{-3})			
	Electron	O	O^+,O_2^+,O^-	O_3
Low Pressure Discharge	10^8-10^{13}	10^{14}	10^{10}	$<10^{10}$
Arc/ Plasma Torch	10^{16}-10^{19}	10^{18}	10^{15}	$<10^{10}$
Corona	10^9-10^{13}	10^{12}	10^{10}	10^{18}
DBD	10^{12}-10^{15}	10^{12}	10^{10}	10^{18}
Plasma Jet	10^{11}-10^{12}	10^{16}	10^{12}	10^{16}
VHF Source	10^{10}-10^{13}	N/A	N/A	N/A

	Scale	Power Density ($W/cm^{3)}$	T_e	thermal
Low Pressure Discharge	mm -cm	0.1-10	1-10eV	N
Arc/ Plasma Torch	cm	~10^6	2-5 eV	Y
Corona	mm	~1	5 eV	N
DBD	mm	1-40	1-10eV	N
Plasma Jet	mm	20-100	1-2eV	N
VHF Source	cm	~25	1-2eV	N

2.2 Water Treatment

The use of plasma for the treatment of water has been in use for over a century. Initially this began with simple ozone generators. The ozone would then be used to purify water as it is as strong oxidizing agent that can disinfect water, resulting in this being one of the most prevalent uses for the chemistry in plasma [29,41]. These processes tend to used DBD discharges as ozone is seen in greater quantities with plasmas with low gas temperatures[42]. The production of ozone has also been produced in corona discharges that have seen significant levels of reduction of microbes and bacteria in short amounts of time [38,39]

2.2.1 Nitrogen Fixation

Nitrogen fixation in water is also another huge industry that this plasma device could serve well. Nitrogen fixation in water, through non natural methods, also began over a century ago, when a Norwegian team flowed air through a thermal arc. Nitric oxides were created and then converted into a nitrate salt [45]. The required energy to produce the nitric acid, 17kWh/kg, eventually led to the replacement of this process with the Haber and Ostwald processes [46]. In the mid-19^{th} century the role of nitrogen in crop production was first realized. Toward the end of the 19^{th} century it was discovered that microbial communities convert nonreactive N_2 from the air and convert it into useable reactive nitrogen forms (NO_x, HNO_3, N_2O, and NO_3^-) [56]. This led to a huge demand in reactive nitrogen that would be used as fertilizer. Up until this point only natural sources of reactive N could be found. This changed in 1913 with the invention of the Haber-Bosch process that allowed for the production of NH_3 from atmospheric N_2 via a chemical process. This caused an explosion in the amount of nitrogen available to the world, and as of 2002 this process produces the nitrogen fertilizer used grow half of the food eaten by the entire population of the world [57]. Recently, both nitrates and nitrites have been produced in aqueous solutions using many different types of non-thermal air discharges, such as gliding arcs, coronas and DBDs [47-49]. This is also seen with this atmospheric source as 120ppm nitrate solutions in water were able to consistently be produced.

The Haber-Bosch process consists of using high pressure (15-25MPa) and high temperatures (300-550°C) to convert N_2 to NH_3. Natural gas is used to supply hydrogen to the system. Due to the sheer amount of NH_3 produced worldwide, it is estimated than in the 1990's about 5% of natural gas produce was used in ammonia production. However, this is expected to decrease significantly as natural gas is used more extensively for world energy use as well as increases in supply throughout the world [58]. The process is also energy intensive as it is estimated that fertilizer production accounts for 1.1% of global energy production [59]. While the Haber-Bosch process has overall benefits, there are a number of dangers involved in the process. For one operating temperatures and pressures used in the process are very susceptible to explosion, enhanced through the extensive use of natural gas. Also, the anhydrous ammonia produced is used in explosives and production in large quantities requires strict regulation.

Another drawback to this process is the need for large scale operations as well as a significant transportation infrastructure to ship the fertilizer. This is where the potential of the source in this work could be used. If the fixation of nitrogen into the water is able to be improved to a near competitive rate, then the source could provide relatively cheap on demand fertilizer. Without the production of ammonia, many of the safety concerns traditionally associated with the production of fertilizer would also be remove, although the problem of NO_x species in the air would now be introduce.

2.2.2 1,4-Dioxane

1-4 dioxane removal is a water contaminant that is in need of an efficient process for removal. It is a hazardous micro pollutant and has been classified as a possible human carcinogen. Current tolerable limits are to be as low as 50μg/L according to tentative guidelines by the World Health Organization. [50]. Dioxane is commonly used as a stabilizer for chlorinates solvents. It is a strong solvent that is used for cellulose ester, cellulose ether, oils, fats waxes, rubbers, cosmetics, and many other products [51]. It has been detected from ground waters of landfills containing the products just mentioned [52] as well as in some natural waters [53]. Removal of the chemical can be difficult due to its

stability both biologically and chemically. Many current techniques for water treatments fail at the removal of 1,4-dioxane including chlorination and ozonation at ambient conditions [54], conventional activated sludge process [53] and air striping [55]. There has been some success in the development of combining ozonation with electrolysis to improve the degradation of 1,4-dioxane [50].

2.2.3 Perfluorooctanesulfonic Acid (PFOS)

Perfluorinated compounds (PFC) are a group of chemical substances that consist of organic compounds where the hydrogen atoms have been replaced by fluorine atoms that are particular difficult to remove from a system [60]. Production of the chemicals began in the 1950s and substantial amounts of these compounds have been produced in recent years [61]. Perfluorooctanesulfonic Acid is one of these compounds and has been banned in many countries as a persistent organic pollutant [61]. The compounds are used commercially in many products such as coating of paper or textiles, oxidative protective coatings on metals, inert surfactant for etching of semi-conductors, aqueous film forming foams, and thermally stable lubricants [60,61]. Treatments used in conventional wastewater treatment systems such as trickling filtration, activated sludge, anaerobic digestion and chlorination have had very little effect on the concentration of PFOS and PFOA [62, 60]. PFOS and PFOA are chemically inert because of the replacement of the C-H bonds with C-F bonds. This results in a chemical that cannot be broken down easily through traditional chemical means. Additional, there has been no evidence of any biodegradation [63,64]. In order to degrade these chemicals, an additional energy source must be used to assist in the breaking of the C-F bonds. This has been attempted through the use of UV and ultrasonic irradiation [64]

The lack of an established process for effective and efficient methods for the removal of PFOS and other PFC's presents an opportunity to find a unique solution that could be advanced. As the chemicals are still in great demand these chemicals will be a persistent problem. The development of novel chemistries mixed with the high energy, both kinetic and irradiated, in the plasma presents a potential pathway for the development of an efficient degradation process for many of these difficult to remove chemicals.

2.3 Paint Removal from Surface

This application was funded through a Strategic Environmental Research & Development Program (SERDP) project WP-1762. It focused on the implementation of plasmas for the removal of paint from US Navy vessel. Thus the paint samples used for this work were be derived from equivalent those found on US Navy vessels. Paint is used primarily as a protective coating for these vessels so this coating is required to have good adhesion to the underlying surface. There are several mechanisms to enhance and or degrade the adhesion properties of the paint. Increasing the roughness of the surface can increase the effectiveness of adhesion as it increases the bonding area the paint is exposed too. On the other hand any contamination on the surface with particulates or water soluble material can result in a degradation of the adhesion [66]. The current method of removal is a grit blast treatment which consists of ejecting an abrasive material through a high pressure gas stream that abrades away the softer paint materials. Grit blasting has effects that are both detrimental and beneficial to the adhesion of the new coat of paint. Particulates from the grit are always left over that could prevent adequate adhesion, but the increase roughness of the surface due to the grit blast could help enhance the paint adhesion. There are also environmental concerns with this technique as large amounts of waste from the process are collected. From the stripping of one large ship can create over 3,000 tons of contaminated grit that needs to be disposed of [67,68]. Furthermore, there is a danger to the operator as blasting with silica sand has been associated with health problems such as silicosis, an occupational lung disease[69].

Another method for removal is the through high pressure water streams [67]. The premise is the same as for grit blast but just water is used instead of an abrasive material in air. This technique has some advantages over grit blast such as a reduction of the waste to 50 tons as well as a reduction of protective equipment and a cleaner surface after treatment [68]. However, there are some disadvantages including the change of workers getting wet, which can be a problem in cold weather. The high pressure lines can break and the removal rates are lower for the water jet technique [67,69]. One other major challenge with the water jet techniques is the potential for flash rusting the steel surface of the ship. This rusting occurs

over a small amount of time and usually requires water soluble salt along with some form of water: liquid, vapor or humidity [70,71].

Two types of paint are used on ships and in the examination of this application. One is the freeboard paint system that gives naval ships their grey color that consists of two coats. One is a prime and tie-coat of anticorrosive epoxy polyamide. It consists of polyamide, polyamide adduct, magnesium silicate, titanium dioxide, butyl alcohol epoxy resin and naphtha. This is the topped with a coat of silicon alkyd [72,73]. The other paint is an antifouling coating consisting of a copper base. Antifouling coatings are used for the portions of the ship that are under water. These coatings are designed to prevent biofouling, which is the collection of biological material from collecting on the hull of the ship. This accumulation can result in increased fuel cost due to the additional weight and from the increased drag from the now rough surface traveling through water [74].

This has motivated the push to develop new techniques for the removal of paint as this is a common procedure during routine maintenance in the US Navy. Not only for the problems above but also the cost of the time associated to remove the paint as it is estimated to cost approximately $6.800-$24,000 a day to store a ship in dry dock [73]. Plasma is being investigated as an alternative due to the unique chemistries that can be achieved. These chemistries could then be used to remove the paint efficiently and also with minimal waste, as the paint removed should be the only particulate waste formed in the process. Potentially, some harmful gases could be generated in the plasma, so there would need to be removed in development or somehow monitored and contained during the operation.

Chapter 3: Source Design

The previous chapter went into the background of both plasmas and the applications that were experimented with using the source in this work. This included comparisons of existing plasma technology including other atmospheric sources. Also, the motivations surrounding the applications were discussed. This chapter examines the plasma source and its design in detail. It also provides an explanation into the mechanisms that allow for the stable production of an atmospheric glow plasma with the drive frequency of the generator.

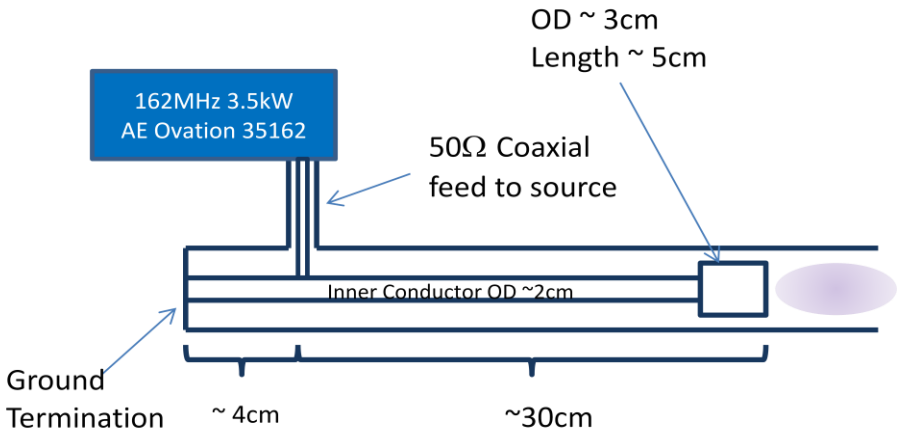

Figure 3.1 : Diagram of Atmospheric Source

The atmospheric plasma source is a simple coaxial device. The plasma forms at the end of the device allowing it to be applied to a variety of different materials. Through simple transmission line theory and tuned stub matching, a well matched plasma can be achieved with a very simple design. Figure 3.1 shows the generic design of the device. The coaxial structure can be broken up into two transmission line elements. The first extends from the RF feed to a ground termination; this is refered to as the shunt leg as it mimics the shunt element of an L-type network. The second extends from the RF feed to the electrode; this is refered to as the series leg as it mimics the series element of an L-type match. The plasma

then loads this network and the combined impedance, ideally, provides a matched impedance for the RF generator. The two transmission line segments can be adjusted easily to match the plasma load for a given set of parameters. A sliding metal plate is used at the ground termination that allows for changes in its length, while the entire inner tube can slide in or out of the device to change the length of the transmission line terminated to the plasma. The plasma forms with a radius of approximately 3.5 cm. This is quite large for an atmospheric plasma such as this which are typically held to very small dimensions such as microdischarges or tend to be thin needle type plasmas.

3.1 Coaxial Device Circuit

In order to insure optimal power delivery to the plasma, the source how to be designed such that when the plasma is in operation, there is very little or no reflected power in the system. This is done via tuned stub matching. Here the device itself acts as the matching network for the plasma system. It consists of two coaxial pipes that act as transmission lines. At the input of the device is an RF connector that then splits into two coaxial transmission lines. One line is terminated to ground, while the other is terminated to the plasma. Both lines can have their total length changed with little effort, allowing for the device to be able to form a good match for many different plasma conditions and feed gases. The lines have an inner diameter of The line terminated to the plasma flares out at the end to a large cylinder that has a diameter of 2.25 cm and an outer conductor diameter of 5.25 cm. The dielectric insulator between the inner and outer conducting elements is air, which gives the coaxial structure a charcteristic impedance of 51.7 Ω. This is calculated using equation (3.1) for the characteristic impedance of a lossy coaxial transmission line

$$Z_0 = \sqrt{\frac{R + i\omega L}{G + i\omega C}} \tag{3.1}$$

where R is the series per unit length, ω is the frequency of the signal, L is the self-inductance per unit length, G is the shunt conductance per unit length and C is the capacitance per unit

length. These values are calculated using the properties of the device and the following equations

$$C = \frac{2\pi\varepsilon'}{\ln\left(b/a\right)} \qquad R = \frac{R_s}{2\pi}\left(\frac{1}{a}+\frac{1}{b}\right) \qquad G = \frac{2\pi\omega\varepsilon''}{\ln\left(b/a\right)} \qquad L = \frac{\mu}{2\pi}\ln\left(\frac{b}{a}\right) \qquad (3.2)$$

where b is the outer conductor radius, a is the inner conductor radius, $\varepsilon = \varepsilon' + i\varepsilon''$ is the complex permitivity of air, μ is the permeability of air, and R_s is the surface resistivity of the aluminum structure

The generator and connecting cable have a standard impedance of 50 ohms. To be able to ensure that the impedance of the device at the exit is 50 Ω as well, the plasma impedance must be known, and this impedance can then be transformed using lossy transmission line theory which gives equation (3.3)

$$Z = Z_0 \frac{Z_L + Z_0 \tanh\left(\gamma l\right)}{Z_0 + Z_L \tanh\left(\gamma l\right)} \qquad (3.3)$$

where Z is the impedance at the end of a line where it is being measure, Z_L is the load impedance that the line is terminated to, l is the length of the line, and γ is the propagation constant given by

$$\gamma = \sqrt{\left(R + i\omega L\right)\cdot\left(G + i\omega C\right)} \qquad (3.4)$$

With these equations and a measurement of impedance at any point along the transmission lines, the plasma impedance for that set of conditions can be calculated. For the calculation done later the impedance is measured at the output of the generator and the impedance of the plasma is then calculated from this value

3.2 Plasma Equivalent Circuit

The plasma is modelled using a simple global plasma model and equivalent circuit to represent the electrical characterestics of the plasma. Figure 3.2 shows the circuit model of the plasma which consists of the bulk plasma impedance in series with the capacitive reactance of the surrounding sheath. The plasma impdeance is composed of the vacuum capacitance of the plasma region in series with a resistive and inductive term that depend on electron density and electron-neutral collision frequency.

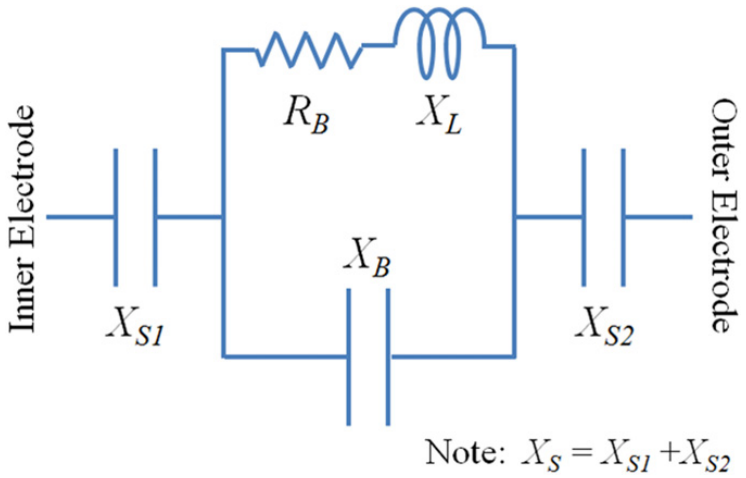

Figure 3.2: Circuit Representation of the Plasma

This equivalent circuit representation is commonly used to study the electrical response of rf discharges [75], and has recently been applied to discharges under atmospheric conditions [76]. Combining all of the terms in Figure 3.2 gives the total plasma impedance, Z_p, consisting of a real component, R_p, and an imaginary component, X_p. Ther real component of the plasma impedance is given by

$$R_p = \frac{R_B X_B^2}{R_B^2 + \left(X_B + X_L\right)^2} \tag{3.5}$$

where R_B is the dc resistance of the plasma, X_B is the vacuum reactance of the plasma region, and X_L is the plasma reactance. The dc resistance of the plasma R_B is given by

$$R_B = \frac{L\nu m_e}{Ae^2 n_e} \tag{3.6}$$

where L = 5 cm is the axial length of the plasma (estimated based on visual observation of the plasma), m_e is the electron mass, A = 9.6cm^2 is the area of the powered electrode surface, n_e is the electron density, e is the electron charge and ν is the electron neutral collision frequency. The collision frequency is estimated using the polarization cross section for charged species collisions with neutral species.

3.2.1 Collision Frequency

Polarization scattering is the main contributor for the collision processes in weakly ionized plasma. This includes the plasma produced by this device. As the plasma is operated in atmospheric conditions, the number of neutral particles is estimated using the ideal gas law with a gas temperature around 3000K which results in a neutral gas density of $2.5 \cdot 10^{18}$ cm^{-3}. This is five orders of magnitude large than the calculated electron density. The ion density can be assumed to be equal to the electron density as singly ionized molecules are the dominant form of ionization occurring in the plasma. However, the ions relatively slow velocities compared to the electrons results in a far less collisions between neutrals, thus the electron neutral collision frequency is used. This type of scattering is derived by modeling the atom as a positive point charge surrounded by a uniform negative charge sphere with equal and opposite charge. Using Gauss' law and induced electric field can be calculated. The resulting force combined with the incoming charged particle forces results in an induced dipole moment. This dipole then exerts a force which results in the following attractive potential[52].

$$U(r) = -\frac{q^2 a^3}{8\pi\varepsilon_0 r^4} \tag{3.7}$$

where q is the charge of an electron and $a^3=\alpha_p$ is the polarizability for the atom. Conservation of energy and angular momentum can be used to determine the cross section for this type of collision. This results in the Langevin or capture cross section

$$\sigma_L = \pi b_L^2 = \left(\frac{\pi \alpha_p q^2}{\varepsilon_0 m} \right)^{0.5} \frac{1}{v_0} \tag{3.8}$$

Then the collision frequency is

$$\nu_L = n_g \sigma_L v_R = n_g K_L \tag{3.9}$$

Where v_R is the relative velocity of the two particles and K_L is

$$K_L = \left(\frac{\pi \alpha_p q^2}{\varepsilon_0 m_R} \right)^{0.5} \tag{3.10}$$

where m_r is the reduced mass of the two particles. Therefore the collision frequency can be calculated using the following

$$\nu_L = n_g \left(\frac{\pi \alpha_p q^2}{\varepsilon_0 m_R} \right)^{0.5} \tag{3.11}$$

where n_g is the neutral gas density and $\alpha = 0.021$ nm^2 is the polarizability constant for air [81]. One important thing to notice is that this collision frequency is independent of the electron velocity. However, this does not cause a problem as it is shown later that through the emission spectra of the plasma that the electron temperature is rather constant over the range of conditions that the plasma has been operated under. Therefore it is assumed that any electron temperature dependence in the collision frequency is negligible. Using this equation, collision frequencies are calculated with the same order of magnitude (approximately 10^{11} – 10^{12} s^{-1}) used by other groups to model atmospheric discharges [76,77,84].

For the calculation of the collision frequency, it was assumed that the electron-ion interactions could be ignored. This is due to the densities of the neutral particles being at least five orders of magnitude larger than the densities of the electrons or the ions. To further justify this assumption the electron-ion collision frequencies were estimated and compared to the electron-neutral collision frequency. To do this coulomb collisions between and ion and

electron were considered. It can be shown that the collision frequency for an electron and ion interaction is given by [8]

$$\nu_{ei} = \frac{ne^4}{16\pi\varepsilon_0^2 m^2 v^3} \tag{3.12}$$

Where *n* is electron density, *e is electron charge, m* is electron mass, and *v* is electron speed. The electron speed was chosen as the average of a maxwellian distribution for a given electron temperature. While the electron energy distribution is most likely to not be maxwellian for this plasma, it is close enough for this calculation. The one problem with this equation is that it only accounts for large angle collision between the particles. This is relatively rare as small angle collisions tend to dominate and contribute more to the momentum transfer despite the small amount of energy transferred per collision. This is typically accounted for by the factor lnΛ, which is approximately 10 for most plasmas and can be calculated using

$$\Lambda = 12\pi n\lambda_D^3 \tag{3.13}$$

where λ_D is the Debye length of the plasma.

As the actual electron temperature is not known, a range of electron temperatures is considered for the electron-ion collision frequency. Reasonable electron temperatures used were between 0.1 and 2eV. Using an electron density of 10^{12} cm^{-3} as is calculated for this plasma and multiplying equation (3.12) and (3.13) gives a maximum value for the electron ion collision frequency of 0.132 GHz at 0.1eV and 2.542E-3 GHz for 2eV. These numbers are approximately three orders of magnitude smaller than the estimated electron neutral collision rate. Even if these calculations are off by a factor of 10 there is still a factor of 100 between the two rates. Thus this collision frequency can be effectively ignored as it contribution is less than the error in the estimation of the electron neutral collision frequency.

3.2.2 Reactive Components

The reactive portion of the plasma impedances is made up of the capacitive sheath terms in series with the reactive component of the bulk plasma impedance. The vacuum reactance of the plasma X_B is the difference between the reactance of the load termination

without plasma X_0 and the sheath reactance X_s. The sheath is modeled as two series vacuum capacitors defined by their effective surface area and sheath thickness ($OD\pi L$) and s, respectively, where OD is the outer diameter of the coaxial structure. The no-load termination X_0 is measured in the absence of a plasma via one-port measurement of the source impedance using a Hewlett Packard 8753 network analyzer at the end of the cable that is normally connected to the RF generator. The termination impedance measured at this point is then transformed to the open end of the coaxial assembly using equation (3.3) and solving for Z_L. The bulk plasma reactance is modeled as an inductor

$$X_L = \frac{\omega R_B}{\nu} \tag{3.14}$$

And the imaginary component of the total plasma impedance is given by

$$X_p = X_s + \frac{X_B R_B^2 + X_L X_B \left(X_L + X_B \right)}{R_B^2 + \left(X_L + X \right)^2} \tag{3.15}$$

And

$$X_s = \frac{-s}{\varepsilon_0 \omega A} \tag{3.16}$$

Where A is the cross sectional area of the plasma

The previous equations constitute all the necessary information for this simple model of the plasma. In these equations there are two plasma parameters that ultimately determine the plasma impedance $Z_p = R_p + iX_p$; electron density, n_e, and sheath thickness, s. Measurement of the plasma loaded impedance of the coaxial structure at the generator output can be transformed to the plasma impedance via the transmission line equations representing the structure of the device. This gives values for both R_p and X_p. Equations (3.5)-(3.16) provide a system of equations with two unknowns, n_e and s, that can be calculated. Similar high-frequency models have reported good correlation to plasma conditions for VHF atmospheric plasmas under different conditions (gas, geometry, power density etc) [23].

While this model works well for the plasma in the region where this device operates, there are some limitations to this circuit representation of the plasma. For example, at low electron densities the plasma resistance begins to asymptotically approach zero. While this

may be an accurate description this still represents a region where practically the information cannot be used as error inherent in measurements begin to account for huge differences in electron densities. This is also true of higher densities as the plasma behaves differently once it reaches a certain electron density. It is discussed extensively in section 3.3 that once the electron density hits a certain value a positive feedback loop occurs causing the plasma to transition to an arc. At this point the model breaks down due to the different characteristics of an arc plasma compared to a glow plasma

3.3 VHF Ballasting

Although this is a very common electrical representation of a plasma, there is an unusual response that is seen due to the high drive frequency used for the plasma. It is seen that as electron density increases, an increase in the real part of the plasma impedance also occurs as seen in Figure 3.3. This is counterintuitive to what would be expected. One would expect that with a higher electron density, and thus a larger number of charge carriers, that the real part of the plasma impedance would decrease as extra electrons would allow the current to flow easier. It must be noted that the total plasma impedance, including all of the inductive terms, is the term that increases. The bulk resistance of the plasma, R_B, still decreases, and this is the term that is directly related to the electron density and follows the idea that more electrons equals less resistance.. Since this value still decreases, the response of the total system is due to another part of the system. In this case it is the frequency and its subsequent influence on non-dissipative elements in the plasma that now have sufficient reactance to contribute to the real portion of the plasma impedance. Figure 3.3 shows the real part of the total plasma impedance, R_p, versus electron density for a variety of different drive frequencies. This data is derived from the model, and compared with experimental data

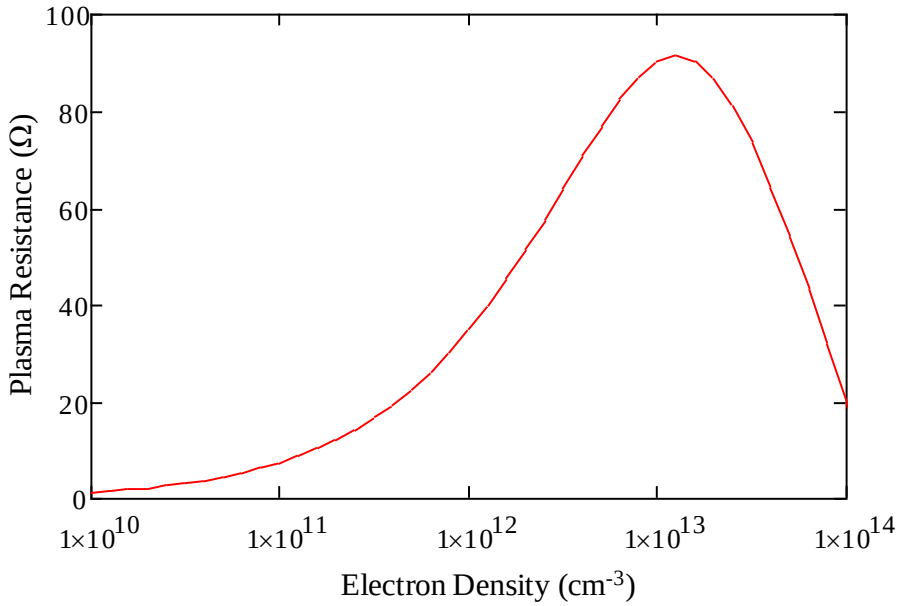

Figure 3.3: Plasma Resistance vs. Electron Density

for the frequency of the device. For all frequencies the plasma resistance seems to follow a similar trend where at first it increases with electron density, until a transition point is reached where the resistance begins to decrease with increasing electron density. However, as the frequency is reduced, this transition point happens at lower electron densities. This is an essential part of this plasma system allows the operation of the device as a glow instead of a thermal arc. The absence of thermally driven instabilities and arcs is believed to be due to the plasma impedance response to increasing electron density. Staack et al presented a very straightforward explanation for the propagation of ion overheating instabilities in atmospheric plasmas [19]. In this work, the progression from increasing electron density heating the background gas (and thereby reducing the gas particle density), which increases the E/n ratio for a dc discharge, increasing electron temperature and thereby increasing ionization rate and thus electron density (further feeding this chain from the beginning) was illustrated as a straightforward mechanism with positive feedback that drove this instability in atmospheric systems. This is illustrated in the left part of Figure 3.4.

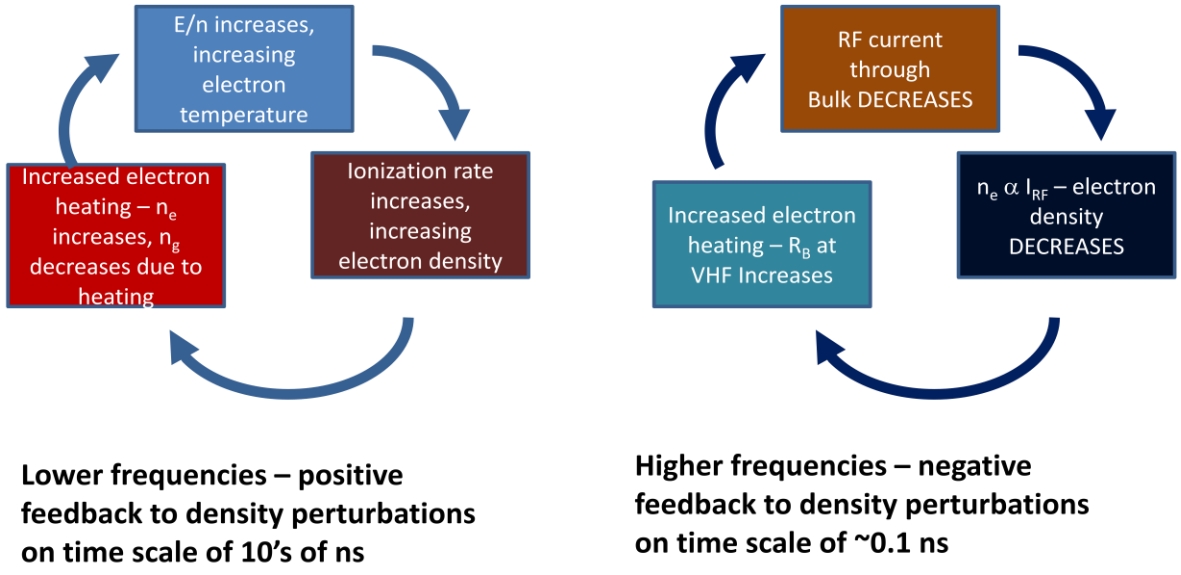

Figure 3.4: Comparison of Low Frequency vs. High Frequency Response to Density Perturbations

At very high frequencies such as 162 MHz, a similar analogy can be made, but in this case, negative feedback is observed. The analogy is as follows: assume that through some perturbation, an incremental increase in electron density δn_e is generated in the coaxial discharge. Similar to the ionization thermal instability, this results in a reduction in background gas density. Additionally, this results in an increase in the real portion of the plasma discharge impedance, R_p. This increase in R_p decreases the RF current driving the plasma discharge assuming that the delivered power is constant since $P = I^2 R_p$. P is the delivered power to the system and I is the RMS current amplitude through the discharge. On first order, the electron density tracks with RF current and sheath thickness with the equality $s_0 e \omega n_e A = I$, where s_0 is the sheath thickness of the capacitive discharge [82]. Reviewing the plasma parameters summarized in Figure 3.4, s_0 is a relatively slowly varying parameter compared with electron density as a function of P (and hence I_2), and is therefore not a significant contributor to the change in I. Therefore, the introduction of δn_e reduces I, and introduces negative feedback to the time dependence of δn_e, effectively restoring the electron density established by the global particle and energy balance of the discharge. Taking a nominal discharge impedance of $(24.9 - j198)\Omega$ that was measured at 560W, 5 L s^{-1} gives

an RC time constant of 0.1 ns, much shorter than the measured characteristic frequency of thermally driven instabilities such as ionization overheating, which are tens of nanoseconds. This negative feedback, coupled with the much faster time response of the system, is believed to be the mechanism that supports a volume glow in this source; effectively, the plasma load acts as a ballast at these high drive frequency conditions for atmospheric discharges. Varying frequency in equations (3.5)–(3.13) show that as frequency is decreased, the electrical response of the system reverts back to a regime where increasing electron density reduces bulk plasma resistance, thereby introducing a positive electrical feedback that cannot counteract instabilities induced by changes in δn_e. This frequency dependence is illustrated in Figure 3.5. Additionally, the reduction in gas density that follows the introduction of δn_e has minimal impact on the RF impedance of the discharge, even for reductions as high as 10×.

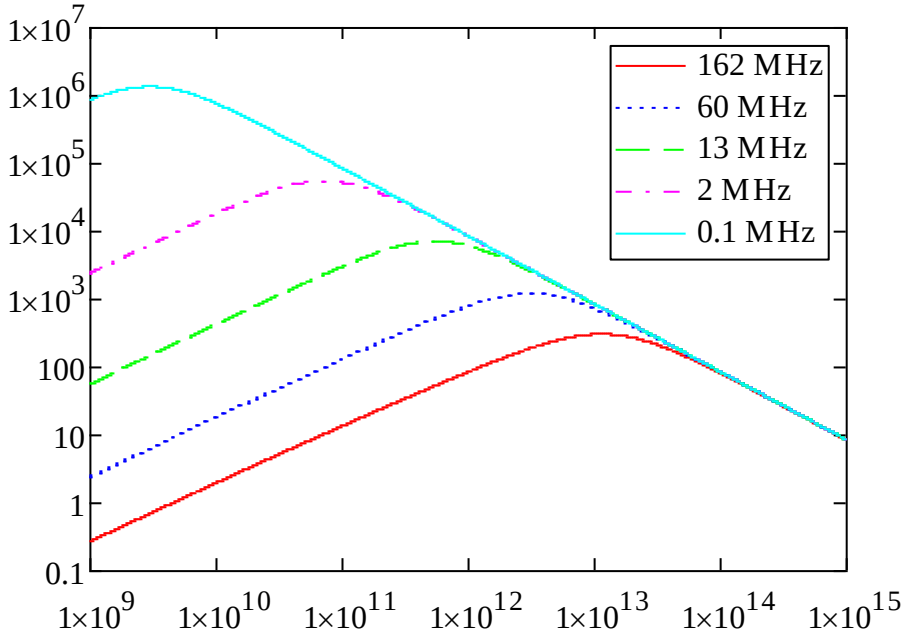

Figure 3.5: Frequency Dependence of the Ballasting Effect

Chapter 4: Plasma Characterization

In the previous chapter we introduced a coaxially driven atmospheric plasma source and a simple equivalent circuit model that predicts a regime where a volume glow discharge can exist without transition to an ion overheating instability induced arc formation.

To understand the plasma and its responses, a variety of diagnostics must be used that help to characterize the plasma. These diagnostics are crucial for learning the mechanisms that drive the behavior of the plasma. Optical emission spectroscopy, plasma impedance measurements, and b-loop probe experiments are all used to study both the device and the plasma itself. Through parametric studies of the plasma using these diagnostics the responses of the plasma can be studied extensively regarding changes, in air chemistry, input power, flow rates, transmission line lengths, and even shape of electrode. This information can then be used to improve upon the performance of the plasma as many of the parameters

4.1 Optical Emission Spectroscopy

Optical emission spectroscopy is an extensively used technique for the characterization of plasmas. It involves analyzing the emitted light from the various excited species that are in the plasma. Each individual atom or molecule emits a certain wavelength due to the excited states that exist in its structure. The light emitted from the plasma is directed into a spectrometer where it hits a grating that disperses the light into its individual wavelengths which is then incident on a CCD camera to display the spectra. In this work spectroscopy is used for two main objectives: Molecular and atomic identification and gas temperature measurements.

When dealing with spectroscopic measurements it is important to determine if the plasma is considered to be optically thin. An optically thin plasma is one that does not absorb a significant amount of radiation. This causes problems when performing certain spectroscopic measurements as a portion of the light emitted from the plasma will be absorbed if the plasma is not optically thin. In order to determine if it is optically thin the absorption coefficient for the radiation must be studied. For this plasma, OH emissions are

the most used spectral lines, so one of these lines will be used to demonstrate. The absorption coefficient is obtained through the cross section of the OH molecule for the line emission at 307.8nm, $5.423 \times 10^{-16} cm^2$[85], and the density of OH molecules in the plasma. The density of the OH molecules is only estimated as there have been no measurements to determine this. To estimate this number the relative humidity of the air stream was found to be around 4%. This leads to a molar concentration of water in the air stream of 0.11%. With a gas density around $2 \times 10^{18} cm^{-3}$ this results in a maximum water molecule density of $2 \times 10^{15} cm^{-3}$. To determine the amount of radiation that can escape the plasma the following equation is used

$$I = I_0 \exp\left(\sigma_{eff} n_{OH} l\right) \tag{4.1}$$

where I is the final intensity of the light I_0 is the initial intensity, σ_{eff} is the absorption cross section, n_{OH} is the density of OH molecules and l is the length that the emission must travel through. To account for the fact that not all radiation must travel through the entire discharge the plasma can be broken into an arbitrary number of sections j. Then the amount of light escaping from each section can be added together using the following equation

$$I = \sum_{i=1}^{j} I_{0j} \exp\left(\sigma_{eff} n_{OH} l_i\right) \tag{4.2}$$

where I_{0j} is the amount of the total intensity each segment produces and l_i is the length that the light from each segment must travel. When an OH density of $10^{15} cm^{-3}$ is assumed only about 71% of the emission would escape the discharge. However, this is the upper estimate for the amount of OH in the system and this is likely much larger than the actual density. When the density is reduced to 10^{14} cm^{-3} then the amount transmitted becomes 96.5%. This indicates that this should not pose a huge problem with the spectroscopic data. Also, for most of the data presented here this absorption does not play a significant role as the absolute intensities of the spectroscopic data were not used for any calculations. A ratio of two lines is used in the gas temperature measurements but that is addressed in section 4.2.

4.1.1 Experimental Setup

The OES measurements were all done using two different spectrometers. The Verity SD1025 LC-5 was used in order to take full spectra over the entire visible light region. This allows for general identification of atomic lines. The Acton 2500sp is a Czerny-Turner monochromator and is used for high resolution spectra that can be used for confirming identification lines as well as the temperature measurements of the plasma. Czerny-Turner monochromators are a common design where the goes through an entrance slit approximately 10μm thick. The light is then directed toward a curved mirror that collimates the light. This light then hits a grating and is diffracted, which hits another mirror that focuses the light onto the exit. At the exit there is a PIMAX 256 CCD camera that collects the light. Due to the grating and the size of the monochromator the CCD camera is able to read a range of about 40 nm with resolutions of .05nm. For the actual experiments, light emitted from the plasma source is directed toward the entrance slit using a fiber optic cable. At the exit of the fiber optic are two mirrors that focus the light into the slit ensuring the maximum amount of light enters the monochromator. Figure 4.1 shows the basic setup of the experiment.

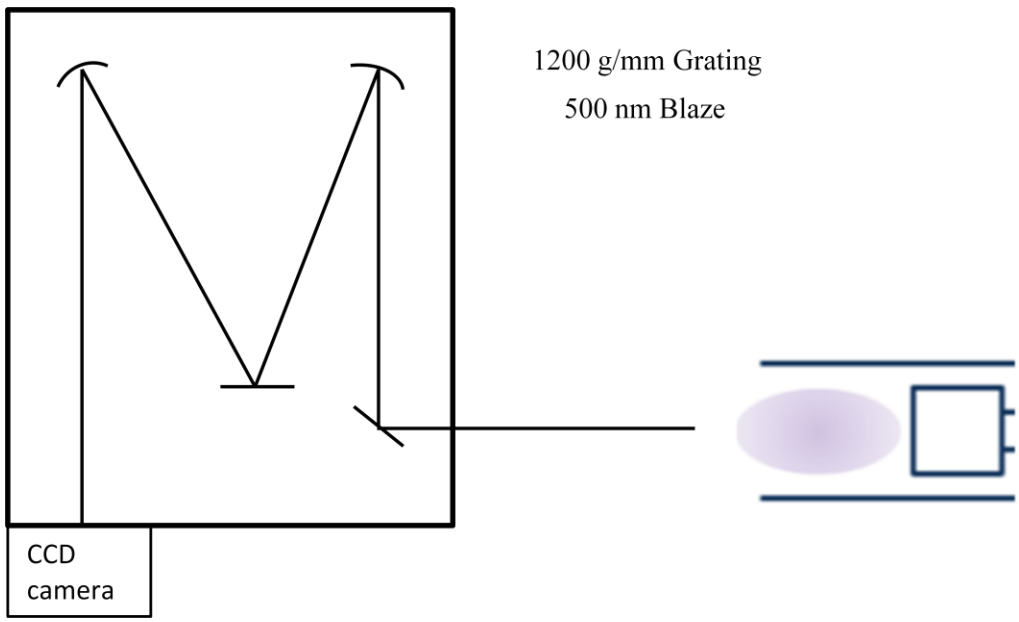

Figure 4.1: Diagram of OES Experiment

4.1.2 Gas Identification

A number of gases have been successfully run in this device including: He, Air, Argon, Nitrogen, and CO_2. This allows for many possibilities to be able to run many other more exotic gases that could allow for future applications. Each of these gases produce unique chemistries that need to be characterized. Also, as each of these experiments was run in open air, there was always some amount of air that was present in the discharges. The Verity was used in order to take these measurements as the entire spectrum needs to be analyzed. The following spectra were taken looking into the end of the device and simply represent an average over the entire plasma. Later on for the gas temperature measurements the spectra were resolved spatially and analyzed as a function of distance from the electrode. Air is the most common gas flowed through the device as it is readily available in and has been used in most examinations of applications. Figure 4.2 shows normalized spectra for a range of powers in an air discharge with most of the peaks labeled as to what atom or molecule it represents. The spectra were normalized so that the area under the curve was equal to one.

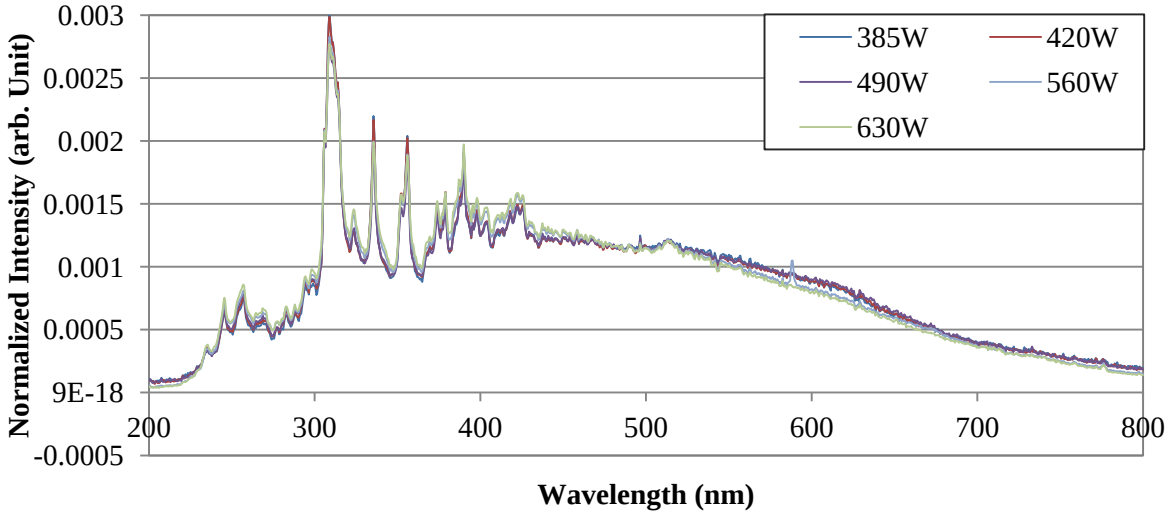

Figure 4.2: Normalized Spectra for Air Plasma for Different Powers

The normalization indicates that there is very little change in the species present in the discharge even with significant changes in power. The nitrogen, oxygen, and NO_x peaks are all seen here as would be expected from a gas consisting of nitrogen and oxygen. However, there is a very large OH peak around 309nm that can be seen. This arises because the air supply contains water as well as the humidity in the surrounding room. When the spectra are not normalized, the total magnitude of the spectra increases with increasing delivered power. This is expected as visually there is an increase in the brightness of the discharge that corresponds to the spectra in Figure 4.3.

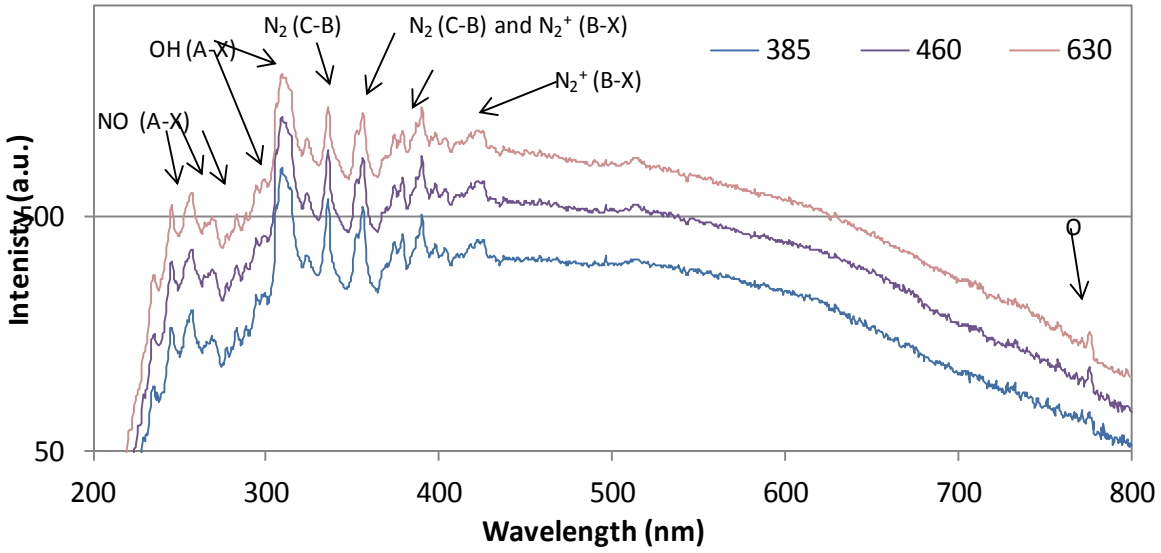

Figure 4.3: Air Emission Spectra

The effects of the flow rate of the air through the device is examined next. Figure 4.4 shows the raw spectroscopic data for an air plasma at 500W for three different flow rates. At low flow rates the plasma is much brighter, which is indicated by the significantly larger intensity of the 5 scfm emission versus the 6 and 7 scfm emissions. Figure 4.5 shows the normalized spectra for the same parameters. Large differences between the peaks around

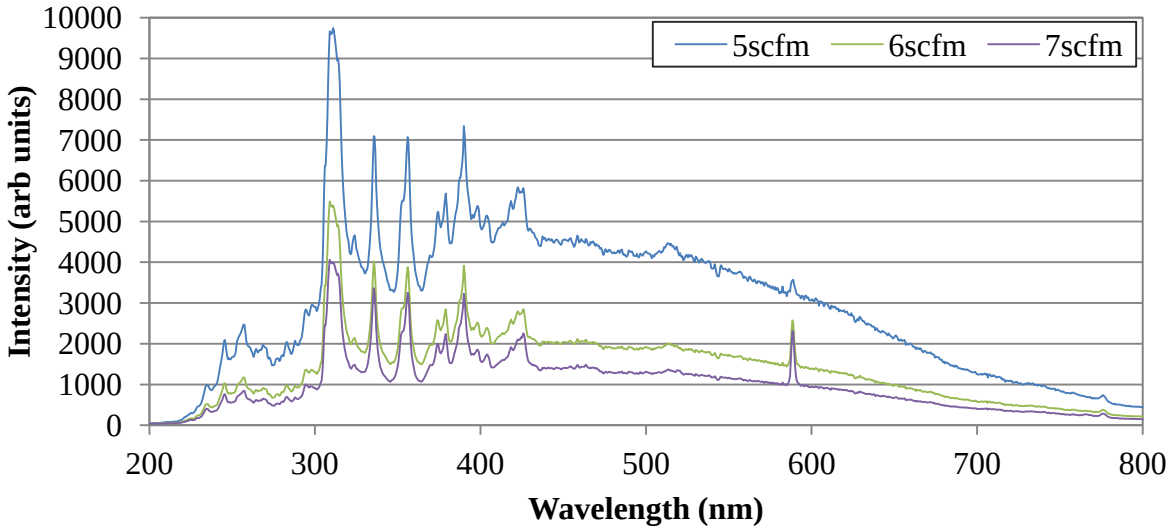

Figure 4.4: Spectroscopy Data for Multiple Flow Rates

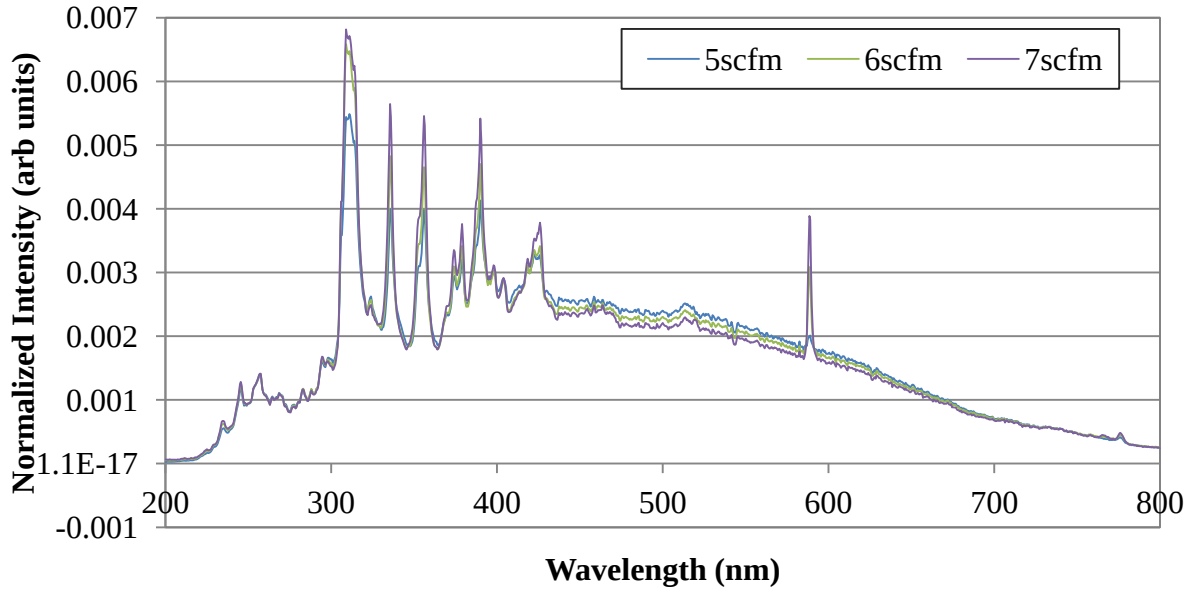

Figure 4.5: Normalize Spectra for Flow Rate Sweep

305 and 590 nm, for the OH and Na emissions respectively, represent a difference in the composition of the plasma. At 5 scfm both the OH and the Na peaks are significantly lower indicating less of both of these substances in the plasma. The lower flow rate would introduce less of the humidity that exists in the air supply line. The water in this air provides the hydrogen to generate the OH peaks as well as the sodium contaminants that exist in water.

Successful operation of multiple gases is critical to the further development of the source. As the design of the electrical circuit allows for variability in the plasma impedance while still maintaining a reasonable match, it is not difficult to run many gases with minimum reflected power. The following figures show the full spectrum obtained for each of the gases that have been successfully operated with in the device. This also allows for picking gases for different applications where certain molecular species are necessary to produce a desired effect. For example, OH radicals are necessary for the removal of certain chemicals in water, but the nitrogen in air can create nitrite and nitrate molecules in the water. Therefore the elimination of nitrogen would be necessary to improve upon the treatment method. Figure 4.6 is the emission spectrum for the plasma with carbon dioxide used as the feed gas. As the plasma is being operated in room air with CO_2 flowing through it there is still nitrogen in the discharge and is seen in the emission lines of CN. The atomic oxygen line at 777 nm is clearer than before.

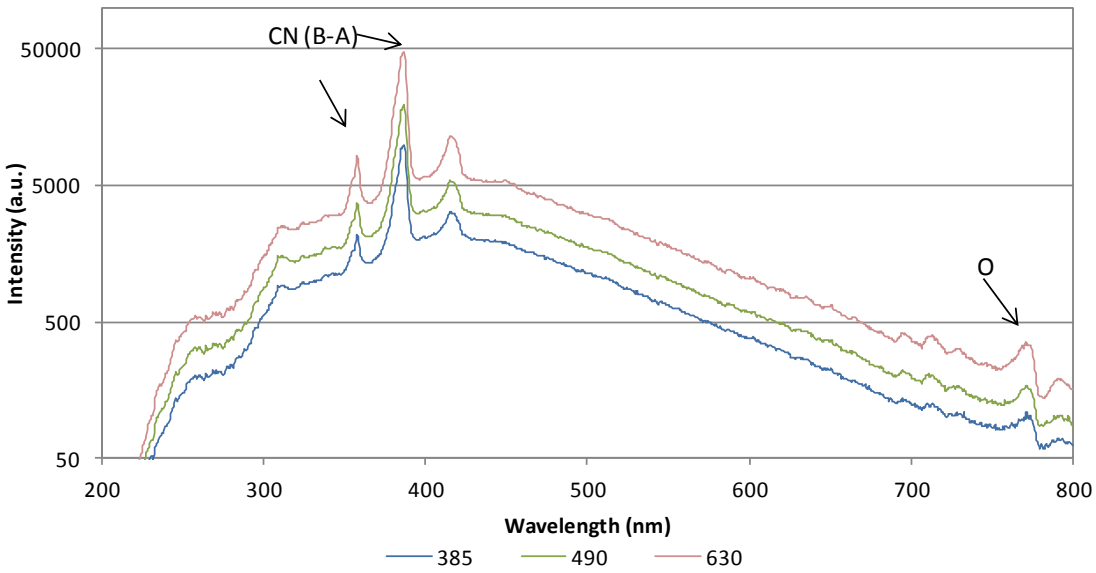

Figure 4.6: Carbon Dioxide Emission Spectra

Figure 4.7 shows the spectra for the same 3 input powers when the feed gas is nitrogen. Here the spectra are completely dominated by nitrogen species of different excited states. This was expected as air consists primarily of nitrogen, ~78%, the amount of oxygen present in the discharge is completely dominated by the nitrogen species. Also, the OH radicals have also gone away as the nitrogen source comes from a high purity gas tank that contains no water and thus no hydrogen atoms to form the OH radicals.

Figure 4.8 is the spectra for the same three inputs powers but with Helium as the feed gas. The helium discharge required a lower flow to sustain the same glow type of plasma as the other gases, resulting in the spectra resembling the air plasma spectra but with the addition of helium atomic emission lines also being present. Even though the compressed air flow is not running the OH radical peaks are still present due to the humidity of the air inside the lab. However, the OH peaks do not dominate as in the helium discharge like it does in the air discharge, and some of the nitrogen species begin to dominate along with the emissions of He.

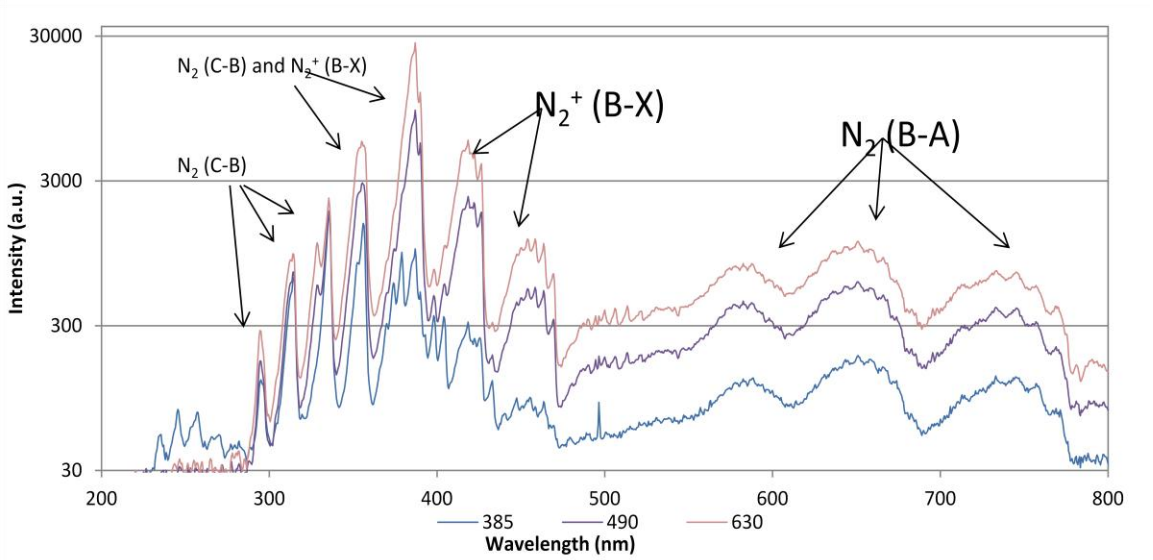

Figure 4.7: Nitrogen Emission Spectrum

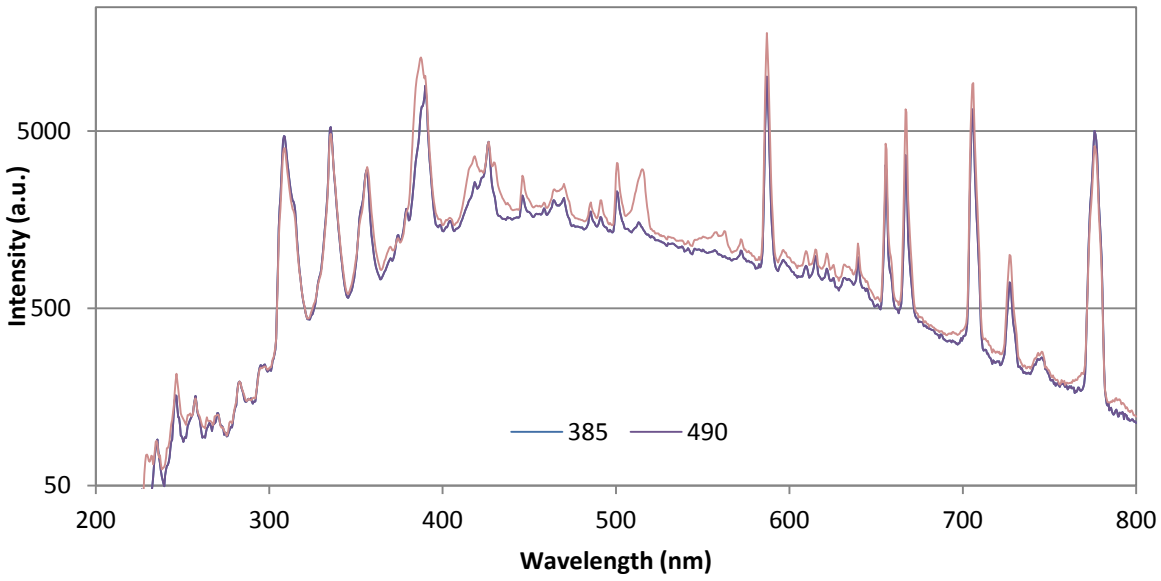

Figure 4.8: Helium Spectra

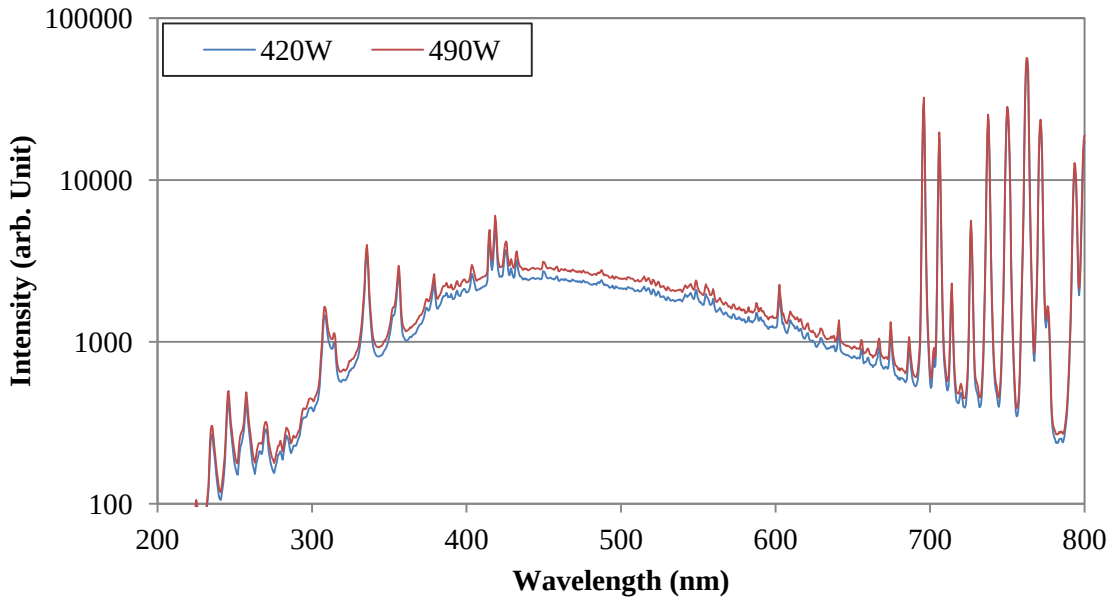

Figure 4.9: Argon Spectra

Figure 4.9 shows the spectra for two power levels of argon. The y axis is on a logarithmic scale so that the small peaks with shorter wavelengths can be seen. The emission is dominated by the argon lines in the 700-800nm range, although some of the same OH and NO peaks can be seen but with much smaller intensities. This indicates the atmospheric air is still playing some part in the active plasma. Argon was not used for most of the following experiments as it had a much different behavior than the rest of the gases. Instead of forming a plasma that is about 10cm long filling the diameter of the device, the argon plasma would form a long thin filament that grew up to over 40cm in length. It would come out of the original device and an extra length of tubing had to be added to prevent the plasma from interacting with anything outside of the device. While the argon plasma was mostly contained in the slender filament in the center of the device there was a much less dense region surrounding this center portion. Interestingly there was also a small dark space between these two regions of the plasma. This region can be seen in Figure 4.10 a. just outside of the brightest center portion of the plasma. Another unexpected occurrence with argon is the formation of a pattern on the surface of the electrode. A close up of this pattern

can be seen in Figure 4.10 b. This pattern seemed to stay constant when looking at it although there was some overall rotation that could be seen. This is probably due to the gas flow in the device as the plasma itself is also rotating. It is not clear what causes this phenomenon and because of this and the shape of the argon plasma. It was decided that argon would be excluded from many of the following experiments because of its significantly different behavior, and the fact that argon plasmas would have less reactive species that could be used for potential applications.

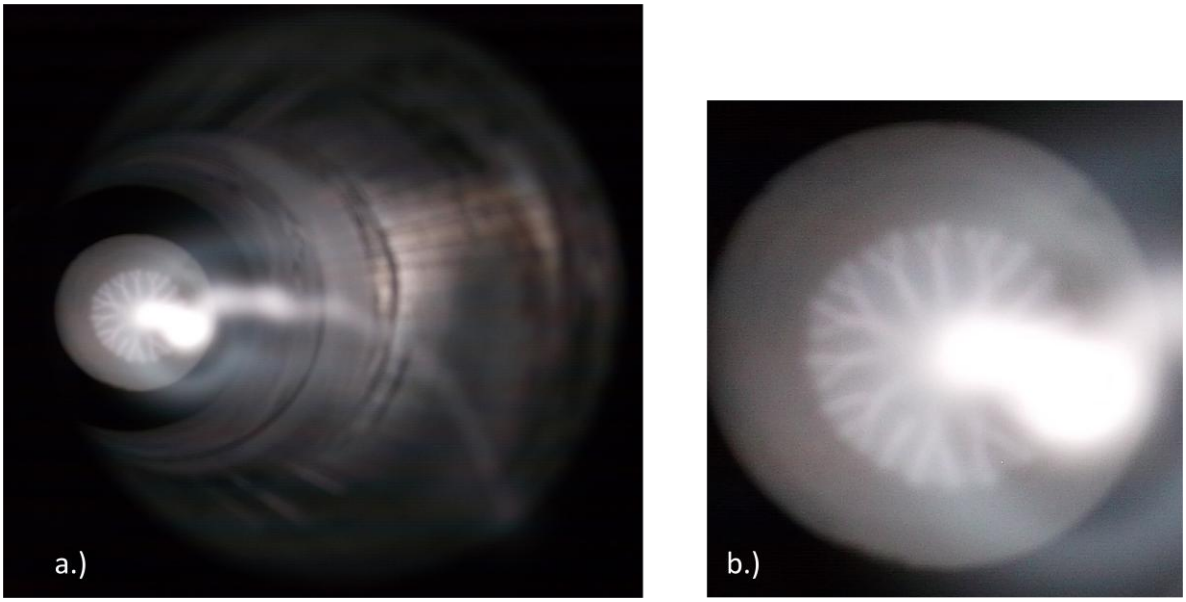

Figure 4.10: Argon Plasma; a.) Full Plasma Photo b.) Close up of the Patter formed on the Electrode

4.2 Gas Temperature Measurements

OES must be used in order to obtain a measurement of some of the temperatures of the different molecules (vibrational, rotational, and electronic). As the plasma is no in equilibrium it is difficult to know the true gas temperature as there are many molecules that are at different temperatures. Focus is placed on the OH A-X rotational temperature. This transition is very strong for air plasmas with even a small amount of H20 (~1%). This can be

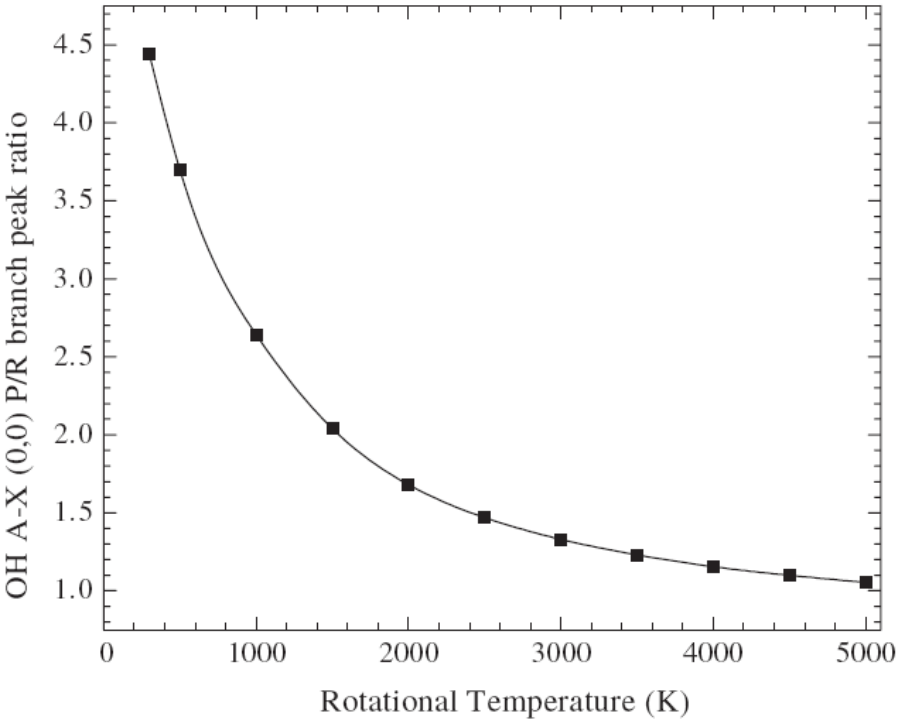

Figure 4.11: Ratio of P and R branches vs. Rotational Temperature (Laux)

seen in the above spectra as the OH peaks around 309 nm tend to dominate the spectra. When water is directly introduced to the system the OH is essentially the only observable peak. Rotational temperatures can be assumed to be close to the gas temperature due to the extremely fast rotational relaxation at atmospheric pressure because of the large number of collisions experience by the particles. The technique to determine the OH is derived from [78]. The OH A-X transition has a number of peaks in the region of 306-312nm. These spectra can be fitted to a spectroscopic model used in SPECAIR, which simulates an emission spectra based on the species within a discharge. However, the temperature can be derived from the relative intensities of two of the groups within the band, specifically the R and P branches of the OH A-X (0,0) vibrational band. These bands have peaks at 307nm and 309 nm. Using SPECAIR, Laux et al. [78] were able to produce a plot that gives the rotational temperatures as a function of the ratio of the P and R peak intensities (P/R), in

Figure 4.11. From this plot if the ratio of the two peaks is known then the rotational temperature of the OH can be simply found from the curve.

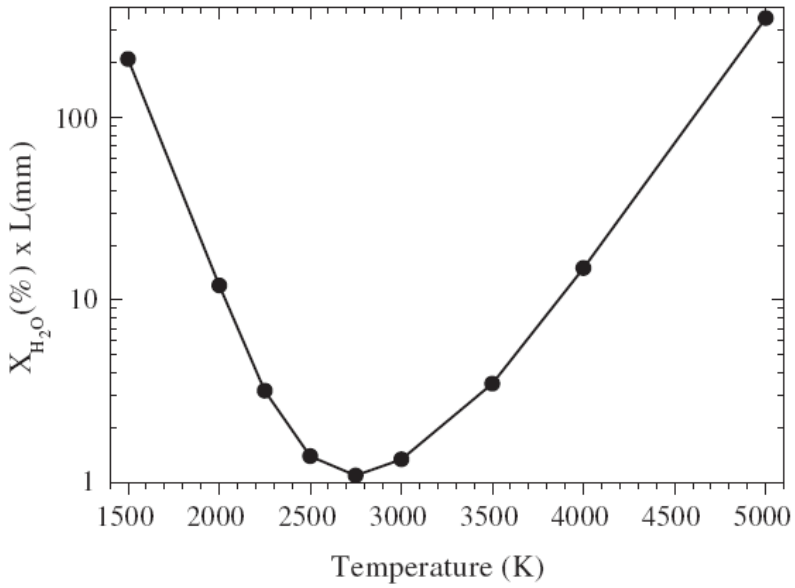

Figure 4.12: Optical thickness times water vapor mole fraction that would result in 4% self-absorption of P-branch peak (Laux)

This technique is useful because does not require an absolute or relative intensity calibration due to the close proximity of the peaks. At such close wavelengths, detector response can be considered effectively constant. There is potential for self-absorption of the emitted light that can cause an error in the final temperature measurement. The P-branch is more readily self-absorbed than the R-branch which could lead to a decrease in the P/R ratio which results in a higher temperature measurement. The optical thickness of the plasma is what dictates if this is a problem. Figure 4.12, taken from [78], shows the level of water vapor in a plasma that would cause a 4% self absorption. Based on this plasma with a temperature around 3500K it would require the air to have a mole fraction of water vapor of .1%. At this level, the effects of self absorption could be ignored. The air lines were measured to have a relative humidity of 4%. This results in a mole fraction of water to be

about 0.11%. Using the length of the plasma, this results in a point on Figure 4.12 just above the 4% self absorption curve. At this temperature the difference the self absorption has a negligible effect on the final estimation of the rotational temperatures. At higher temperatures a small change in the ratio will have a more significant effect as the slope in Figure 4.11 is approaching zero resulting in large changes in measured temperature with small changes in the ratio. This is even less of a factor for the spatially resolved measurements that are made. These spatial measurements have a much smaller optical thickness as only the plasma radius contributes to the thickness, and therefore has less of an effect on the temperature measurements. These spatial temperature measurements tend to correlate well with the average temperature measurements taken from the end of the device.

4.2.1 Experiment

In order to resolve the peaks needed for the gas temperature measurements, the Acton 2500 monochromator is used along with the PIMAX 260 camera. This allows for sub nanometer resolution. As the camera allows for up to a 40nm spectrum to be obtained at once, these measurements are done so that both peaks are captured at the same instance. This prevents any variations in the plasma with time to be removed which would alter the measurements. Gas measurements were done for ranges of two different parameters: gas flow rate and power.

Figure 4.13 shows the raw spectroscopic data from the gas temperature measurements. It shows mainly the two peaks needed to produced the ratio. The P-branch intensity is larger than the R-branch intensity which gives a ratio larger than 1. According to Figure 4.11, this must be true to be able to obtain any information from the plot. Another more informative way to view this data is to normalize the intensities so that the P-branch

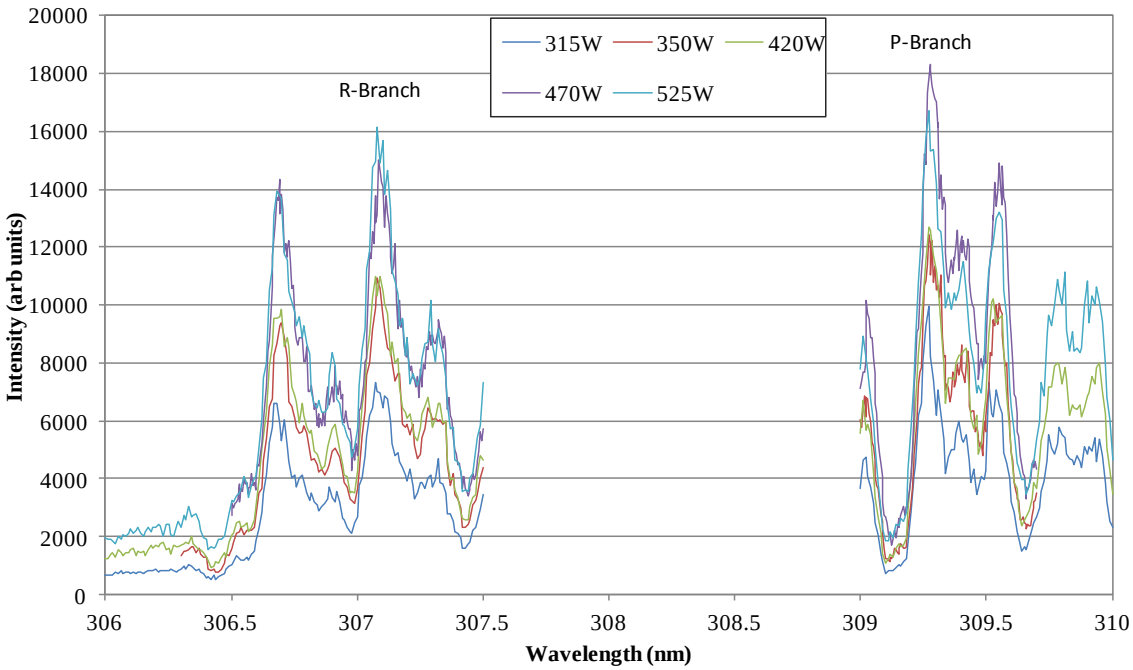

Figure 4.13: Power Sweep of the Gas Temperature Spectroscopy Measurements for 3.5 scfm

peak is equal to one. As it is the highest point all other data points are less than one. This allows for visual trends to be seen in this raw data. As gas temperature decreases when the ration increases, it can be seen qualitatively how the gas temperature changes with changing powers. Figure 4.14 shows this normalized plotting of the data. It can be seen that the blue line which corresponds to 315 W has the lowest R-branch peak. Therefore it has the lowest P/R ratio and thus the lowest temperature. This is useful when taking experimental data to observe and confirm trends while measurements are being made.

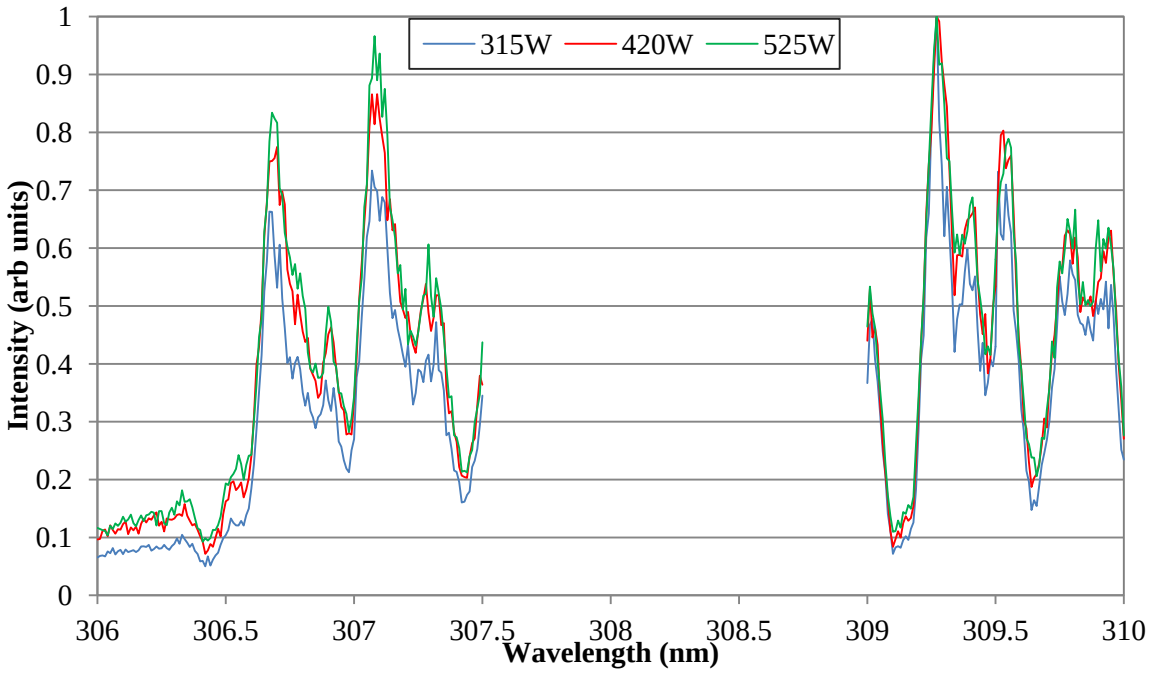

Figure 4.14: Raw Spectroscopic Data Normalized to the P-branch

Now that the P/R ratio can be calculated, the rotational temperature measurements can be found from Figure 4.14.. Figure 4.15 shows the calculated rotational temperature as a function of input power. There is a clear trend for the gas temperature to increase with increasing power as more energy is being delivered into the plasma. This data was then connected to the electron density calculation that had been made before this data was taken. Figure 4.16 shows this plot of the temperature vs. electron density. Once again there is an increase in the gas temperature as the electron density increases. Temperatures are measured to be between 2700 and 5000 K. This puts the gas temperature to be close to these numbers and would appear to show that the plasma is not in thermal equilibrium as it is assumed that the electron temperatures would be on the order of 1eV. However, this shows that the plasma is not a cold plasma and could still pose some problems for applications that are temperature sensitive.

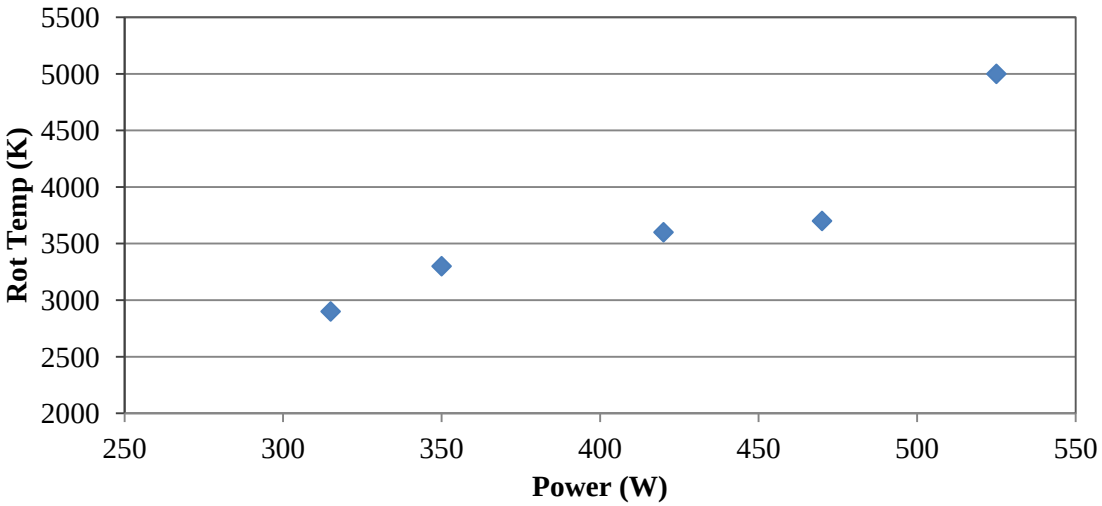

Figure 4.15: Rotation Temperature vs. Input Power for 3.5 scfm

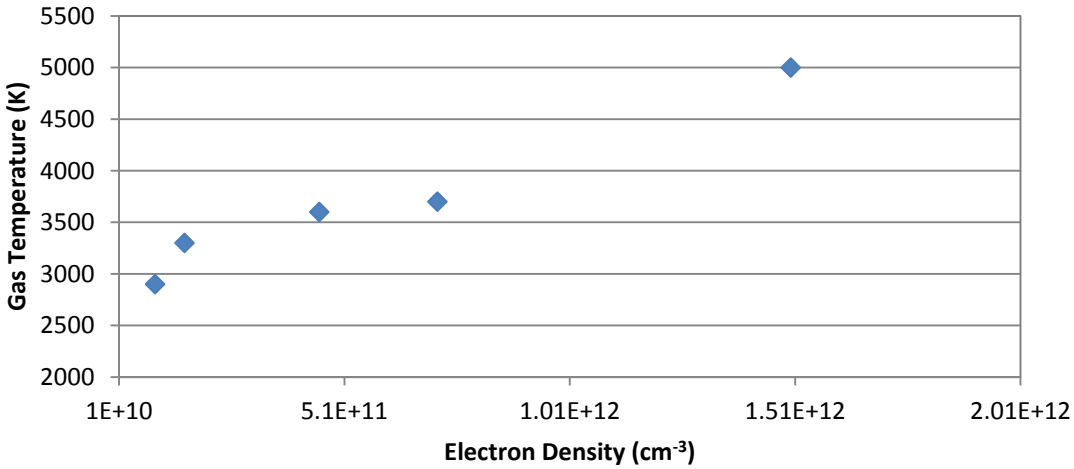

Figure 4.16: Rotational Temperature vs. Calculated Electron Density

The other parameter to look at is the flow rates. A second set of data was taken at the same input powers, but with a gas flow rate of 5 scfm. The only difference is that 315W is not included in the measurements as the plasma is not able to sustain itself with as high an air flow. Figure 4.17 compares the two power sweeps for each flow rate. The major difference is that the higher flow rate tends to measure a lower gas temperature. When the flow rate is

high, the plasma becomes much less bright. This would indicate a drop in the electron density. If the electron density is low then there could be less interactions with these higher energy particles that would be able to exchange that energy with the OH radicals. Also, the one point for the low flow at 525W where the temperature jumps to 5000K seems out of place. Before that point, it appeared that the temperatures were slowly converging to a common temperature for higher powers. This could arise from some error in the measurement that arises from the variability in the plasma. It could also be correct as there are not nearly enough data points on this plot to know if these numbers are actually converging.

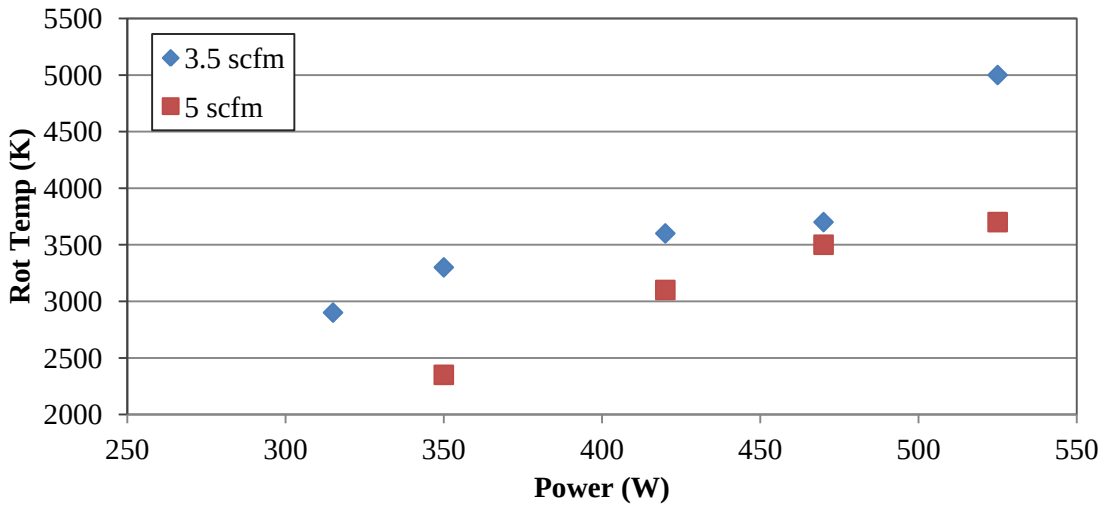

Figure 4.17: Rotational Temperature vs. Power for multiple air flow rates

4.2.2 Spatially Resolved Rotational Temperatures

The previous measurements for the rotational temperature involved taking spectra from the end of the device looking down at the plasma. This results in just one temperature to describe the plasma. However, it is clear from observations that the plasma close to the electrode is more intense than the plasma farther away from the electrode. This indicates not only from intuition but also from the previous data that, brighter areas of the plasma should

have higher gas temperatures as well. Therefore, an experiment was designed to measure the spatial distribution of the plasma.

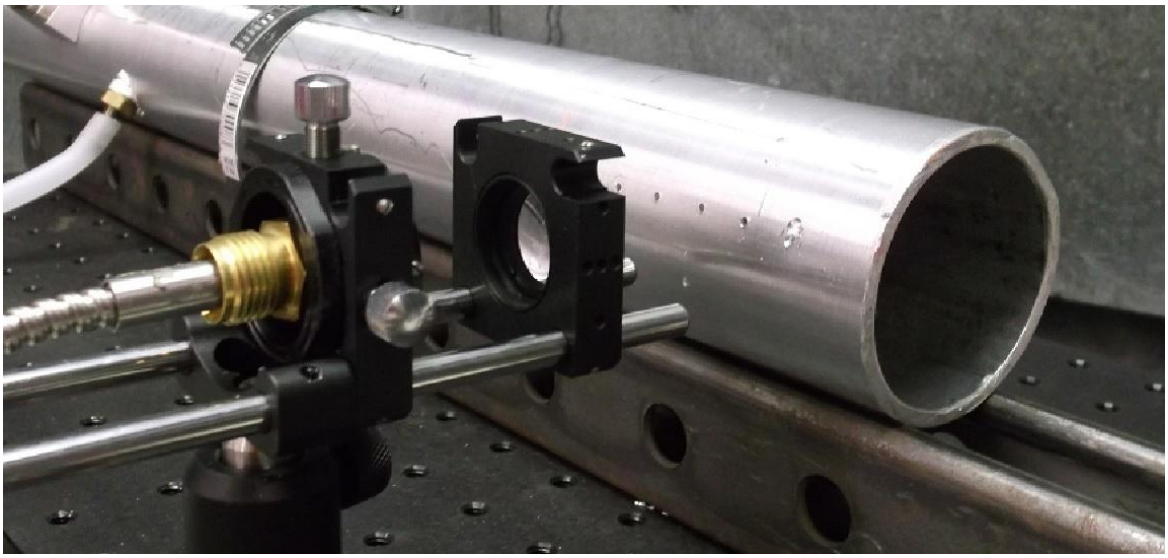

Figure 4.18: Experimental setup for Spatially Resolved Temperature Measurements

This was done by drilling 5 small holes in the device as shown in Figure 4.18.. This method was used instead of just removing the end of the device because as the distance between the electrode and the end of the device decreases, the plasma begins to behave differently. The plasma decreases in both length and radius, and then begins to rotate around on the surface of the electrode as the plasma does not fill an area as large as the electrode. To maintain the same plasma as the previous data, then the spectra must be taken while the plasma remains inside the device. These holes are small enough to have a negligible effect on the airflow in the device. The holes allow for the light emitted from the plasma to the reach the spectrometer. Also, the light coming out of each individual hole can be assumed to be coming from that cross section of the plasma as the ratio between the wall thickness and the whole diameter is relatively large. This allows for only shallow angle light to escape the hole and thus be used for taking the temperature measurements. After the light exits the hole,

a lens collects the light and focuses it on an aperture of a fiber optic cable that then transmits the light into the spectrometer.

The same data as the previous experiments was collected to investigate how the rotational temperature changes with distance from the electrode. Figure 4.19 shows the spectroscopy data normalized to the P-branch peak. Only the two peaks that are used for the calculation are shown here. It is clear that the closest measurement to the electrode has the highest rotational temperature. This is expected as the plasma is more intense in this region. Figure 4.20 shows the temperature estimates derived from the ratio of the two peaks. At 2.54 cm from the electrode the temperature is very large and is in fact larger than the temperature of the previous experiments with similar power levels. These had slightly different delivered powers of 470W vs. 490W here. However, this should not change the temperature too much. The two middle measurements at 3500K and 3200K were close to the temperature measured from the end of the device at 3700K. This indicates that the measurements taken from the end of the device represent an average temperature measurement, and that the plasma does not have one consistent temperature throughout. Finally at 6.35 cm the temperature has dropped of significantly down to 1950K. These measurements correspond to the observations of the plasma behavior as the emission intensity decreases while moving away from the electrode. It seems there are two separate large jumps in the temperature while moving from the electrode. Close to the electrode the temperature is very high, and then falls of significantly to a lower temperature several centimeters away. Then the temperature seems to decrease slower for the next couple of cm. Finally, there is a much quicker decrease in temperature once the distance has increased even further.

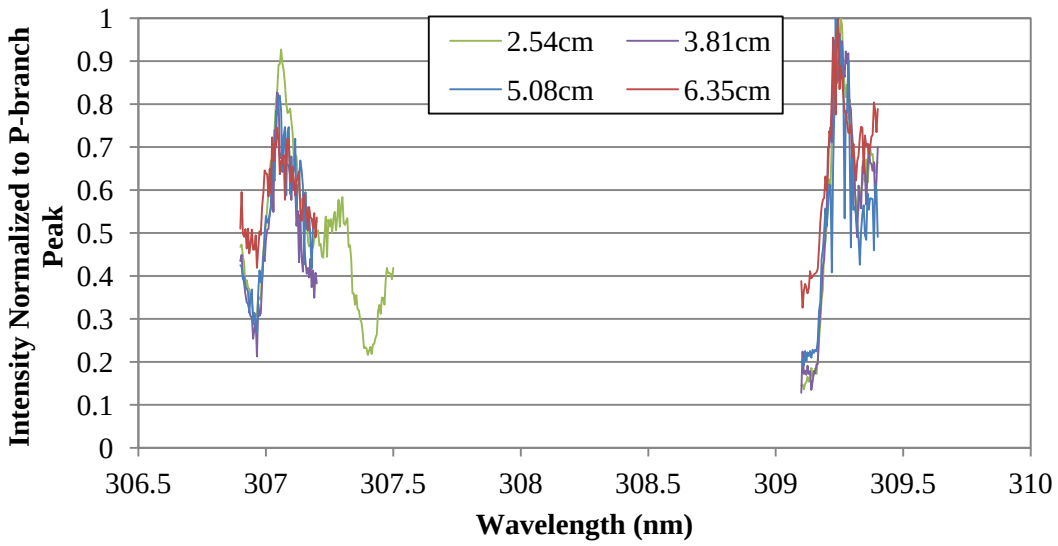

Figure 4.19: Spatial OH Temperature Measurement Spectra

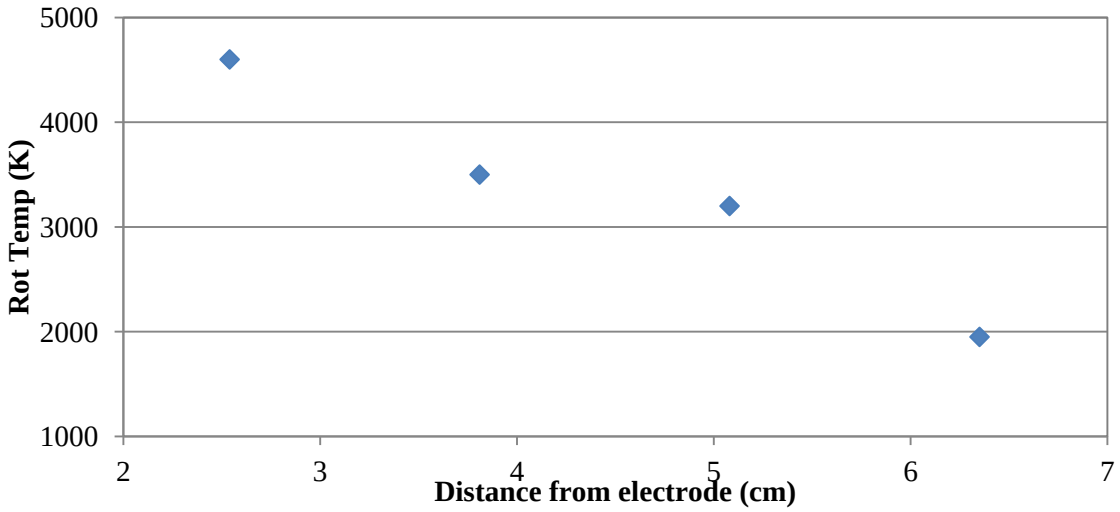

Figure 4.20: Spatially Resolved Temperature Measurements for 490W

Determining how the plasma behaves has a function of distance between electrodes is also important. This could allow for optimizing applications if one particular species is present at greater quantities in a particular region of the plasma. This experiment is done

using the same setup in Figure 4.18. The plasma was operated at 490 W for all of the data presented here. Figure 4.21 shows the spectroscopic data for each distance from the electrode. The spectra closest to the electrode have the most intense emissions as expected. The one interesting thing is that the closest data point seems to actually reduce the OH emissions while enhancing the NO emissions near 250nm. This change in the species in the plasma is also shown more readily in Figure 4.22. This is the normalized spectra that have been truncated to show the data that is relevant to the species in the plasma. Overall, there is a decrease in the intensity of the molecular emissions as compared to the broadband emission and background. The OH peak and the NO peaks drop rapidly with increasing distance from the electrode. The one exception to this is between the 1st and 2nd points from the electrode. The 1st point actually has a smaller OH peak than the 2nd while the NO peaks are significantly larger than those of the 2nd. The lines are almost identical for all the other points indicating that there is a difference between the compositions of the plasma at these points. Several things could be causing this. One could be that the amount of energy needed

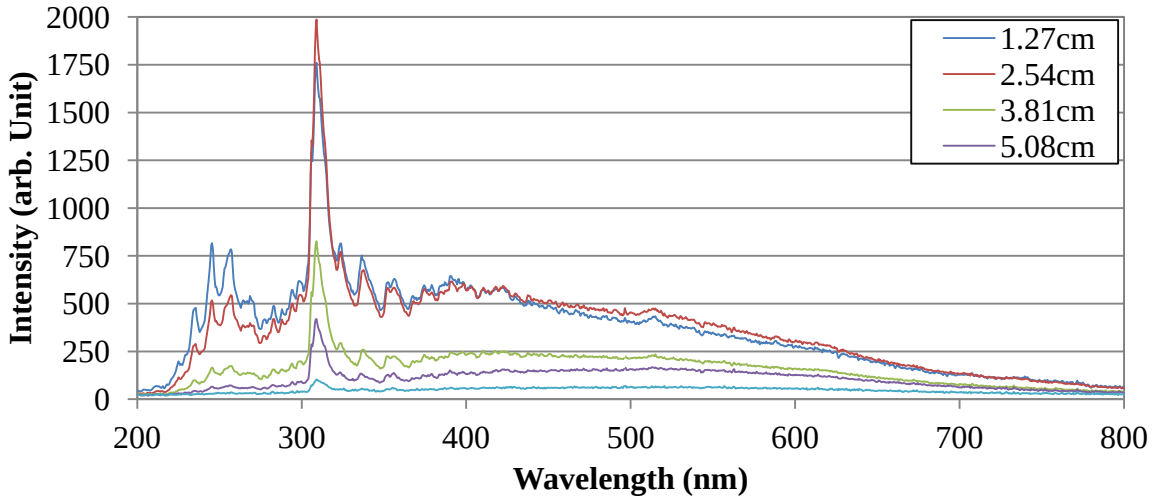

Figure 4.21: Spatially Resolved Spectroscopy Data

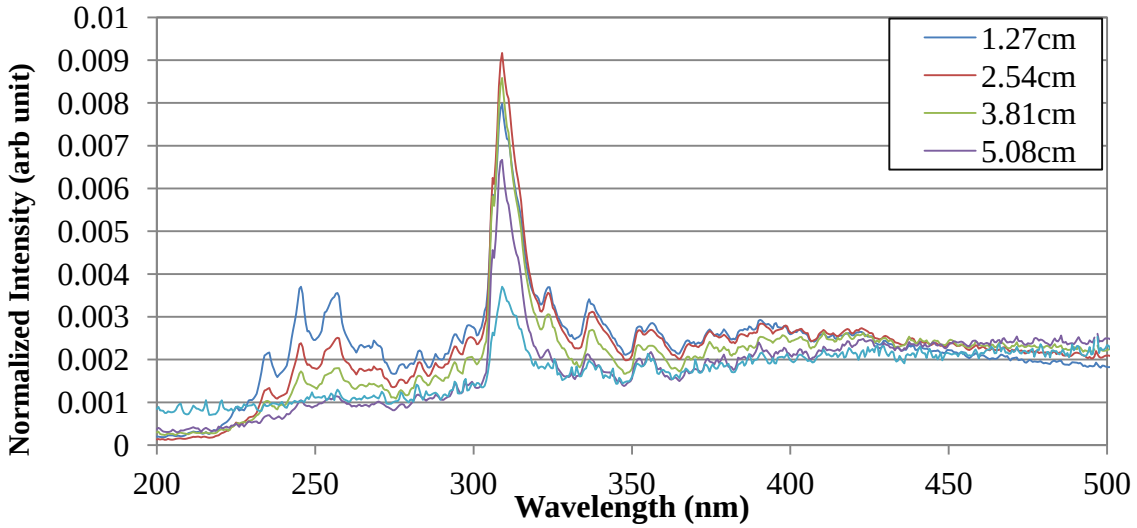

Figure 4.22: Normalized Spatially Resolved Spectra

to form the NO molecules would be higher and therefore these would only form where the plasma is most intense. Another explanation is simply due to the airflow of the system. The OH exists in the plasma due to both the humidity of the atmosphere but also more so from the humidity of the air source. At points close to the electrode the flowing air might not be able to reach this point of the plasma as it streams around the electrode. It could require a small distance before this air reaches the center of the device creating an absence of OH close to the surface of the electrode. This latter explanation seems more fitting as air flow plays such an important role in the characteristics of the plasma.

4.3 Electrode Damage

After extensive operation, the electrode begins to degrade. Bright blue flashes in the plasma occur as some of the aluminum electrode is eroded away and interacts in the plasma. After these flashes are seen, the plasma eventually maintains this blue color. This tends to occur at higher power levels as there is more energy in the plasma along with an increase in the temperature inside the device which weakens the aluminum. Once the plasma is turned off there is a distinct gray layer of aluminum oxide that has formed on the surface of the

Figure 4.23: Damage Occurring on the Surface of the Electrode after Sustained Operation with High Delivered Power

electrode as seen in Figure 4.23. The center of the electrode, where the most intense area of the plasma resided, is where this occurs first, but eventually spreads to the entire electrode if the plasma is continuously operated after it first begins. Figure 4.24 shows the spectrum obtained from the plasma during this phenomenon. The large peak on the left is the atomic lines for aluminum located at 394.4 and 396.15nm. The set of peaks on the right all coincide with the molecular peaks of aluminum oxide [83]. This is an undesirable effect as it changes both the composition and the impedance of the plasma. The aluminum discharge tends to completely dominate all other discharges as the OH peaks near 300 nm can barely even be seen. In any application utilizing the plasma this change in plasma competition would be detrimental to its efficiency.

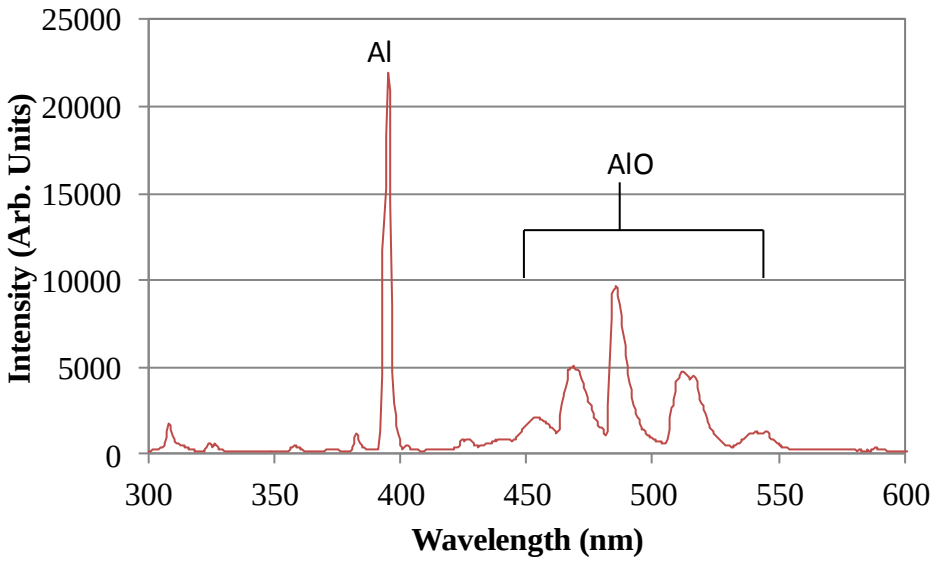

Figure 4.24: Spectrum for Plasma When Electrode is Damaged

4.4 Electrical Measurements

Knowledge of the electrical properties of a plasma are essential for obtaining a better understanding of the plasma itself. Plasma impedance is of utmost importance since it allows for the calculation of a crucial parameter, electron density, when combined with the simple global plasma model explained earlier. These measurements were used to both validate and to improve on the initial plasma model as initially the model did not completely agree with the results that were seen. However, with some minor adjustments to the model these discrepancies were reduced such that the model data and experimental data were in agreement to a reasonable error.

Electrical measurements are made using the onboard phase magnitude pickup on the generator itself. This reads the phase and magnitude of the impedance at the output of the generator. This is then converted into real and imaginary parts in order to be used in calculation of the plasma impedance. Following the circuit leading up to the plasma, including both the cable connecting the generator to the device as well as the components of the devices, and using lossy transmission line theory allows for the calculation of the plasma impedance.

4.4.1 Validation of the Model

In order to ensure that the electrical circuit of the source itself was correct a Hewlett Packard 8753 network analyzer was used to examine the electrical response of the source without plasma. This was actually done before attempting to ignite a plasma in the device. Verification of the device circuit was done by looking at the frequency response of the device without plasma and comparing this with model data to confirm that the device circuit used to calculate impedances can be used, and that the device will have a resonance near 162 MHz. Device response to drive frequencies between 150MHz and 225 MHz was examined by the network analyzer. The resonance of the circuit could then be studied to determine its important quantities such as full width half max (FWHM), resonance depth and q value of the circuit. This was done as well for a range of transmission line lengths and compared to computational data. It was difficult to obtain the exact response between the experimental and model data as there are many minor details that would be difficult to account for directly

Table 4.1 shows both the calculated and measured values for the resonant frequency and depth of that resonance for a variety of different shunt and series lengths. For the frequency of the resonance the measured and calculated data matched up reasonably well. The largest difference between the two is about 3.4%. While this does result in differences in frequency of up to 6 MHz this still represents a good match between the data. It should be noted that by changing either of the series or shunt lengths by as little as 0.25 cm can result in a shift in frequency of about 1MHz. This indicates that even being slightly off with the measured values for the lengths can result in some of the shifts in frequency seen in the data. All data measurements were taken by hand so it is difficult to guarantee accuracy down to the scale of millimeters.

The depths of the resonances were very different. Many of the calculated values are extremely different from the measured values. This difference arises from the ground connection on the shunt end of the device. The contact between the inner conductor and outer conductors is not ideal, so there is a finite resistance, Z_{ground}, at this ground connection which comes into the calculation in equation(4.7). This quantity can affect the depth of the resonance greatly.

Table 4.1: Comparison of Network Analyzer Data and Calculated Model Data

Shunt Length (in)	Series Length (in)	Measured f_{res} (MHz)	Calculated f_{res} (MHz)	%error in f_{res}	Measured depth (dB)	Calculated depth (dB)
2.069	13.4265	139.92	144.4	-3.2018	-1.3	-3.7769
1.229	13.4265	146.68	149.8	-2.1271	-24.2	-16.626
0.53	13.4265	152.76	155.6	-1.8591	-13.5	-1.7829
0.53	11.6765	170.88	171.1	-0.1287	-5.61	-2.2294
1.228	11.6765	163.28	165.2	-1.1759	-3.78	-10.691
2.068	11.6765	154.84	156.5	-1.0721	-13.6	-3.02
2.068	10.3765	168.2	169.4	-0.7134	-5.14	-2.531
1.229	10.3765	173.2	179	-3.3487	-3.22	-7.6352
0.53	10.3765	187.48	187.3	0.09601	-26.1	-2.6945
0.53	12.2765	164.2	166.5	-1.4007	-6.86	-2.0575
1.226	12.2765	157.2	159.2	-1.2723	-3.09	-13.359
2.062	12.2765	149.44	152.06	-1.7532	-7.8	-3.2839
2.062	14.5765	131.6	135.8	-3.1915	-10.3	-4.3758
1.223	14.5765	137.6	141.5	-2.8343	-11.3	-10.497
0.53	14.5765	142.84	146.6	-2.6323	-10.5	-1.563

It is also interesting to look at how the resonances frequency is affected by the changing of the series and shunt lengths. It is clear that these values have a significant effect on the resonant frequency from the data in Table 4.1. To illustrate this, all of the frequencies have been plotted with respect to the series length of the device, with three different shunt lengths in Figure 4.25. The plot shows that there is a decrease in the resonant frequency of the device as the shunt length increases. This plot represents the shunt lengths as well and shows that with the series length remaining the same the frequency increases with shunt length. This trend is confirmed when taking real data with the plasma operating. In order to maintain the best match possible for different input powers, the lengths of the device has to change accordingly. From experiments, it was seen that the series and shunts must be moved in opposite directions from each other. It should also be noted that to optimize for higher power with air it is best to decrease the series length while increasing the shunt length.

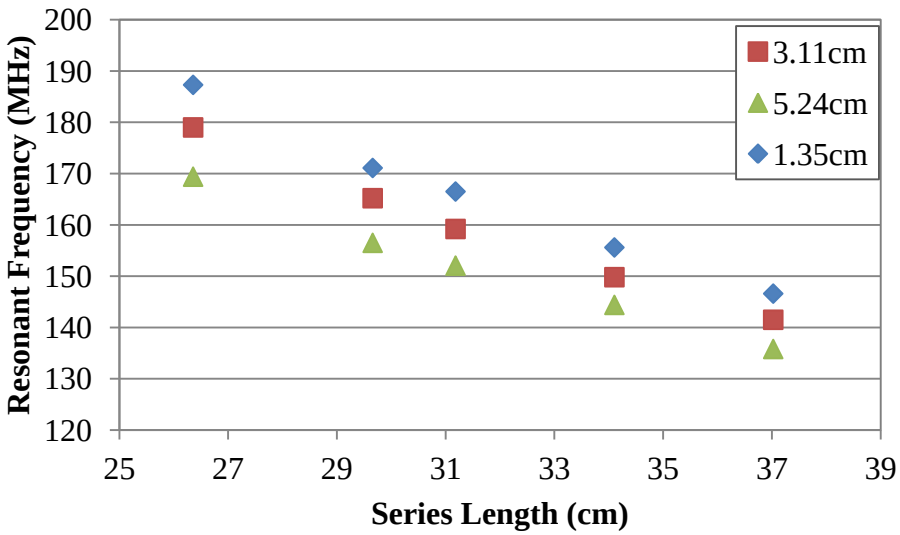

Figure 4.25: Resonant Frequency Changes with Series and Shunt lengths

4.4.2 Plasma Impedance Measurements

The measurements made for calculation of plasma were simply taken from the software that operated the generator. It provides real time measurements of both the real and imaginary components of the impedance at the output of the generator. As the plasma shape is heavily dependent on the airflow of the system, and the airflow is somewhat chaotic, there is a constant variability to this reading of the impedance. There is typically an error on the order of 15-20% which limits the accuracy of the final calculations of the plasma impedance. For a typical measurement, multiple values of the impedance are recorded over some amount of time. Usually at least 5 total measurements are made, sometimes significantly more if the variability seems to be unusually high. A simple average of these numbers is taken to give the number that is used in the calculation of the plasma impedance.

The process for obtaining the plasma impedance is simple as one simply has to follow down the electrical circuit. When calculating impedances of transmission lines using equation 3.3, one tends to work backwards down the line. Figure 4.26 illustrates how the impdance is calculated. Impedances are calculated by following the red arrows and beginning with either Z_p or Z_{ground}. Impedances from these starting points are then calculated

independently until the point where they meet. The calculation would start with the plasma load which would be Z_p. In this situation Z_p is the value that is trying to be obtained, so one

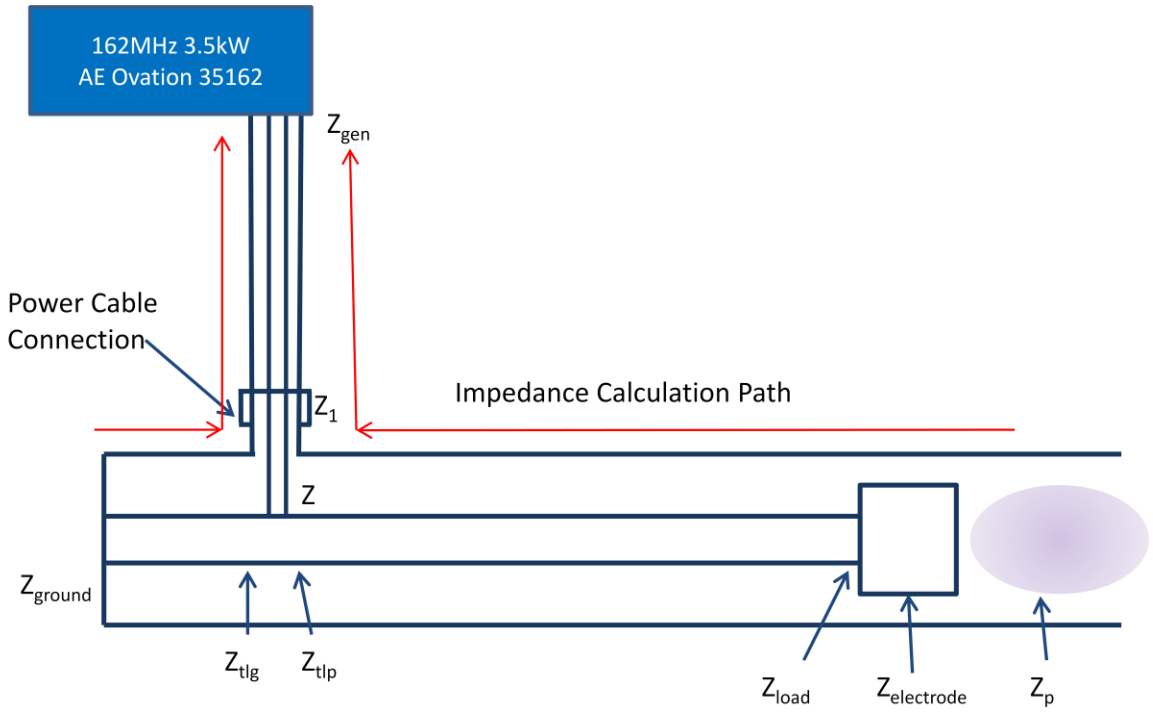

Figure 4.26: Illustration of how the Impedance is Calculated Down the Device

equation is derived that can be solved numerically to give the corresponding value of the plasma impedance. The first step in deriving the equation is to find the impedance that the series leg of the device is terminated to. This includes both the plasma impedance and the impedance that the cylindrical electrode contributes. This term, $Z_{load,}$ is considered the parallel combination of these two impedances and is given by

$$Z_{load} = \left(\frac{1}{Z_{electrode}} + \frac{1}{Z_p} \right)^{-1} \tag{4.3}$$

Where $Z_{electrode}$ is simply the impedance of the electrode acting as a cylindrical capacitor and is given by

$$Z_{electrode} = \frac{1}{i\omega C_{electrode}} \tag{4.4}$$

with

$$C_{electrode} = \frac{2\pi\varepsilon_0 l_{elec}}{\ln\left(\frac{OD}{ID_{elec}}\right)} \tag{4.5}$$

Where l_{elec} is the length of the electrode, 3.8cm, OD is the diameter of the outer tube of the device, and ID_{elec} is the diameter of the electrode. Z_{load} is then put into equation(3.3) as Z_L to find the impedance on the line up to the point where the RF connector is, Z_{tlp}.

$$Z_{tlp} = Z_{tl}\frac{Z_{load} + Z_{tl}\tanh\left(\gamma_{tl} l_{sr}\right)}{Z_{tl} + Z_{load}\tanh\left(\gamma_{tl} l_{sr}\right)} \tag{4.6}$$

where l_{sr} is the length of the series line, $\gamma_{tl} = \left(8.122\times10^{-4} + 3.395i\right)m^{-1}$ is the propagation constant of the device transmission lines, and $Z_{tl} = \left(51.75 - .0072i\right)\Omega$ is the characteristic impedance of the line. These values were derived using equations (3.1)-(3.4). The impedance due to the grounded segment must also be calculated up to the same point, this is done using the following equation

$$Z_{t\lg} = Z_{tl}\frac{Z_{ground} + Z_{tl}\tanh\left(\gamma_{tl} l_{sh}\right)}{Z_{tl} + Z_{ground}\tanh\left(\gamma_{tl} l_{sh}\right)} \tag{4.7}$$

where l_{sh} is the length of the shut leg of the device. Both Z_{tl} and γ_{tl} are the same as before and Z_{ground} is the impedance of the connection between the inner and outer conductors. Z_{ground} is effectively the load of this transmission line, and due to the non-ideal ground connection this does have a finite value of approximately 0.7Ω. This value was chosen due to the circuit ground connection not being ideal and seemed to create the most accurate overall response of the device. Since the grounded plate is required to be able to slide relatively freely, there is a slight resistance measured at this connection between the inner and outer conductors. Once these impedances are known they must be combined in parallel giving

$$Z = \left(\frac{1}{Z_{t\lg}} + \frac{1}{Z_{tlp}}\right)^{-1} \tag{4.8}$$

This gives the impedance where the RF connector meets the inner conductor. The impedance change through the connector is the next point for calculation. Using equations (3.1)-(3.4) with the dimensions of the connector gives both the characteristic impedance, $Z_{rf} = (49.19 - 0.02i)\Omega$, and the propagation constant, $\gamma_{rf} = (0.0021 + 4.92i)m^{-}$` of the RF connector. The dimensions used for these calculations were measured on the connector giving the following: inner diameter, ID_{rf} = 6.7mm, outer diameter, OD_{rf} = 22mm, length, l_{rf} = 5.5cm. Teflon was used as the dielectric between the conductors with a resistivity of $10^{14}\Omega$ cm, and a relative permittivity of 2.1. This leads to the equation for impedance at the input of the device

$$Z_1 = Z_{rf}\frac{Z + Z_{rf}\tanh(\gamma_{rf} l_{rf})}{Z_{rf} + Z\tanh(\gamma_{rf} l_{rf})} \tag{4.9}$$

The final step in this process is to account for the cable connecting the output of the generator to the input of the device. Once again the dimensions of the cable are used to calculate the characteristic impedance and the propagation constant. The cable used is a thermax/cdt MS^2-480. It has an inner conductor diameter of 3.68mm and an outer conductor diameter of 10.67mm. It has PTFE as the dielectric and at 162MHz has the following characteristic impedance and propagation constant $Z_{pow} = (44.05 - 0.039i)\Omega$ and $\gamma_{pow} = (0.0043 + 4.92i)m^{-1}$. Plugging in these values gives the following equation for the impedance at the output of the generator.

$$Z_{gen} = Z_{pow}\frac{Z_1 + Z_{pow}\tanh(\gamma_{pow} l_{pow})}{Z_{pow} + Z_1\tanh(\gamma_{pow} l_{pow})} \tag{4.10}$$

where l_{pow} is the length of the cable connecting the device to the generator. Here l_{pow}= 70.7cm. This value, Z_{gen}, is then the same quantity as the impedance measured by the generator. There may be some error in this due to the wiring leading up to the point of measurement. However, this is assumed to be small and seems to have little impact on the overall impedance of the system. For the most part this should be equivalent to having and additional length of transmission line as most of the connections would have impedances of

50Ω at the frequency the generator operates at. Equation (4.3)-(4.10) can all be combined into one large equation that can be solved directly for the the plasma impedance. However, it is much simpler to just solve this equation numerically. MathCAD is used for this calculation and can be done for any given set of impedance measurements coupled with measurements for the lengths of both the series and shunt components of the device.

Table 4.2: Impedances Measurements at Generator Input for a Variety of Gases

Power(W)	Air (Ω)	CO_2 (Ω)	Nitrogen (Ω)		Power(W)	He (Ω)
385	45.82-16.26i	49.26-73i	44.38+1.56i		245	64.26-54.67i
420	46.019+1.2i	55.18-59.4i	38.28+9.37i		280	64.71-43.4i
455	45.06+1.89i	53.14-46.17i	36.83-12.77i		315	63.93-32.37i
490	42.43+10.59i	50.52-42.33i	40.74+19.45i		350	62.36-24.7i
525	40.42+16.87i	47.41-27.17i	39.90+21.82i		385	60.75-17.15i
560	38.25+21.29i	44.07-18.63i	42.92+23.2i		420	59.03-10.55i
595	36.40+24.98i	42.11-5.88i	46.37+23.33i		455	57.49-5.23i
630	35.23+28.24i	40.08+3i	46.41+27.8i			

This process was done for the all the gases used in this device except for argon. The response of argon in the device was so different that the model would have to be changed significantly, and difficult to verify the validity. Table 4.2 gives a representative case of the impedance read by the generator for several gases over a range of powers. Helium is separated because it required operation at lower power levels, as it would tend to break down into an arc for higher power levels. These values are then used to calculate the plasma impedance for each gas by inputting these impedances as Z_{gen} in equations (4.3)-(4.10)

These impedances are used to calculate the plasma impedance but first, a comparison with the model data was done. Figure 4.27-Figure 4.30 show this comparison for the four gases used: Air, CO_2, He, and N_2. In each plot the red diamonds (♦) represent the model data

and the blue squares (■) represent the experimental data. The graph shows the impedances on a smith chart as seen by the generator. To produce the model data a range of electron densities between 10^{9}-$10^{14}$$cm^{-3}$ along with the corresponding shunt and series lengths that were used for the particular experiment were input into the model to determine the impedance of the system at the generator. All data was then plotted on a smith chart so that a visual representation could be achieved. In all cases the actual lengths of the shunts and series segments were initially set to the experimental data, but were changed slightly to obtain the closest fit to the data. These minor changes amounted to a maximum change in the lengths of about 1cm. This difference is acceptable as the amount of error associated with both the device and the plasma can account for this. Figure 4.27 shows the data for the an air experiment where the shunt length was 5.436cm and the series length was 28.143cm while the model data had lengths of 5.30cm and 28.15cm.

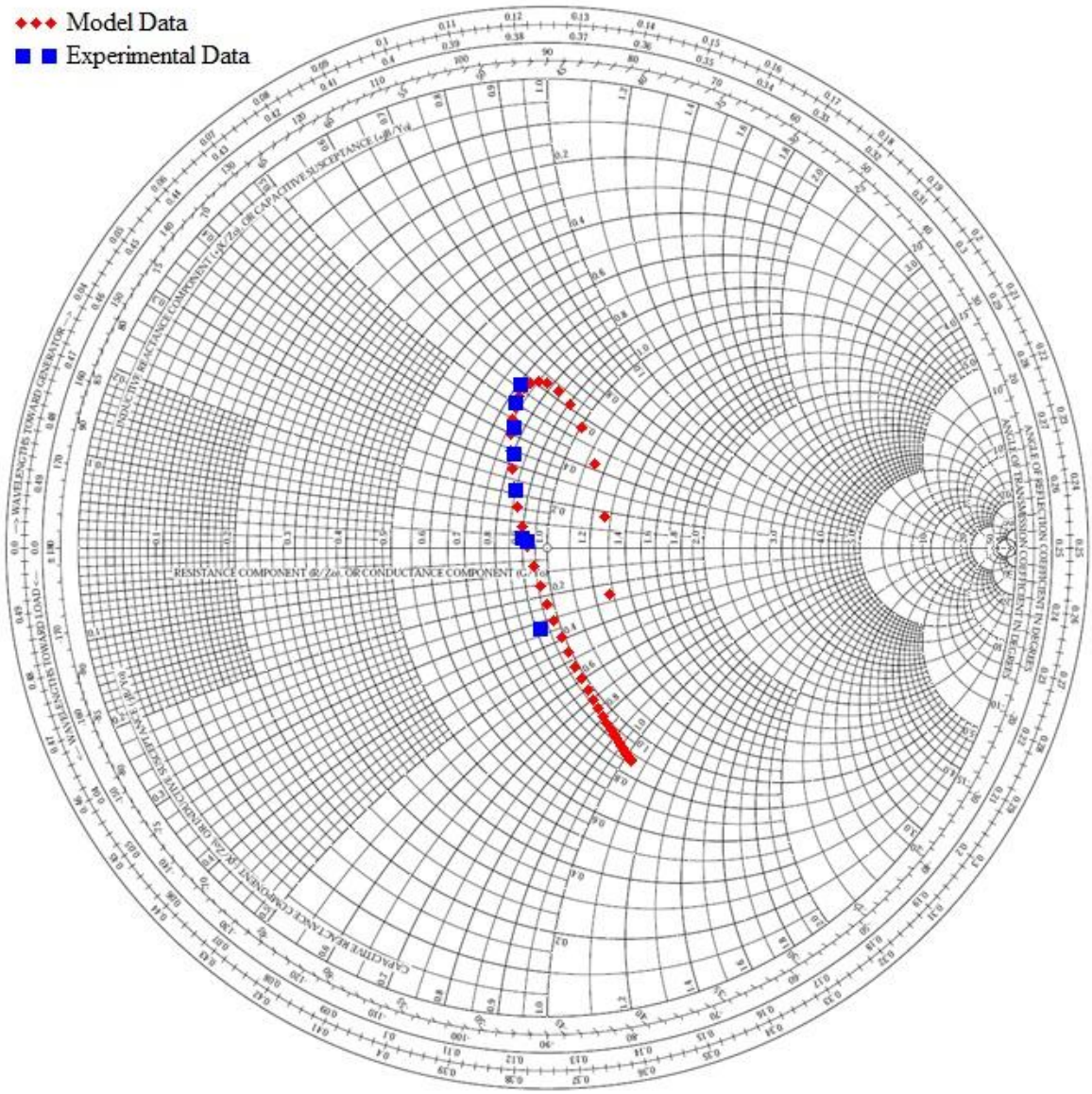

Figure 4.27: Comparison of Experimental and Model Generator Impedances for Air

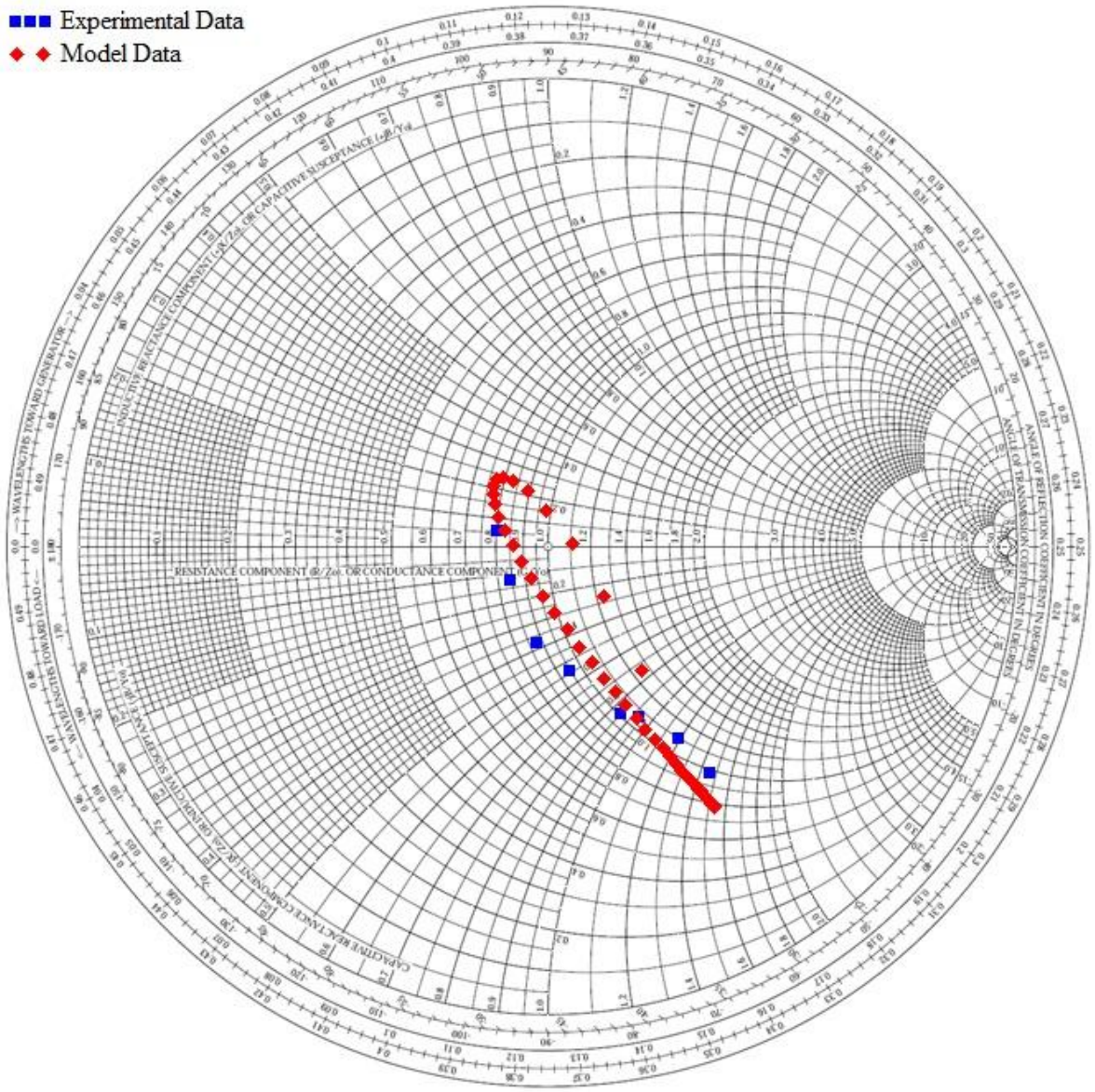

Figure 4.28: Comparison of Experimental and Model Generator Impedances for CO_2

Figure 4.28 is the comparison for CO_2 with experimental shunt and series lengths of 4.67cm and 29.08cm vs. model lengths of 4.67cm and 28.93cm.

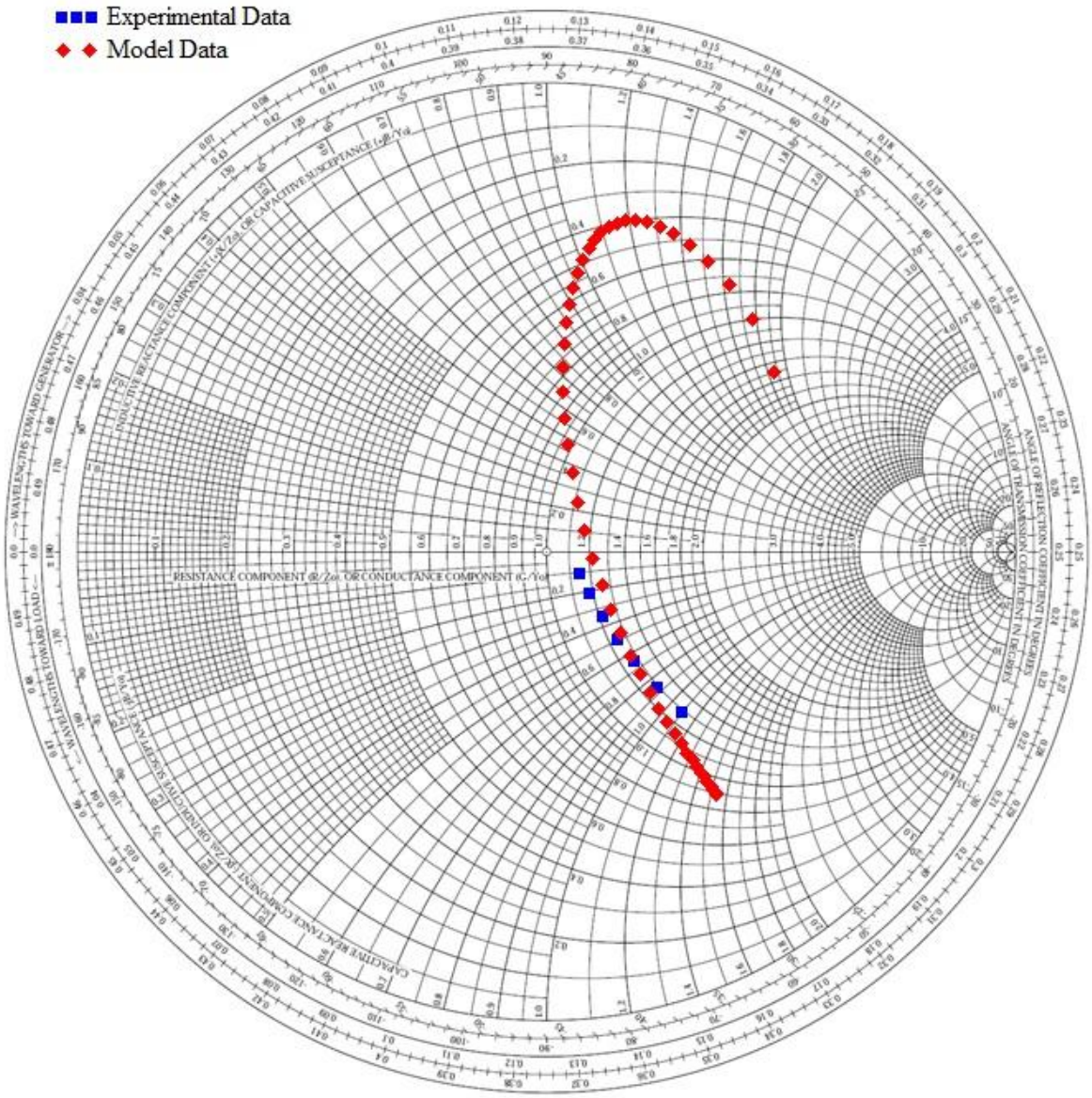

Figure 4.29: Comparison of Experimental and Model Generator Impedances for He

Figure 4.29 is the comparison for He with experimental shunt and series lengths of 5.94cm and 29.08cm vs. model lengths of 6.30cm and 29.13cm.

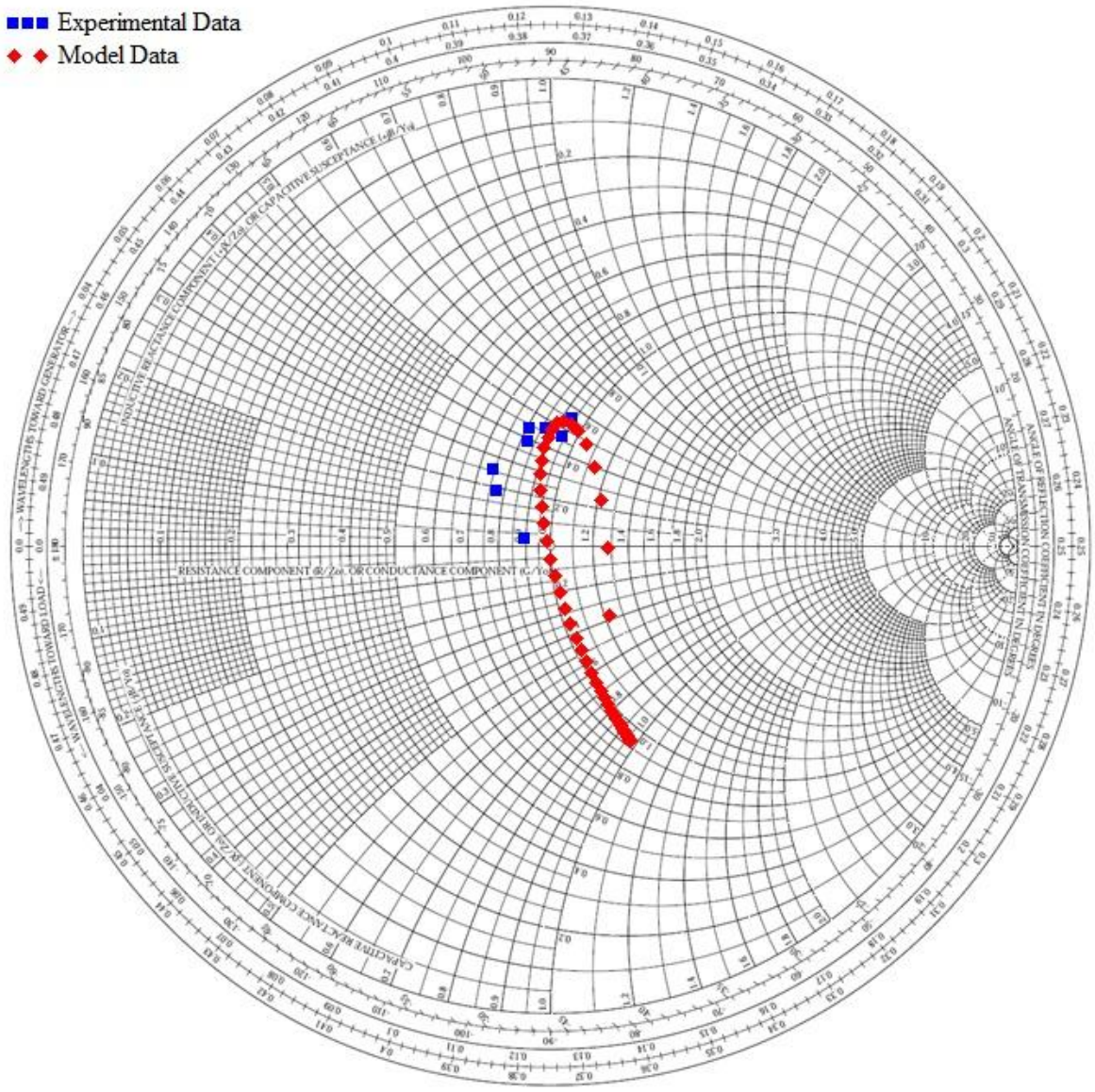

Figure 4.30: Comparison of Experimental and Model Generator Impedances for Nitrogen

Figure 4.30 is the comparison for N_2 with experimental shunt and series lengths of 5.54cm and 27.99cm vs. model lengths of 5.44cm and 28.07cm. Overall, a decent match was able to be produce for all of the gases. Interestingly, nitrogen was the worst overall match between the experimental and model data. It was expected that nitrogen and air would react similarly as nitrogen is the main component of air, but these two gases had different

responses. While the two gases are similar, it was seen from the spectroscopy data that the active species in the plasma are quite different, as OH and NO_x species tend to dominate the discharge. For the helium discharge a slightly different electrode was used than in the rest of the experiments due to its propensity to arc to the walls instead of forming a glow plasma at the end of the electrode. This electrode removed the relatively sharp corners of the cylindrical electrode and replaced the end of the electrode with a hemisphere. This removed the field enhancements seen at edges that could result in the plasma arcing to the walls. The difference in the electrode is also seen in the plasma calculated plasma impedances because of the effects of the device on the plasma impedance. The curve in the model data is caused by the ballasting effect that helps to sustain the plasma. This point represents the same knee as the one seen in the plot in Figure 3.3.

Table 4.3: Calculated Plasma Impedances for different Gases

Power (W)	Air (Ω)	CO_2 (Ω)	N_2 (Ω)	Power (W)	He (Ω)
385	20.7-258.1i	0.9-271.6i	41.3-264.9i	245	6.4-231.1i
420	37.7-263.5i	4.5-271.3i	57.7-259.3i	280	9.8-230.7i
455	39.1-262.9i	8.1-269.3i	66.2-259.2i	315	13.8-230.2i
490	52.2-267i	9.1-268i	74.5-276.8i	350	17.1-229.7i
525	63.5-273.2i	15.3-265i	80.6-279.9i	385	21-229.4i
560	73.7-279.2i	20-262.4i	76.4-287.8i	420	25-229.3i
595	83-286.7i	30.1-260.7i	69.5-292.5i	455	28.7-229.4i
630	89.7-296.1i	39.9-260.3i	73.8-302i		

The plasma impedances were calculated based on these points where the model most closely matched the experimental data. With only minor differences in the lengths of the series and shunt segments, there were also insignificant differences with the calculations of the plasma impedances between the measured and best fit lengths. These calculations of the

impedance do not depend on any plasma parameters as the only parameters used for the calculations were based on the physical parameters of the device.

4.4.3 Electron Density and Sheath Thickness Calculations

Electron Density and sheath thickness are two quantities crucial for understanding and characterizing plasmas. The plasma impedance provides a means to calculate both of these quantities when paired with the global plasma model described in Chapter 3. As the impedance is a complex number $Z_p = R_p + iX_p$, equations (3.5)-(3.16) are used to create a system of equations that are solved using numerical methods (MathCAD's equation solver). By doing this, differences in how the plasma reacts can be linked back to more fundamental properties of the plasma. Instead of just looking at spectra or other application based data as a function of power, this data can be examined while keeping in mind what is actually going on in the plasma. This allows for a more complete understanding of the plasma. Application of this knowledge can then be used to make improvements or modifications to the device for the use with various applications.

Figure 4.31 shows the calculated densities for each gas that was used. A range of densities between 2.5E10 cm^{-3} and 2.5E13 cm^{-3} were seen between all of the gases. Helium had the lowest electron density of all the gases but this was in part due to the delivered power being significantly lower than for the other gases, although it still had relatively low densities with similar delivered power. This is most likely cause by the large ionization potential of helium paired with the high collision rates of atmospheric plasma. These collisions tend to have a low energy transfer making the ionization of He small compared to other gases. This has also been seen in other atmospheric plasmas [88]. Air and nitrogen had similar densities with nitrogen having slightly higher densities. This difference is caused by the presence of both the oxygen gas in the air as well as the water from the humid air stream. As oxygen is added to a plasma, electron densities typically decrease. Carbon dioxide has an even larger amount of oxygen resulting in a further decrease in the electron density.

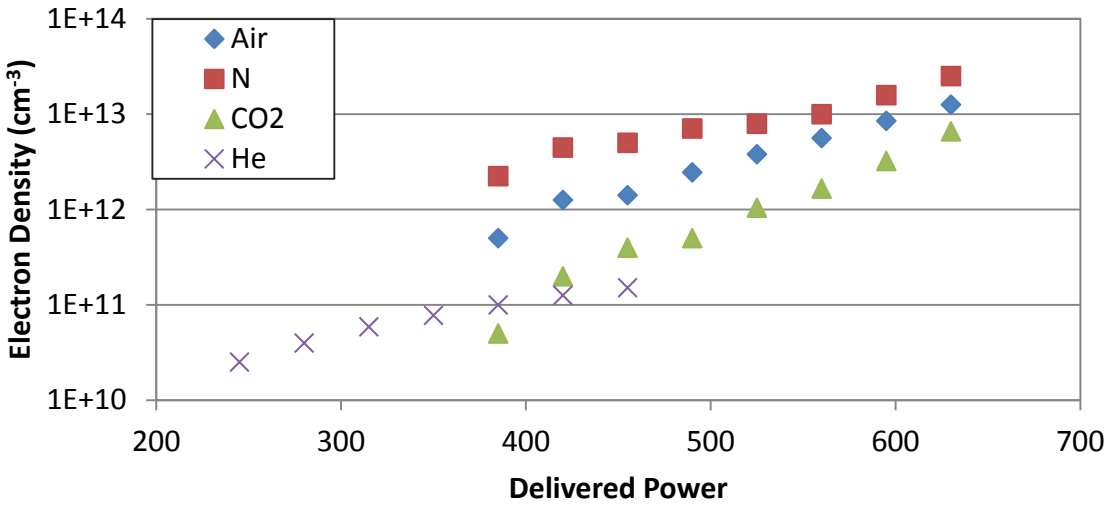

Figure 4.31: Electron Density vs. Delivered Power for All Gases

Now that electron densities have been calculated, a comparison to the model data in Chapter 3 that discussed the VHF ballasting effect can be compared to this experimental data. A plot of both the plasma resistance and reactance versus electron density was made for each gas to compare the data. Figure 4.32 shows the plasma resistance plots for both air and nitrogen. For both gases the model is able to match well with the experimental data. Both have electron densities on the order of $10^{12}cm^{-3}$ and show the ballasting trend necessary for a sustained plasma without the transition in to an arc. Figure 4.33 is the same plot but for helium and CO_2. Once again a good match between the two data sets is found while the helium tends to operate at a much lower density than the other gases. These plots confirm that the plasma impedance increase as the electron density increase, supporting the model prediction of the ballasting effect.

Figure 4.34 is the reactance of the plasma with electron density for both air and nitrogen. Here there is a significant difference in the data. While the air model tends to follow the experimental fairly well, the nitrogen data strays significantly. This is expected as the model was not able to accurately predict the impedance that the generator sees and this is just a result of this. The reactance measurements of the plasma and of the generator

impedance tended to fluctuate more rapidly than the resistances did. Figure 4.35 is the same plot but with helium and CO_2 as the supplied gas. The difference in the two values as electron density decreases is simply due to the electrode that was used for the helium discharge. As the plasma impedance is dependent on the vacuum impedance of the device, equation (3.15), this changes as the shape of the electrode is changed. Model data matched well with the helium reactance. The CO_2 experimental data increased with increasing electron density which is opposite of model predictions and from the other experimental data for the other gases.

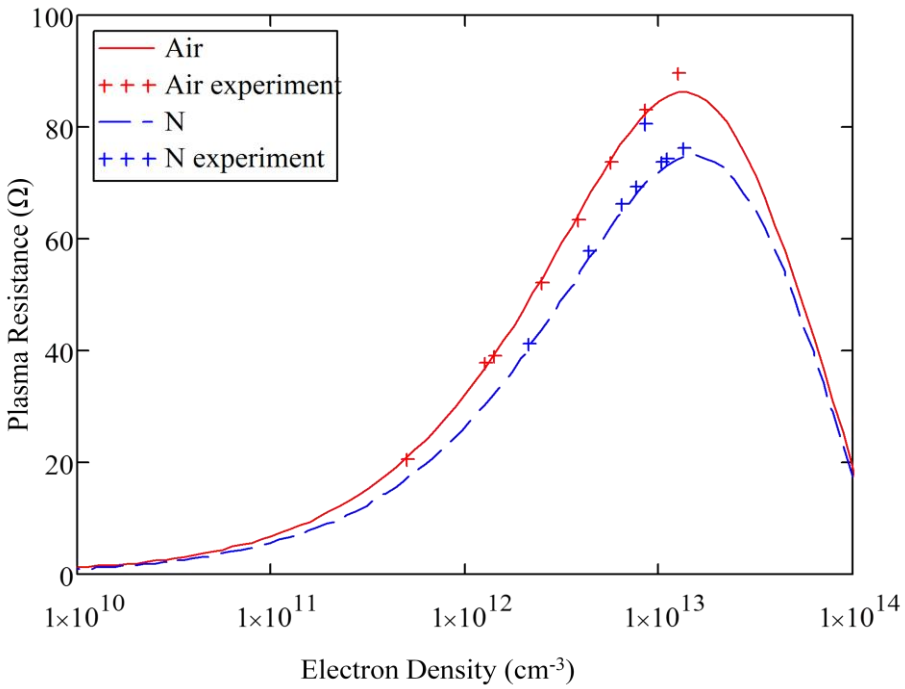

Figure 4.32: Plasma Resistance Vs Electron Density for Air and Nitrogen

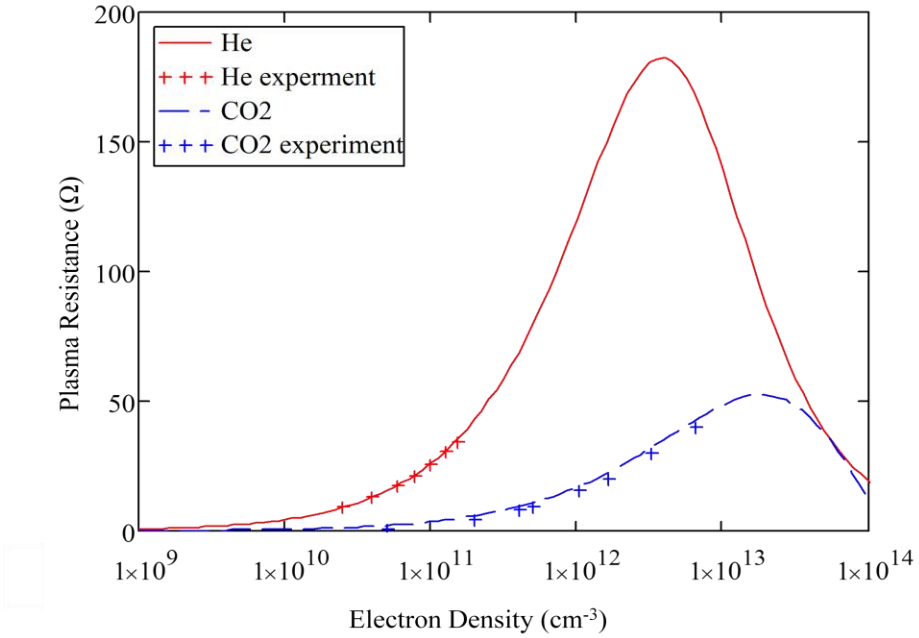

Figure 4.33: Plasma Resistance vs. Electron Density for He and CO_2

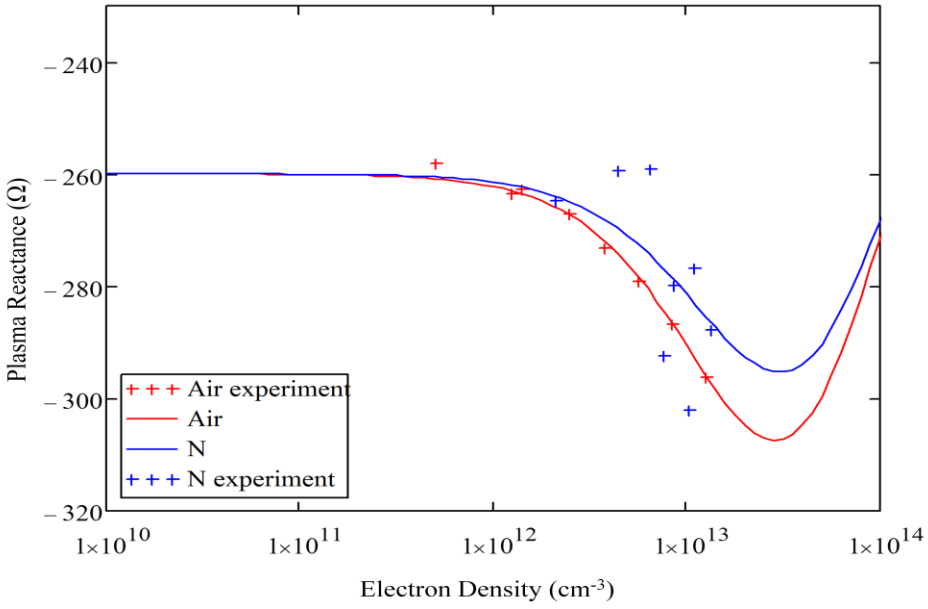

Figure 4.34: Plama Reactance vs. Electron Density for Air and Nitrogen

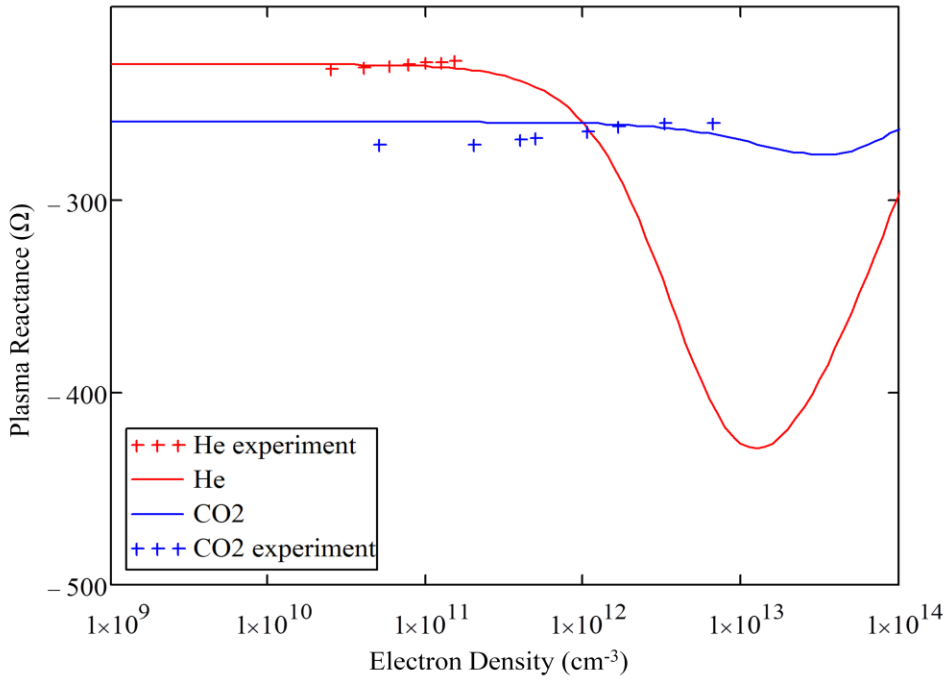

Figure 4.35: Plasma Reactance vs. Electron Density for He and CO_2

4.4.4 B-Loop Probe

The b-loop probe is a very simple probe used to determine the current in the plasma. The probe is simply a conducting loop that is inserted into the device next to the plasma. A ceramic shield is used to prevent direct electrical interaction with the plasma. There is an oscillating current due to the RF waveform powering the plasma resulting in an oscillating magnetic field being produced. This magnetic field then passes through the b-loop probe and produces an electrical current in the probe according to faraday's law. This signal is largest when the probe is oriented so that the normal vector of the loop is parallel to the direction of the magnetic field, and falls to zero when perpendicular and no magnetic field lines pass through the loop. An oscilloscope connected to the end of the probe displayed the current in real time and allowed for the measurement of the voltage of the signal, which can then be used to calculate the current in the plasma. Figure 4.36 shows the output from the oscilloscope.

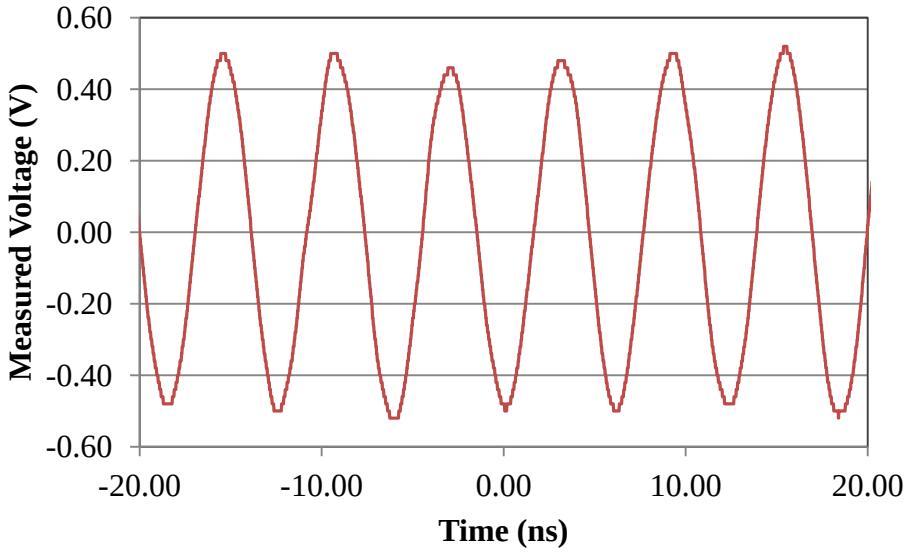

Figure 4.36: Oscilloscope Data Taken With B-loop Probe

The oscillating magnetic field through the loop probe created a maximum potential of 0.5V. Utilizing faraday's law the maximum induced potential for an oscillating magnetic field through a loop is:

$$\varepsilon = NBA\omega \tag{4.11}$$

Where N is the number of turns of coil, ε the potential, B the maximum value of the magnetic field, A is the area of the probe and ω is the frequency of the oscillation. The probe used has one turn and the area can be calculated assuming the loop is an ellipse with major and minor axes that are 6.49mm and 2.86mm respectively giving a total area of 58.259mm^2. This equation is solved to find the magnetic field generated by the plasma. Using Ampere's law, equation (4.12), the current needed to generate this magnetic field is found to be 0.54A

$$B = \frac{\mu_0 I}{2\pi r} \tag{4.12}$$

r is the distance from the center of the plasma to the probe. This current value is simply the peak value for the oscillating current in the plasma.

This experiment was also useful in the determination that the plasma is indeed glow plasma and not sustained by arcs or streamers within the plasma. As Figure 4.34 shows, there are no spikes or other irregularities in the signal. If there were arcs or streamers in the plasma there would be visible spikes throughout the overall signal as well as an overall shape that deviates from the sinusoid observed here.

4.5 RF Matching Network

Understanding the response of the device to multiple plasma conditions is integral for the further development for future applications. It has been shown that his device can run multiple gases but it requires slight modification of the lengths of transmission lines. Furthermore, for different applications there could be a variety of different plasma conditions necessary for a particular process. The need to be able to design for a specific process with different gases, electron densities or area of application is crucial for the improvement of the device.

4.5.1 Q-Value

The q-value represents the ratio of the stored energy in a system to the energy dissipated for a resonator circuit. A high q in a resonator circuit indicates a high performance of a circuit as very little power is lost in the circuit while maintain the stored energy [79,80].This is also true for many plasma systems in use today as this indicates that the greatest amount of power is delivered to the plasma. However, a large q also results in a high response of the system to any changes that occur which could lead to failure of the plasma circuit which makes matching networks in plasma systems essential for its operation. In this system a low q value is used. Instead of this meaning that the energy dissipated in the system is high, the low q is obtained by reducing the amount of stored energy. This low q value results in a broad resonance with respect to the different parameters of the system, allowing the match to be able to tune through perturbations in parameters such as electron density. Therefore, there are not large changes in the system response which would result in the failure of power to reach the plasma.

Frequency Q-value can be approximated by comparing resonant frequency with resonance width in frequency space. A resonance where the reflected power is decreased significantly can be see around 162MHz depending on the lengths of the transmission lines. The q value is estimated as the frequency at which the resonance occurs divided by the FWHM of the resonance. This value is obtained using the electrical circuit model described in section 3.2 and is evaluated over several changing parameters of the system. Figure 4.37 shows an example of three representative q values that were easily generated with the device. The response of the system for changes in transmission line length, feed gases, power, electron density, and characteristic impedance of the device is discussed. All of the discussions involve the use of air as the feed gas except when it is explicitly noted that a different gas is being used during operation.

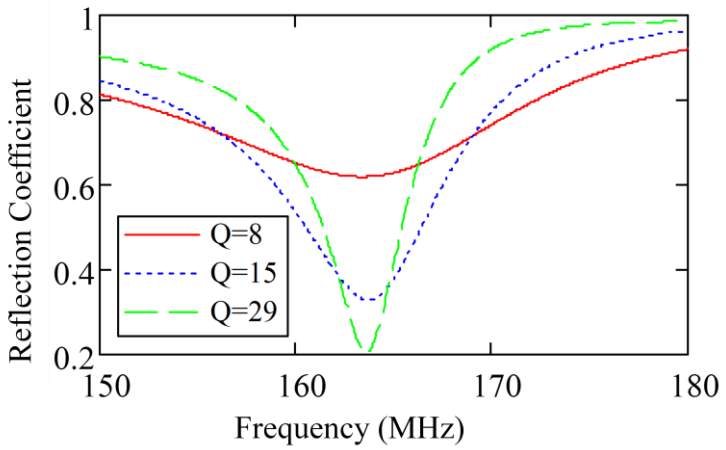

Figure 4.37: Device Electrical Response without Plasma for Different Q Values of the System

The most straight forward way to alter the Q-value of the system is by changing the lengths of the transmission lines in the device. Figure 4.38 illustrates what parts of the device are changing in this situation. These changes are easy to make as the inner conductor is free to slide if the clamp that connects the inner conductor to the RF connector is loosened. This is done by simply loosening a screw that can be accessed through a hole in the side of

the device. While in operation this hole is covered with electrical tape. The grounded termination can simply slide back and forth at any time and can be easily changed while the plasma is running to improve the reflected power levels.

Figure 4.38: Illustration for the Changing of the Lengths of the Series and Shunt Segments

The first parameter studied is the power delivered to the system. This parameter is heavily linked with the electron density as the density increase with an increase in power. In this study, the device was operated for a range of powers between 380 and 700 W. The lengths of the transmission lines were changed so that the minimum reflected power (~0-5W) was obtained for each individual power level. These lengths were then input into the electrical model and q-values were obtained. Figure 4.39 shows the resulting q-value vs. power on the left and q-value vs. electron density on the right. Electron densities were calculated using the plasma model along with the electrical model for the particular configuration. There is a clear trend in q-value with power and thus electron density as the two variables change similarly. A higher q-value is necessary to be able to run the device with a lower electron density. This trend helps to illustrate how to plan for a specific device in the future. If a particular process desires a certain electron density, while maintaining low reflected power, this can be achieved by simply changing the lengths of the two transmission lines. It requires no separate matching network allowing for the device to still remain relatively portable to be used for the application.

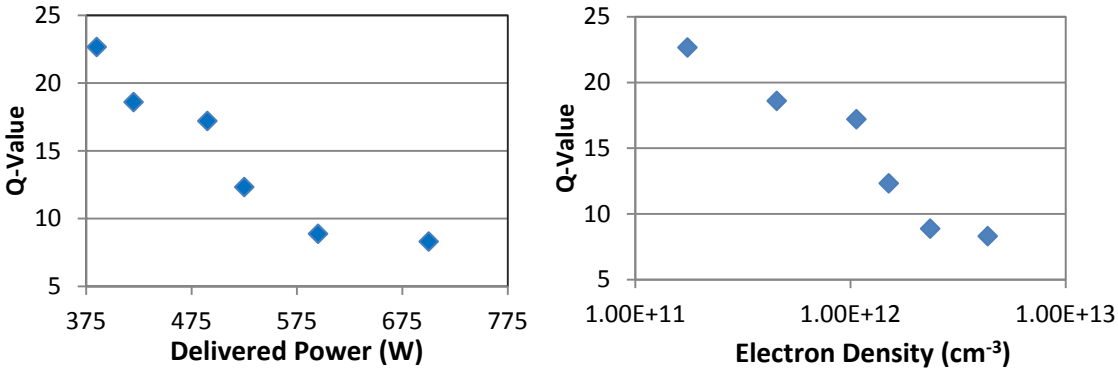

Figure 4.39: Comparison of the Q value of the circuit with Delivered Power and Electron Density

The characteristic impedance of the device is another potential change that could be made to the device. Equation (3.1) gives the characteristic impedance of a coaxial transmission line, and is determined by the ratio of the diameters of the inner and outer conductors of the line. Figure 4.40 illustrates would be physically changing in the device. Electrically it is only the ratio of the diameters that matters, therefore this device could be made into a much larger device with the ratio of diameters. However, this neglects how the

Figure 4.40: Cross Sectional Cut Showing Diameters of Inner and Outer Conductors

plasma would change in size and impedance. Figure 4.41 shows how the circuit responds to changing electron densities. The sharpest resonance is when the line impedance is 71Ω. The current device operates at 51Ω and has a much broader resonance. The broader resonance is actually desired to allow the device to be able to handle perturbations in electron density without a significant change in the electrical response.

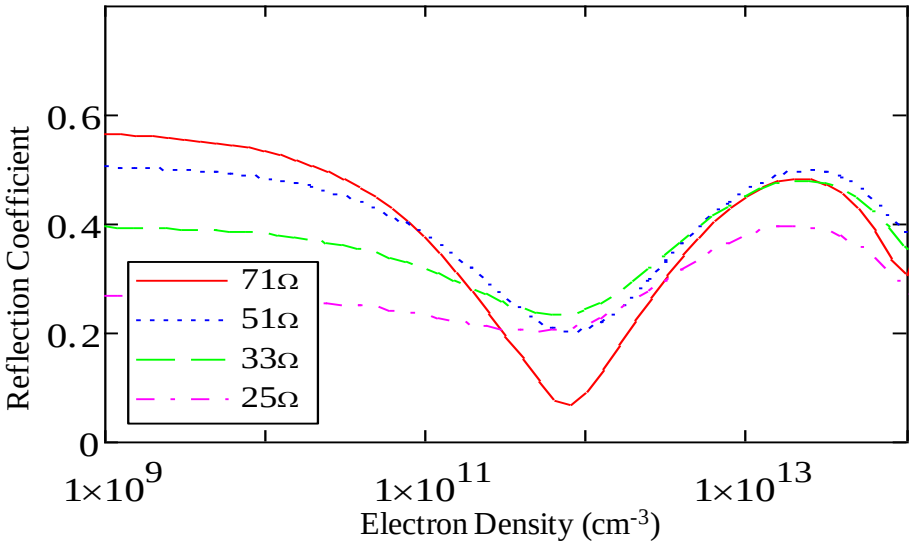

Figure 4.41: Reflection Coefficient vs. Electron Density for Various Device Characteristic Impedances

The final physical change to the device is changing the size of the electrode at the end of the device as shown in Figure 4.42. Obviously, the upper limit of the electrode diameter is

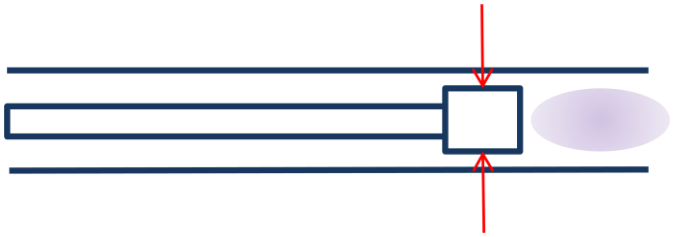

Figure 4.42: Illustration of Change in Electrode Size

set by the diameter of the outer conductor, but the size of the device is not regulated by the electrical circuit and could potentially become larger if necessary. For this study, three different electrode diameters were used: 2.8 cm, 3.5 cm, and 4.1 cm. All three scenarios are done assuming the outer conductor of the device remains constant at 3.5 cm is the dimension

of the current device in use today, 5.27cm. In the electrical model of the device the electrode generates an impedance that is in parallel to the plasma as it acts as a cylindrical capacitor with an outer radius equal to the radius of the outer tube of the device. There are two scenarios to consider with regards to how the plasma responds to a change in the electrode diameter. The first is that the plasma changes its size based on the electrode size. It would increase its diameter with increasing electrode diameter, and similarly decrease its diameter with the electrode. The second option is that the diameter of the plasma is dictated more by the outer conductor size and airflow. Figure 4.43 shows the first scenario where the plasma size changes with electrode size. According to the data a larger electrode radius results in system that is best matched for higher electron densities. This could then be used for making a specific device for an application that would require a smaller or larger radius for plasma application on a substrate. Figure 4.44 shows the second scenario where plasma radius is independent of the electrode size. There is very little change in how the system responds to this change as the capacitance from the electrode plays a relatively minor role in the overall system response. However, if this scenario is the correct way of looking at the plasma, then changing the radius would do little good in the first place. The main goal any of these changes would be to alter the plasma so that it could be used in a situation where it would need a larger or smaller surface area to interact with. So if there is no change in the plasma then there is little need to change the size of the electrode.

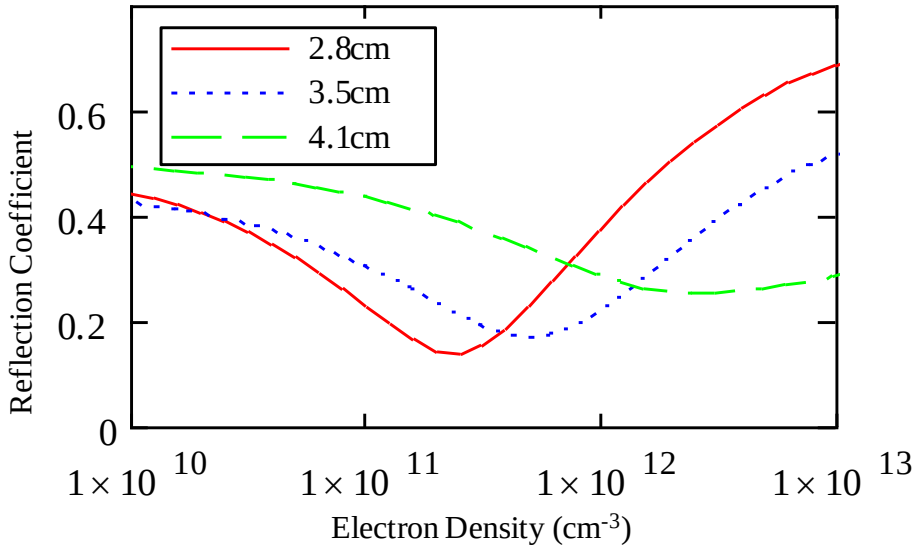

Figure 4.43: Response of Device with Changing Electrode Diameter Assuming Plasma Diameter Changes Accordingly

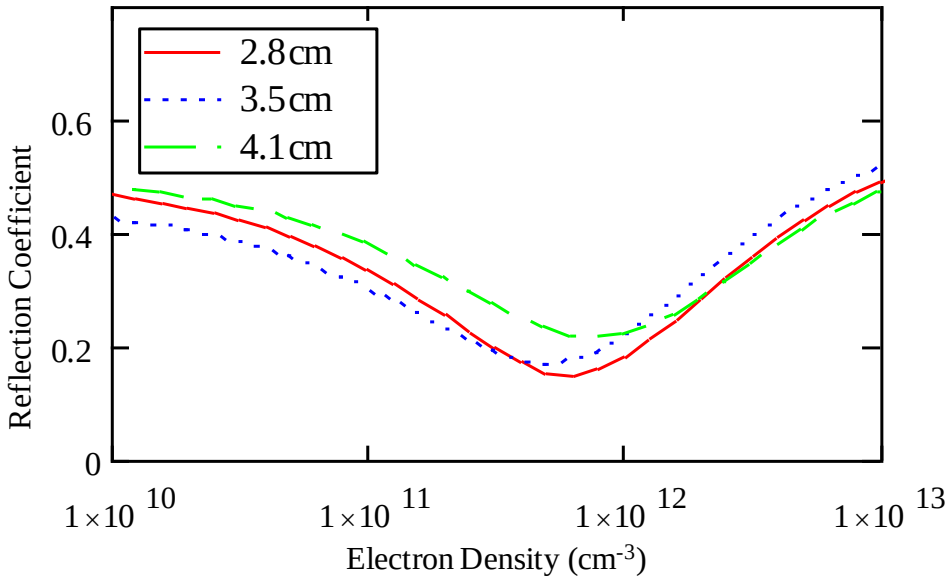

Figure 4.44: Response of Device with Changing Electrode Diameter Assuming Plasma Diameter Remains Constant

Feed gas is another important parameter for this device. Although the device is capable of running a multitude of gases, there is still a significant change in plasma impedance when different gases are used. This arises primarily through the differences in the collision frequency of the gas. How, the collision frequency is obtained is shown in section 3.2.1. Figure 4.45 shows how the match responds to collision frequency changes. Three values of q are looked at: 6, 14, and 27. The graph shows the reflection coefficient versus the collision frequency for each of these values. The collision frequency with the best match tends to increase as the q of the device increases. This can be compared to experimental data as the best match has been found for He, Air, N_2, and CO_2. The lengths of the transmission lines at this point were recorded and the q value of the circuit was calculated from this. Figure 4.46 shows the q-values plotted against the relative polarizability of the corresponding gas [89,90]. As shown in section 3.2.1, the polarizability is proportional to the collision frequency and thus scales with it. Gases with higher relative polarizability, and thus higher collision frequency, have a higher q circuit for the optimal match of the system. To avoid any other parameter altering these values all of the gases were ran with the same set of parameters. These data points were all taken with power levels of 420W, and each was able to be maintained with less than 15W reflected at any given time. The trends of both the experimental and model data match up. As helium has the lowest polarizability and lowest collision frequency it has the lowest q value. Conversely, CO_2 has the highest collision frequency and thus has the highest q value. This is useful since this informs decisions made on how to determine the lengths of the device when a new gas is introduced to the system. As long as the collision frequency can be estimated for the gas the approximate dimensions of the device can be determined before any experiments are run using that gas.

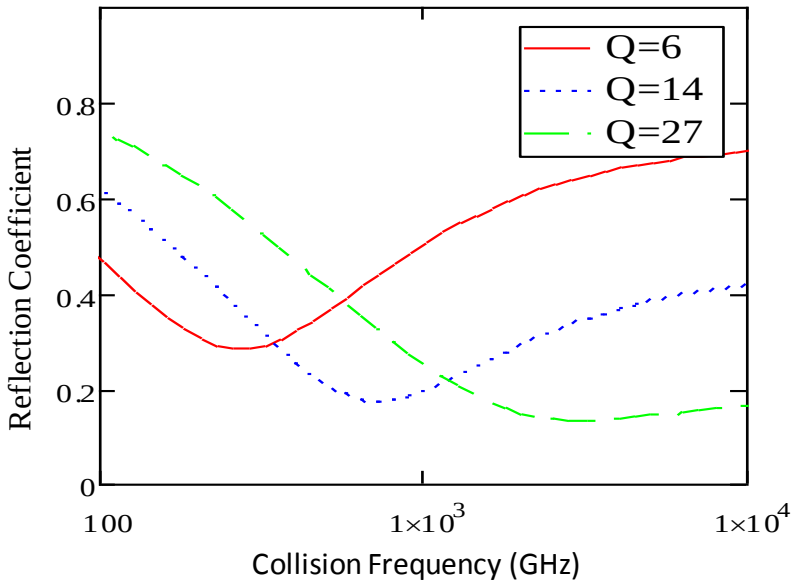

Figure 4.45: Reflection Coefficient vs. Collision Frequency for Different Q values

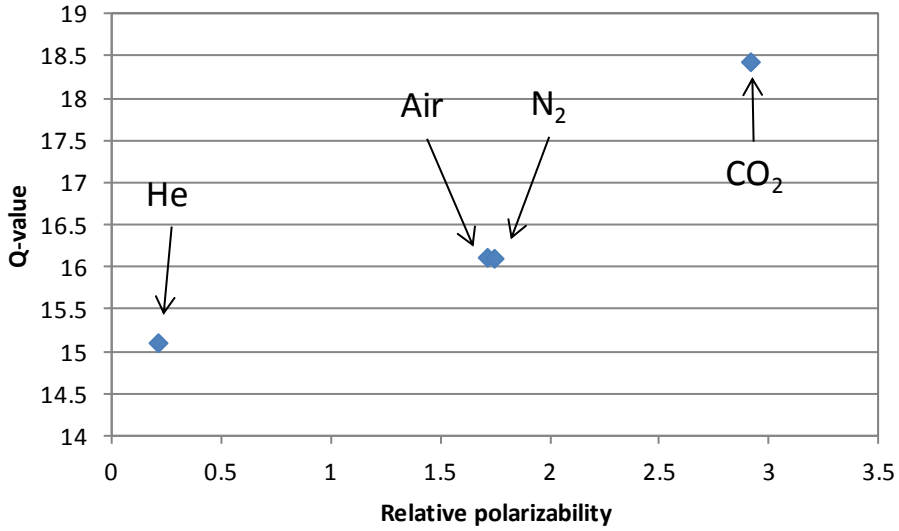

Figure 4.46: Q Value vs. Relative Polarizability

Chapter 5: Simultaneous Operation of Multiple Devices

In Chapter 4, the various plasma diagnostics used to characterize the plasma were discussed. This included OES to determine rotational temperature and gas identifications, as well as electrical measurements for electron density calculations. This chapter demonstrates the extension of the VHF source to parallel operation to enable larger processing and improve throughput

Parallel source operation is a must in order to increase the effective rate of treatment for any application. Generator cost per Watt has a baseline upfront cost for chassis, circuit boards, controllers, etc. and then increases linearly with maximum delivered power. Therefore, parallel operation of a plurality of sources off of a common power supply presents tremendous economic benefit compared to individually driven sources. Additionally, the use of a single generator reduces the number of components prone to failure, increasing the reliability and uptime of a larger scale system. As there is already a large generator on the market and used for this device that could power multiple devices simultaneously, the most straight forward way of doing this is running several devices side by side all off of the single generator. As the device only uses on average about 500W for most of the applications tried in this work, the generator in used could ideally run up to 7 devices at once.

The process of scale up begins more modestly and only two sources are used to illustrate the effects of parallelization of the sources. To connect the devices a cable coming from the generator is connected to a tee connector. Then two more power cables connect the tee to each device. The main concerns are reflected power, how the power is delivered to the two devices, and how parallel loading of the power distribution system impacts source geometry and operation

5.1 Parallel Combination of Sources

The first challenge is to ensure that the devices are able to run with minimum reflected power. This is relatively straight forward as the model for the plasma has been developed for a single device, and now it is simply combining the two devices' impedances in parallel. The

combination of impedances in parallel uses an equation similar to equation (4.3). From the previous experiments the devices are setup such that an impedance of 50Ω is achieved for a variety of input powers. The impedance of the system is e accounted for and calculated going from the two devices to the tee, and then along the final cable connecting to the generator. If the impedance of the device is at 50 Ω, without any reactance component, then the impedance remains the same at the end of the cable connecting the tee. The cables are 50Ω and only result in a change in the phase angle of the impedance. If this is the case then the new impedance after the tee is given by:

$$\left(\frac{1}{50\Omega}+\frac{1}{50\Omega}\right)^{-1}=25\Omega \tag{5.1}$$

This is a significant change in the impedance and results in relatively large amounts of reflected power due to the poor match. Therefore, adjustments must be made to the source configuration with regard to shunt and series transmission line length to realize an impedance for one device resulting in a 50Ω impedance after the combination of the two impedances. This requires that the impedances at the input of the tee for each device must be equal to 100Ω. It is assumed that each device has identical parameters and identical plasmas so that the impedances are identical. This can be extrapolated further to calculate the necessary impedances for any number of simultaneously running devices. Looking at equation (5.1) for an arbitrary number of devices n to give a total impedance of 50Ω results in

$$\left(\frac{1}{Z}+\frac{1}{Z}+...+\frac{1}{Z}\right)^{-1}=\left(\frac{n}{Z}\right)^{-1}=50\Omega \tag{5.2}$$

which results in the simple relation between the number of devices and the desired impedance at the tee input to produce a stable match.

$$Z=n50\Omega \tag{5.3}$$

From this the dimensions of the device necessary to produce an arbitrary number of devices, n, all operating with plasmas at a given electron density is found. For example, the case of two devices running simultaneously with electron densities of 10^{12} cm^{-3} is used determine the lengths of the device parameters necessary for a matched system. For n=2 the desired

impedance at the input of the tee needs to be 100Ω. As transmission lines change the impedance in such a way that only the phase angle changes, there are numerous device impedances that could be used to achieve 100Ω at the tee. However, in most situations, the smallest amount of cable is desired to eliminate losses due to cable length and any potential transmission line effects. Also, length of the cable is also dictated by the setup of the experiment and only enough cable must be used to accommodate the setup. Therefore, the length of the cable was set constant based on the lengths used in the experiments done here: 43.2cm.

For an air plasma with an electron density of 10^{12} cm^{-3}, the plasma impedance is estimated to be $(25.7-261.4i)\Omega$. The necessary lengths of the lines in the device can be calculated using equations (4.1)-(4.7). This results in a series length of 27.95cm and a shunt length of 6.26 cm. Table 5.1 shows lengths necessary for a range of electron densities. There is a clear trend with decreasing increasing shunt length and decreasing series length with increasing electron density. This holds true until higher electron densities where the ballasting effect begins to fail. At this point the plasma resistance begins to reduce with electron density and is at the limits of where this plasma operates.

Table 5.1: Calculated Lengths for Series and Shunt Legs For Optimum Dual System Impedance Matching

Electron Density(cm^{-3})	Shunt length (cm)	Series Length (cm)
6.00E+11	5.69	28.34
8.00E+11	6.0	28.13
1.00E+12	6.26	27.95
2.00E+12	7.169	27.40
4.00E+12	8.09	26.94
6.00E+12	8.514	26.79
8.00E+12	8.72	26.76
1.00E+13	8.80	26.78
2.00E+13	8.611	27.05
3.00E+13	8.19	27.32

5.2 Frequency Response of Devices

Two identical sources were built by the NCSU machine shop. Once the devices were built, a few tests needed to be run before the devices were actually connected to the generator and tested. In order to check to see if the devices would behave as expected, each device was connected to the Hewlett Packard 8753 network analyzer used in previous experiments. This was to determine if the devices behaved as the previous devices did as well as to see if the predictions made by the circuit model of the device agreed with performance of the devices. Each device was connected independently to the network analyzer and examined via a single port measurement of transmission and reflection of a calibrated RF signal. The main goal was to determine if the resonant frequency for each device was at the expected frequency, and how it changed with different series and shunt lengths. Table 5.2 shows the data from the network analyzer for a range of series and shunt lengths for device #2 and device #1. The devices must be distinguished from one another as there are slight differences in the lengths of different sections of about 0.5 cm which can play a role in many of the measurements done here. Three different points were chosen as each had the resonant frequency close to 162MHz.

Comparing the data in the table, each device has a similar response with only one significant difference. The frequency at which each resonance occurs only differs by about 1MHz and the full width half max (FWHM) measurements were all with about 16% of each other. The one significant difference was between the measurements where the resonance depth goes form -23dB to -6.9dB. This then means there is a significant difference in the 162MHz impedance at the input of the device for this measurement as well. The main factor contributing to this is the sliding ground connection plate. Mechanical tolerances that allow the ground end to slide back in forth also presents a condition where it does not lock in tightly to the device, and can result in the shunt leg being terminated to different impedances. This can be shown to have a significant impact held constant with a

Table 5.2: VNA Data for both Individual Devices

Series (cm)	Shunt (cm)	Resonant freq (MHz)	Resonance Depth (dB)	FWHM (MHz)	R@162 MHz (Ω)	X@162 MHz (Ω)
Device #2						
28.9	4.53	162.168	-4.42	12.1	59.6	-82
26.42	7.11	159.2	-2.5	20.3	15.9	-55.9
31.5	2.03	163.56	-23	4.41	40.1	41
Device #1						
28.9	4.53	161.9	-4.5	13.5	50.1	-74.2
26.42	7.11	159.49	-3.1	23.6	17.3	-67.5
31.5	2.03	162.49	-6.9	4.52	118.4	-49.8

series length of 26.42cm and shunt length of 7.11cm except for the resistance that the shunt leg is terminated to, Z_{ground} from equation (4.5). Two values for Z_{ground} were used: 0.2Ω and 0.9Ω. This shows the significant impact on the depth of the resonance that this value can have as it changes the depth of the resonance in Figure 5.1 from -0.63dB to -2.74dB. This

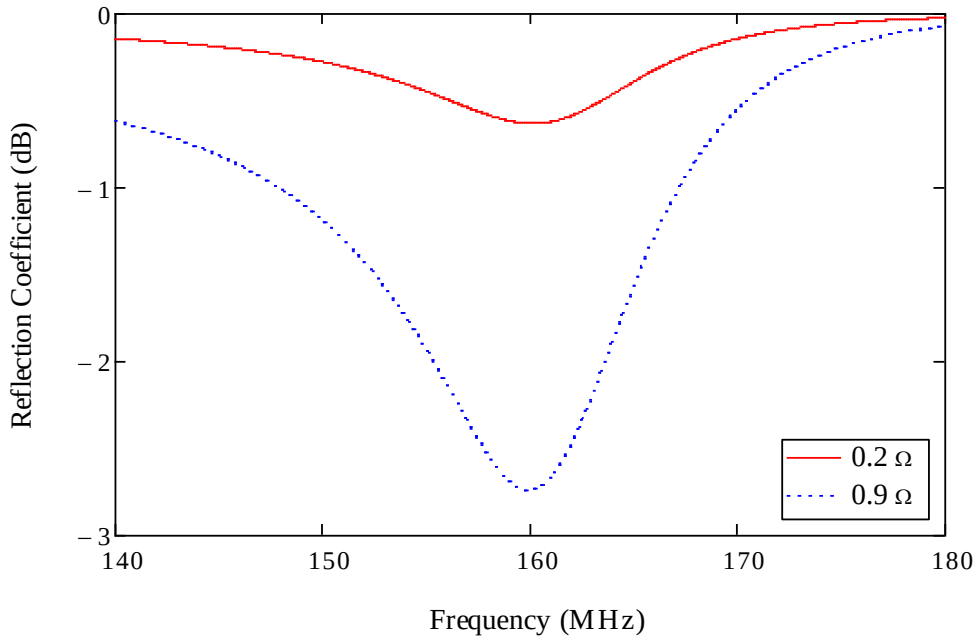

Figure 5.1: Frequency Response of Device with Different Ground Plate Resistances

effect can also be seen when experimentally testing the device. By simply tapping on the device where the ground connection plate is, the depth of the resonances can be observed changing by a significant amount. Therefore, the difference in the two recorded resonance depths for the devices can be explained by a small difference in the resistance at the connection of the inner and outer conductors on the shunt end of the device.

5.2.1 Multiple Device Frequency Response

More interesting is how the devices respond when connected in parallel. Two RG-393/U coaxial cables were cut to lengths of approximately 43cm and 7-16 DIN connectors were soldered onto the ends. Each of these cables were connected to an input of a device and then both connected to a 7-16 DIN tee connector which the connected to the calibrated cable going to the network analyzer. A variety of combinations of the four parameters, series and shunt for device 1 and series and shunt for device 2, were examined. The lengths used in these experiments were derived from the previous experiment that had single device resonant frequencies near 162MHz. The difference with the two sources compared to a single source is the presence of a second resonance. When both sources are set to the same dimensions however, there is only one resonance that can be seen, or at least a very small one that is embedded in the larger resonance. This is expected although there should be a change in the resonance depth. As this depth is directly related to the impedance at the exit of the device, it would have a significant change with respect to the single device. Although the frequency at which this occurs would not be expected to change significantly. As can be seen in Table 5.3, with both devices having series length of 28.91cm and shunt lengths of 4.53cm and 4.4cm for devices 1 and 2 respectively only one major resonance is seen at 165.3MHz. Although there was a very small resonance that could just be seen at 157.4MHz. Figure 5.2

Table 5.3: VNA Data for Dual Sources Compared With Corresponding Model Data

Series #1 (cm)	Shunt #1 (cm)	Series #2 (cm)	Shunt #2 (cm)	Resonant Freq #1 (MHz)	Resonance #1 Depth	Resonant Freq #2 (MHz)	Resonance #2 Depth
31.496	2.032	31.496	2.032	165.19	-12.6		
28.905	4.5212	28.905	4.5212	157.4		165.3	-6.2
28.905	2.032	31.496	2.032	162.55	-3.71	171.7	-17
28.905	4.5212	31.496	2.032	158.8	-11.2	164.5	-10.04
28.905	4.5212	28.905	2.032	160	-17.7	173.03	-7.45
28.905	2.032	28.905	4.5212	159.75	-9.04	172.9	-9.3
31.496	2.032	28.905	4.5212	158.83	-4.8	165.9	-8.6
26.416	4.5212	28.905	4.5212	157.51	-1.94	170.8	-4.76
26.416	7.112	28.905	4.5212	153.1	-6.46	165	-6
26.416	7.112	26.416	7.112	152.1		165.1	-4.14
26.416	7.112	26.416	4.5212	154.31	-26.9	171.9	-9.56
Model Data							
31.496	2.032	31.496	2.032	164.96	-2.0474		
28.905	4.5212	28.905	4.5212	156.6		162.56	-8.178
28.905	2.032	31.496	2.032	160.04	-3.843	171.28	-11.407
28.905	4.5212	31.496	2.032	162.36	-1.37	165.28	-1.53
28.905	4.5212	28.905	2.032	161.6	-10.842	174.56	-3.379
28.905	2.032	28.905	4.5212	163	7.2038	172.92	-7.3308
31.496	2.032	28.905	4.5212	161.24	12	164	-3.5473
26.416	4.5212	28.905	4.5212	161.52	-3.3358	171.76	-8.1005
26.416	7.112	28.905	4.5212	156.88	-2.45733	165.68	-2.3
26.416	7.112	26.416	7.112	154.2		166.64	-3.094
26.416	7.112	26.416	4.5212	158.28	-4.0867	173.72	-9.8235

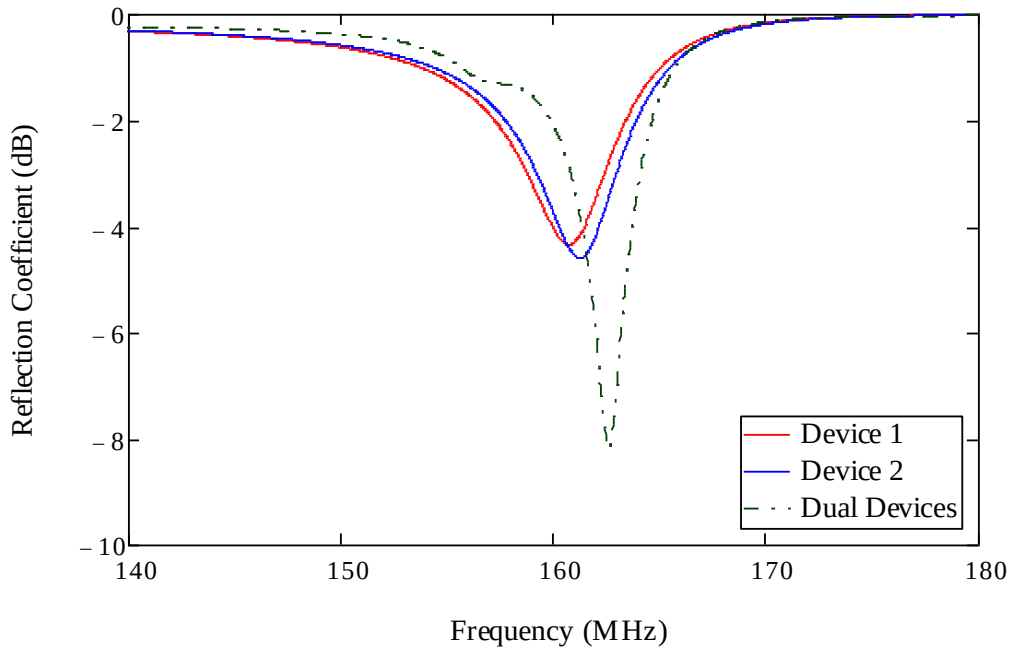

Figure 5.2: Comparing Single Devices and Dual Devices

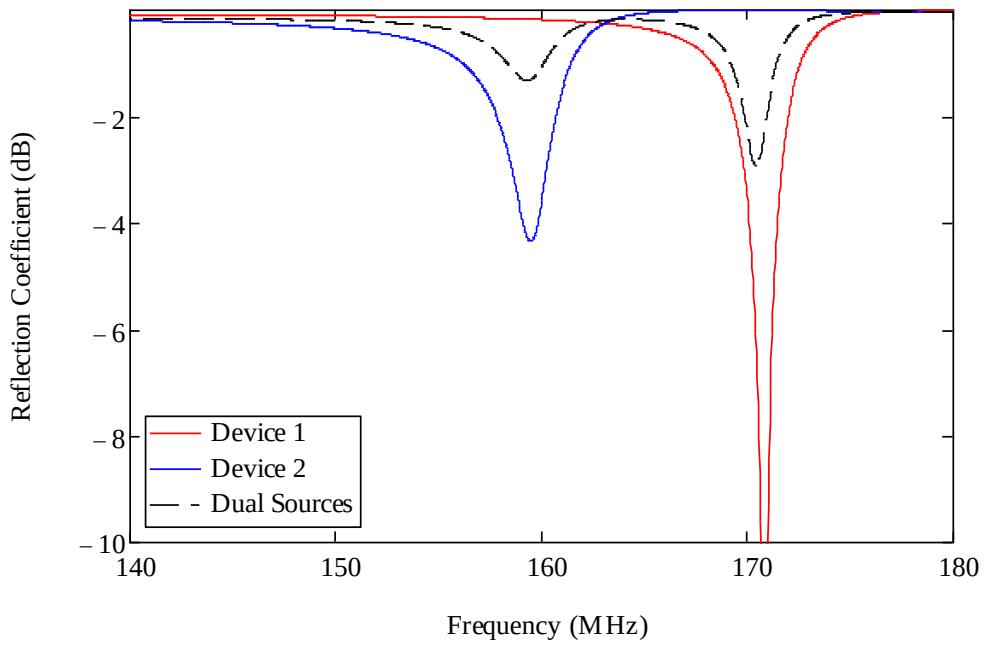

Figure 5.3: Comparing Single and Dual Devices with Different Series Lengths

shows the model data for the same data. Here the slight differences in the devices can be seen, mainly due to errors in measurements, along with the small shift in resonant frequency and the increase in depth of the resonance. However, in the model data the frequency shift is only about 1.5MHz compared to the 3MHz seen in the experimental data. The same small peak can be seen at 156.4MHz, about 1MHz lower than the experimental data. This shift is also similar to the shift seen in the single devices as these resonant frequencies when calculated are found to be at 160.68MHz and 161.24MHz as compared to the 161.9MHz and 162.2MHz frequencies seen experimentally.

Figure 5.3 shows another example of the frequency response of the dual sources. For this plot both devices have the same shunt length of 2.15cm while device 1 has a series length of 28.91cm and device 2 has series length of 31.5cm. This is then compared with the same dimensions for each individual device. While the depths change significantly from the single devices the resonant frequencies do remain close to the initial value of the single device. Overall the model predictions compared with the experimental data are reasonably close. There are some shifts in resonant frequencies of up to 2MHz, but this is in within reason as several small adjustments can create shifts in the frequency. For example a change in the shunt length can cause a shift in the frequency. Figure 5.4 shows how much of an effect this has. The plot shows model data for the same device with the only difference being that one shunt is at 4.15cm while the other is changed by 0.5cm to 4.65cm. This results in a change of resonant frequency of 162.2MHz to 160.1MHz, a 2MHz difference. This could easily account for many of the differences seen in the data as many of the measurements can only be taken with a certain amount of accuracy as well as imperfections in the modeling of the device. There are larger differences in the resonant depths, but these can be explained in a similar fashion as was done previously, but now there are two different ground connections to that could change.

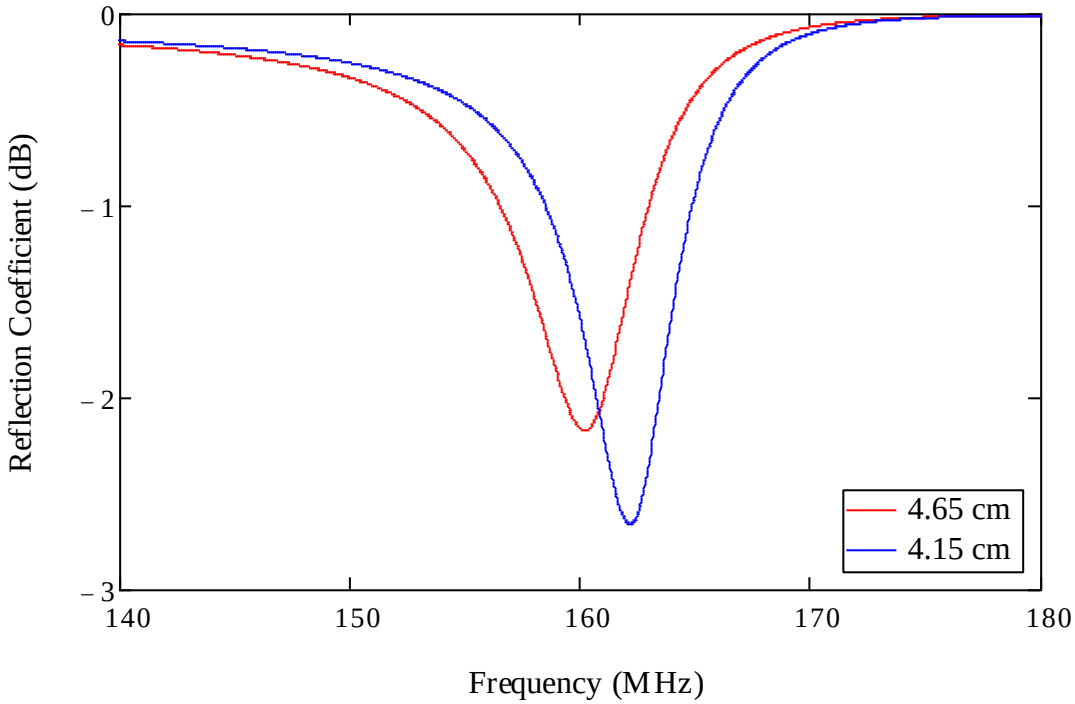

Figure 5.4: Comparison of Frequency Response with Small Change in Shunt Length

5.2.2 Multiple Device Plasma Testing

Previously, experiments had been done in a fume hood or open in the room with an exhaust chute close to the device. At this point, a large enclosure that contained all of the systems necessary for operation, including gases, generators, and the device had been built and was in use. The size constraints of this enclosure required that the dual sources be oriented so that the plasma end of the device was pointed up. This allowed for the devices to fit in the enclosure while also minimizing strain on the power cables used in the setup. Although the preceding material focused on obtaining a good match for the dual system a different approach was taken here to ensure a stable working plasma. Instead of setting the dimensions to calculated values, only one device was connected to the generator and set such that a stable plasma was formed with low reflected power. Then both devices were set to the same dimensions and hooked up simultaneously. Due to the generator's capability to run in delivered power mode, a shift in the impedance caused by the devices operating in parallel

could easily be handled. Once both devices were connected it was very straight forward to get both of the sources running simultaneously. Figure 5.5 is an image of the two sources operating in parallel simultaneously. The plasmas in these devices look similar to the previous plasmas seen with the single device. Figure 5.5 illustrates that both plasmas were operating simultaneously.

Figure 5.5: Image of the Dual Sources in Operation

On the first successful production of the two plasmas, there was a significant amount of reflected power, approximately 300W for the 800W of delivered power. This was remedied by changing the series and shunt lengths of both devices. From the data in the previous section, an ideal configuration for both devices to have lengths as close to each other so that there is only the one resonance found at 162MHz. The final lengths used for this initial test was: Device 1 series = 29.64cm and shunt = 3.8cm, Device 2: series = 29.54cm and shunt = 3.726cm. There is a slight difference in the two as the measurements for length are external from the device and result in slightly different actual lengths needed for calculation. For ease of the experiment the external measurements are the ones set equal

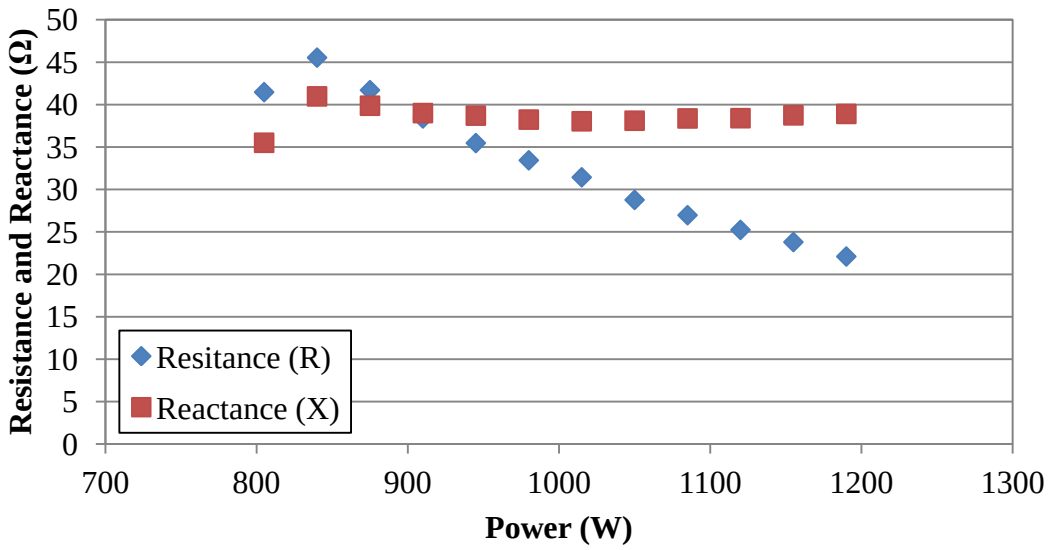

Figure 5.6: Resistance and Reactance of Initial Duel Source Setup

to each other. Figure 5.6 shows the complex impedance seen by the generator. Although at low powers the resistance is close to 50Ω, there is still significant amount of reflected power due to the reactance also being near 50Ω. The trends seen here are very similar to the ones seen with the single device. The reactance tends to change very little while the resistance decreases as the power is increased. Once it was clear that the plasmas could be sustained, the lengths of the devices were change in order to reduce the amount of reflected power in the system. The best match in this situation was obtained when both series were 28.14cm, and shunt1 = 5.3cm and shunt2 = 5.68cm. This resulted in a voltage reflection coefficient of 0.18. Figure 5.7 shows the initial dual setup and the better matched one through a sweep of power. The ▲ show the initial impedances for first time setup with powers ranging from 805W to 1190W in 35W increments. The ■ symbols represent the modified devices with a better match. The powers swept for this data are 875W to 1155W in 70W increments. Power is increasing from the lower right to the upper left in both data sets. The ♦ symbols represent the model data, where electron density is the changing variable in the plot. Electron densities rise from lower right to upper left, similarly to how the power behaves. The dual plasmas due tend to act very similarly to the single source which is desirable. An

interesting observation made was that the brightness of these plasmas could be changed such that one was much brighter than the other one. This was done by changing the shunt lengths on one of the devices, and could be done during operation of the plasmas. The length could be changed a centimeter or two before the source that was dimming would eventually go out.

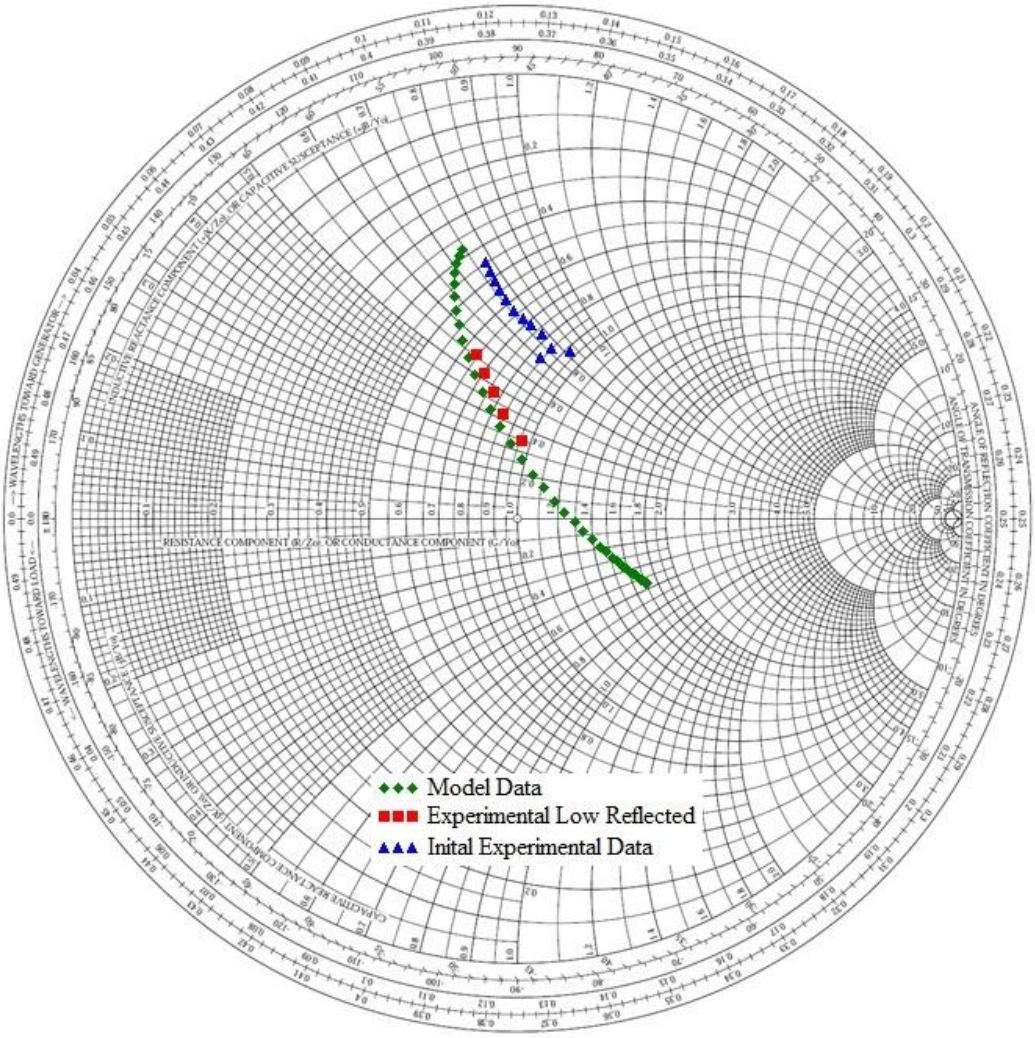

Figure 5.7: Impedances of Dual Sources for Two Different Lengths Compared to Model Data

This fact could be useful in the future for some application as it could provide plasmas with different electron densities that could be operated from the same generator. Potentially some process could need one treatment with a high density plasma while immediately needing some less dense plasma. Further customization could also be achieved with flowing different gases through different devices. However, this would need considerable more effort to achieve to stable plasmas with different gas compositions.

5.3 Electron Density Calculation

Since the model data is able to closely reproduce the experimental data then this can be used to effectively calculate the electron density of the two discharges for this experiment. One major assumption must be made due to the amount of information taken from the system. Both plasmas must be assumed to have the same density to be able to make any calculation of the electron density. This is because there is only one measurement value, impedance at the generator. However, to calculate the density of the plasma the plasma impedance must be known. Since there would be two plasma impedances unknown and only one measurement, there is no way to independently calculate the plasma impedances independently. There would actually be many different possible solutions which would not lead to the appropriate electron density. Thus both plasma impedances (and therefore electron densities) are assumed equal. In order to account for this problem, an impedance measurement or a V-I reading could be used before the tee connector on one of the plasma systems. Then an impedance value on each of the single lines connected to each device could be found leading to two independent density calculations. This comes back to why the experimental data points were chosen. The data for this calculation was chosen because during the experiment it appeared that each plasma had a similar brightness, and was confirmed with simple OES data confirming approximately equal intensities of emission.

Electron Density calculations for this experiment were done the same was as in section 4.3.3. The measured electrical impedance taken by the generator is used and then the plasma impedance is found by calculating the impedance down the line that would produce the measured impedance. The data set in Figure 5.7 that is closest to the model data was

used in the following calculations. Calculated electron densities are in the same order of magnitude as the densities calculated for the single tube device with approximately half as much input power. The overall increase in electron density with increasing power trends in the appropriate direction. Also, the ballasting effect discussed in section 3.3 can also be seen as the overall plasma impedance, Z_p, also increases with increasing electron density. This gives assurance that this model for the dual system is an effective method for calculating densities and predicting electrical behavior of the device.

Table 5.4: Impedances and Electron Densities Calculated with Dual Sources

Power	Measured Impedance (Ω)		Plasma Impedance (Ω)		Electron Density(cm^{-3})
875	47.4	17.6i	27.6	-263.7i	3.80E+11
945	41.8	21.2i	35.3	-264.8i	5.60E+11
1015	38.1	24.0i	41.1	-266.8i	7.30E+11
1085	34.8	26.2i	49.3	-269.0i	9.60E+11
1155	31.8	28.0i	57.2	-271.5i	1.20E+12

5.4 Comparison to Data from Single Device

In order to confirm that the devices are acting as they should it is necessary to look at some of the original data for the single source. Comparing electron densities as a function of power helps to get an insight into if the sources are behaving independently as the individual sources do. Figure 5.8 shows a plot of the electron density as a function of input power for both the dual system and the original single source. In order to get similar power levels for both systems, it was assumed that the same amount of power went to each device, just as it was assumed that the electrond densities would be equal. Therefore the power used for this plot is simply the input powers from Table 5.4 and divide each one in half. The result is that the electron densities are slightly smaller for the dual system than the single source. The dual system's electron densities tend to bearound 30% lower than the single device. This could be caused by some of the extra losses involved due to the extra cable lengths although this

should have little effect as there should only be about a 1% drop in power over the lengths used in the dual system. Also, this could be an effect of the assumption used to calculate the densities. If the densities were not as similar as was assumed, a significant change in this "average" density might occur. Also it appears the gas temperature is higher for the dual system experiment as compared with the single source data. This would result in more energy going into heating the gas particles instead of being used for electron production through ionization. The increase in temperature is discussed in the following section.

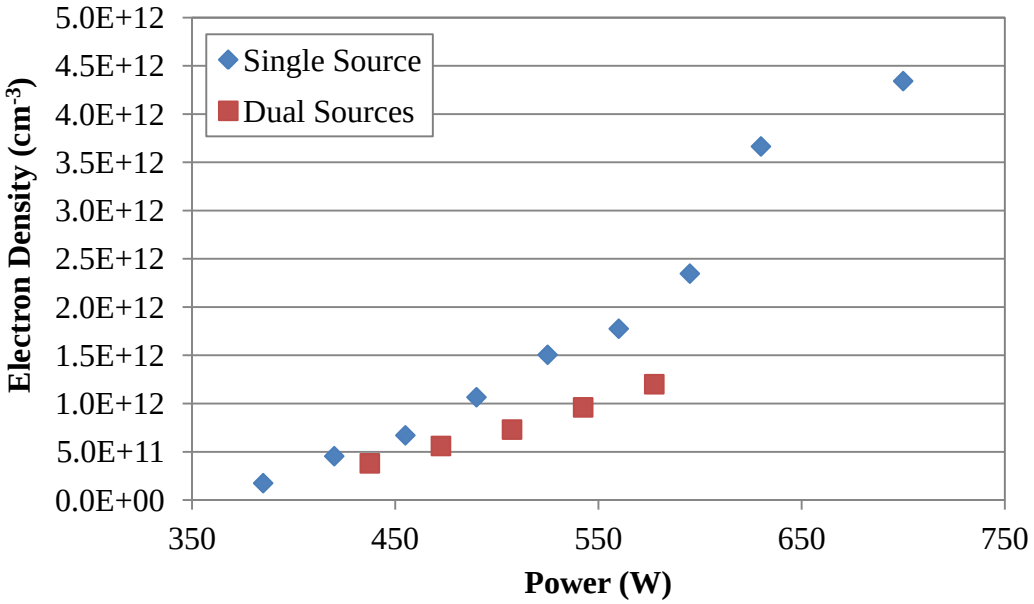

Figure 5.8: Comparison of Electron Densities for Single and Dual Sources

5.5 OES

Spectroscopy was also used to characterize the dual system and compare it to the single source. This technique was used to determine molecular and atomic species present in the two plasmas as well as OH radical rotational temperature measurements. Air is the only gas that was used for any of the experiments. Figure 5.9 shows the spectra recorded for each device. These spectra were taken for the same set points as the electron density calculation

data points. This illustrates that the electron densities are close they are definitely not identical. However, as the peaks of the molecular emissions are still very close it is within reason to make the assumption. There is a large broadband emission starting around 450 nm in these spectra. While this is present in the spectra presented for the single device, Figure 4.2, it is not nearly as large. This type of emission indicates an increase in the gas temperature, and this is observed by the increase in heating of the actual device. When this emission is seen, the outer tube of the device can be felt to be significantly warmer than when it is not present. However, this is not something that happens exclusively with the dual system. This has also been seen with a single device. It is not known what the cause of this change in the plasma is.

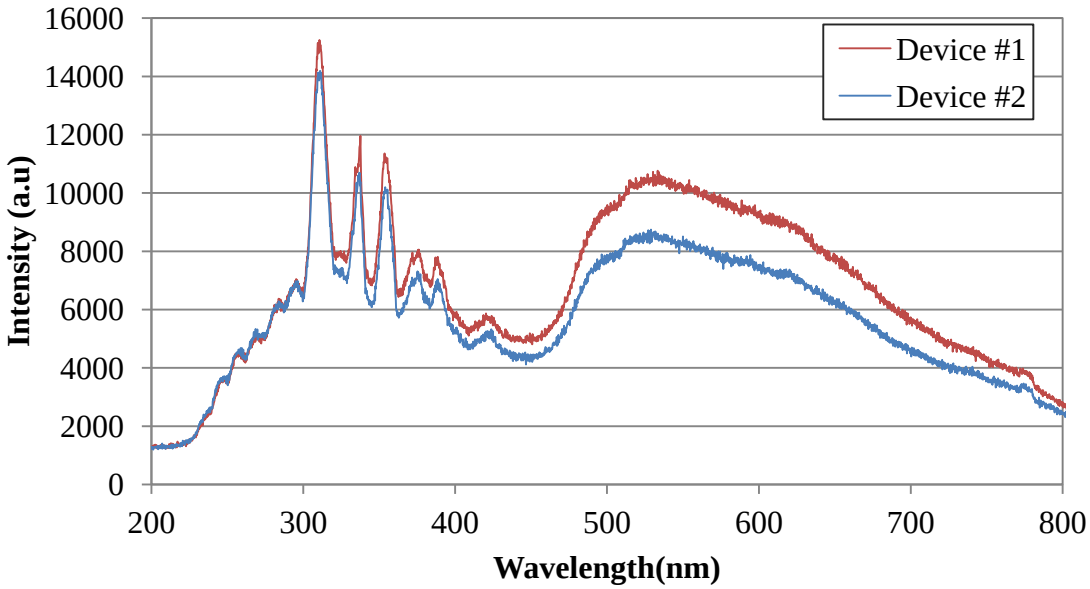

Figure 5.9: Simultaneous Spectra for Each Device with Air as the Feed gas

5.5.1 OH Temperature Measurement

OH rotational temperature measurements were also made for the dual plasma system. The same technique was used as before with the PIXIS 256 CCD camera being used along with the Acton 2500 1.5m spectrometer being used to take the data. The spectrometer was centered between the 309nm and 306nm peaks and the ratio of these peaks can be used to determine the rotational temperature. Figure 5.10 and Figure 5.11 are the spectra for a range of powers at the relevant wavelengths for the temperature measurements. There is a slight shift in the wavelengths for which these emissions occur as the R-branch peak occurs closer to 307nm than to 306nm. This is simply due to some calibration errors but these are the

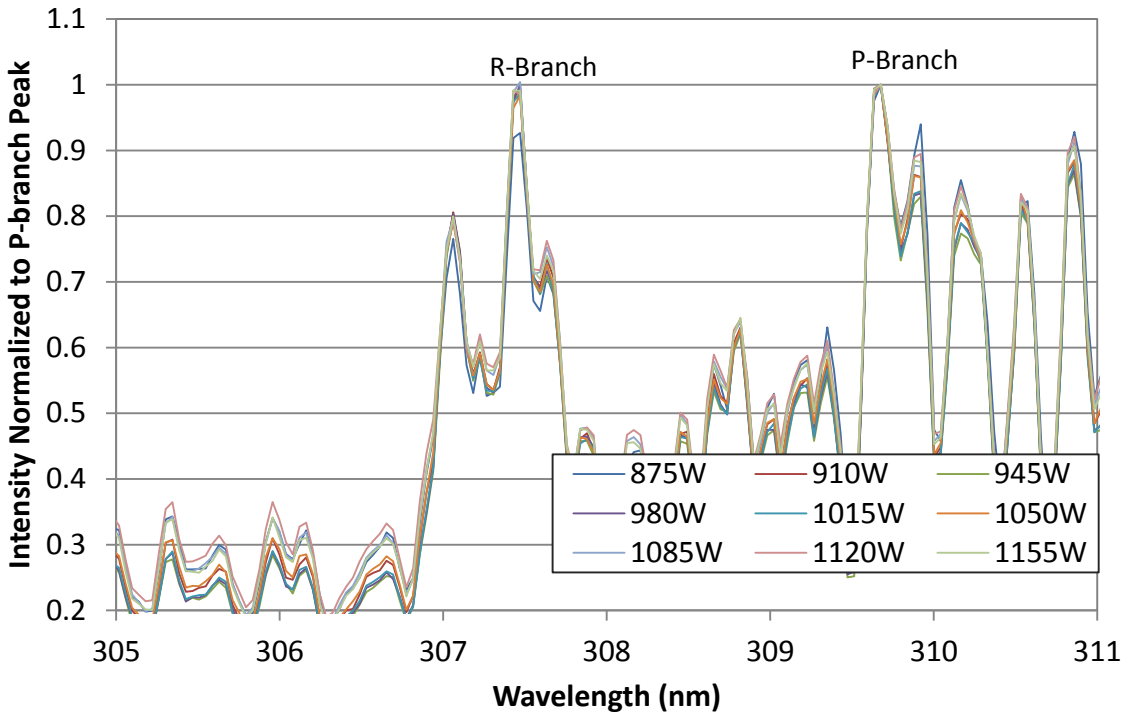

Figure 5.10: OH Temperature Measurements for Device #1

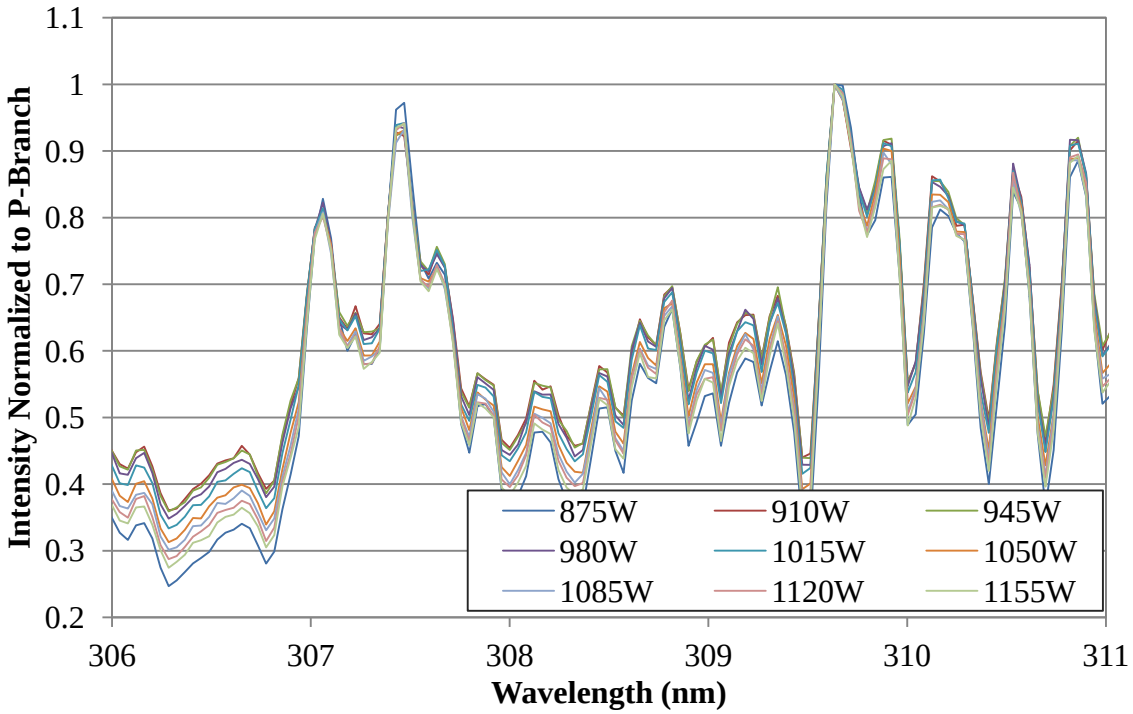

Figure 5.11: OH Temperature Measurements for Device #2

Table 5.5: P/R branch Ratio for Each Device

Power (W)	P/R ratio #1	P/R ratio #2
875	1.07907	1.03282
910	1.005893	1.106045
945	1.010295	1.102003
980	0.999789	1.088901
1015	1.015592	1.07946
1050	1.016402	1.093733
1085	0.995897	1.090615
1120	1.008805	1.075492
1155	1.00865	1.075514

correct peaks for the measurements. These figures are normalized so that the P-branch emission is set to 1. This is done since the ratio of the P-branch to the R-branch, P/R, is the

concern. By doing this the trends in the rotational temperature can be qualitatively observed as the gas temperature decreases as the R-branch peak decreases. However, in this experiment it appears that there is very little change in the ratio of the peaks. This is in part due to the already high rotational temperature of the OH molecules. Using this technique, with the temperatures measured, a very small change in the ratio of the peaks can result in significant changes in rotational temperature as seen in Figure 4.11. Table 5.5 shows the ratios found for these devices. These are very small ratios close to 1 for all of them. This results in temperatures of at least 5000K. After this point it is difficult to extract more exact data due to the resolution of the process. This brings up the main issue with this technique, self-absorption of the p-branch. At these already high temperatures a small amount of absorption can have a significant increase in the measured temperature. Due to the size of the plasmas as well as the humid air supply, there is bound to be enough self-absorption to inflate these measurements.

5.6 Conclusions

The design and implementation of the dual source system was relatively straight forward. Using the simple model developed for the single device, the behavior of the impedance for the devices was sufficiently predicted. Furthermore, power distribution between the two sources was straight forward and could easily be changed by changing the lengths of the series and shunt elements. This indicates that expanding this process to an arbitrary number of devices is possible, limited of course by the amount of power that the generator can provide. With multiple devices running simultaneously, any applications that the device is used for could be scaled without a huge increase in cost as the cost of the device is very low compared to the price of a generator. There were also no significant changes in the behavior of the plasma. While the electron densities measured were lower, new measurements would be necessary with an additional impedance measurement are necessary in order to be able to characterize each of the devices independently.

Chapter 6: Applications

In Chapter 5 the issue of scaling the device for an application was addressed by discussing the operation of multiple sources in parallel. Operation of two sources was demonstrated. Implementation of more devices is straight forward and the same approach can be followed. This chapter discusses in detail some of the applications that have been investigated for the device where scaling up of the process could be necessary.

Due to the uniqueness of the device there are a large variety of potential applications that it could be used for. Its large area in comparison to other atmospheric devices allow it to potentially be used for current processes that must be done at vacuum, allowing a significant reduction in cost since the vacuum chambers are expensive. The ability of the device to run a variety of gases also opens up a number of potential applications, as we are not limited to simple noble gases that have limited pathways for chemical reactions with a substrate. The two main types of applications that are looked at are surface treatment and water treatment. Surface treatment refers to the application of either the plasma or the reactive species directly on to the surface of some substrate. Water treatment deals with the molecules that we can either add to water, such as nitrates for fertilizers, or the removal of unwanted chemicals such as 1,4 dioxane or perfluorooctane sulfonates (PFOS). In order for this to be effective as an industrial application, the ability to perform these processes on a large scale must also be considered. Scaling of the source is necessary by either increasing the size of the plasma or by running the devices in parallel. Here the design of running the sources in parallel is discussed.

6.1 Water Treatment

While vacuum chambers are costly which creates a desire to move away from these systems for plasma devices if possible, there are certain situations where the presence of a vacuum makes it impossible to apply the plasmas to a substrate. One interesting instance of this is water. Water does not stay in its liquid state at the pressure and temperatures of most vacuum plasmas. This makes it very difficult if not impossible to have any sort of plasma

application with any reasonable rate of interaction. Atmospheric plasmas, however, allow for the treatment of water for a variety of different applications. As the molecules are ionized in the plasma, they are able to form interesting and novel chemistries that are difficult to obtain any other situations. Even when these are possible, hazardous materials and chemicals are necessary to obtain the types of chemistry needed for a particular application. There are two main types of water applications that are discussed: addition of molecules to the water and the removal or degradation of unwanted compounds already present in the water.

In order to treat the water, the device was oriented so that the plasma is pointed down. This then allows the plasma to be able to be placed directly on the surface of the water. Figure 6.1 is an image of the setup for the water treatment experiments. The plasma can be seen directly on the surface of the water. The mesh screen around the device is used to screen out any of the RF that comes out of the device. This is the easiest and most direct method for treating water, although it leaves much room open for improvement on the efficiency of any process as there is very little contact between the water and the surface of the water. It is no expected for the plasma to be able to penetrate the water so the only area where the molecules can react is directly at the water surface when in direct contact with the plasma.

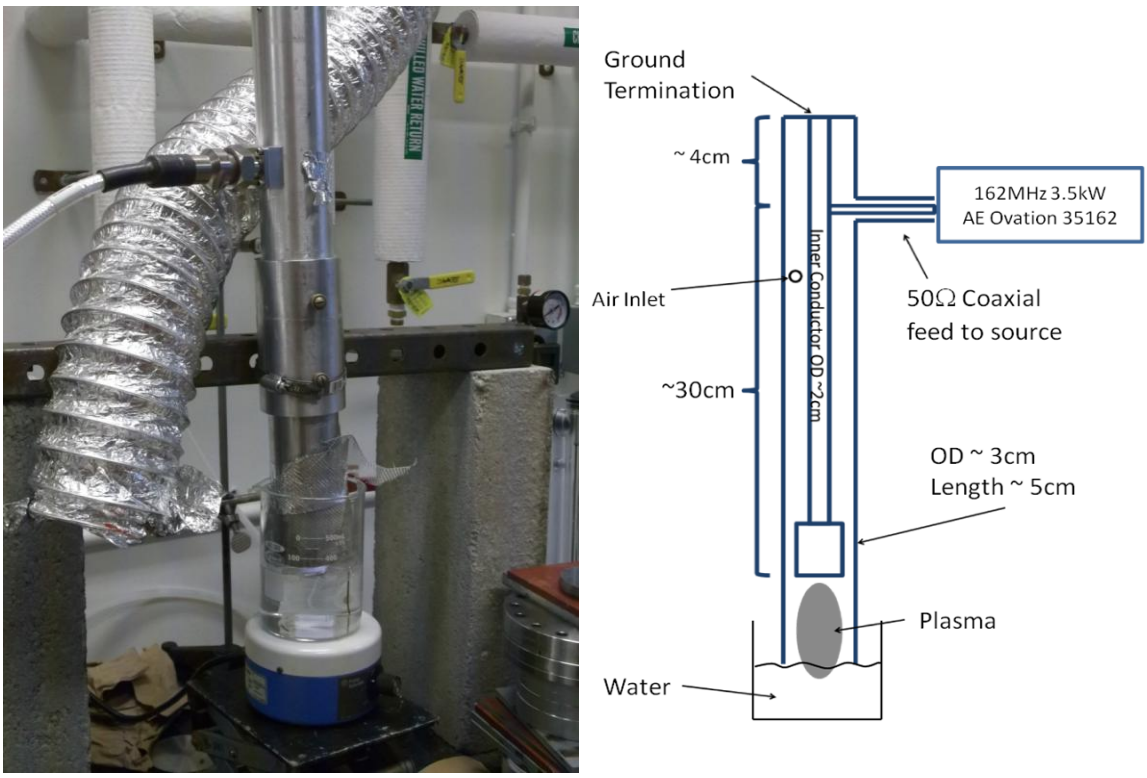

Figure 6.1: Plasma Water Treatment.

6.1.1 Plasma-Water Characteristics

There are some very different characteristics of the plasma when in contact with the water. An obvious physical difference is the change in size and shape of the plasma. As the water is placed close to the surface of the electrode and the plasma stops at the surface of the water, the total length of the plasma is much smaller. Also, the radius of the plasma tends to decrease during treatment and is just a small cylinder shape. This is most likely due to all of the excess oxygen that exists from the production of OH that reduces the number of electrons because of oxygen's electronegativity. Normally, the plasma has a center that is brighter and smaller than the rest of the plasma. The removal of electrons from the plasma by the oxygen prevents the plasma from expanding out away from the center more dense region of the plasma.

Once again OES is used to examine the contents of plasma-water discharge. Figure 6.2 shows a representative spectrum for the treatment of the water surface. This was taken with an input power of 500W with an air flow rate of 4 scfm. The discharge spectrum is almost completely dominated by the OH emission lines near 300nm. Any reactive nitrogen species cannot be seen in this spectrum as the O atoms react with the free hydrogen atoms from the water. Therefore, there are no NO_x species that can be seen in this emission. There is also a small peak around 585nm that was not seen previously. As the experiment was done

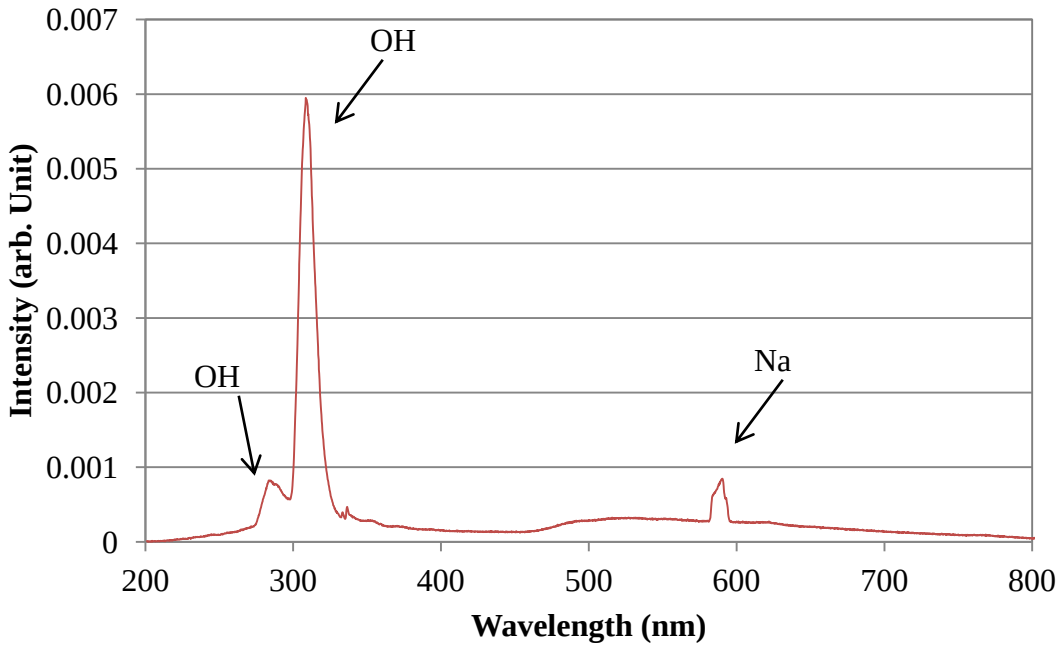

Figure 6.2: OES Data for Plasma Treatment of Water Surface at 500W 4scfm

Using tap water there are other contaminants in the water sample that would cause this new emission. This emission corresponds with the atomic emission lines of sodium at 588.9nm and 589.5nm. The city water would contain some sodium in the water and this would be a reasonable result of the sodium interacting with the plasma.

6.1.2 Nitrogen

One particular use for this is for the uptake of nitrogen into a volume of water to be used as fertilizer for plants. As air is primarily made up of oxygen and nitrogen the air plasma discharge is made of a large amount of NO_x compounds, which can be seen from spectroscopic data in section 4.1.2. When the plasma interacts with water, these compounds are absorbed in the water as either nitrate, NO_3, or nitrite, NO_2. Oxygen for NOx production is further provided through direct plasma interaction with water species. Dissociation of surface water species via electron impact or UV dissociation are possible in the liquid phase as well as the gas phase, and OES results indicate significant production of species from water precursors when spectra is compared with and without water interaction with the active plasma region. Nitrate is one of the primary constituents in fertilizers that deliver nitrogen to plants. With current configurations, this plasma source has been able to impart nitrate levels of up to 300pm to water. While this highest number was achieved with small water volume and large treatment time, there is much room for the improvement in the absorbed nitrogen rates in water. When the nitrate or nitrite is absorbed into water it bonds with the water molecules to make nitric acid. This is a noticeable effect as the pH consistently drops with increased plasma treatment time. This effect is more apparent experiments using distilled water because of the buffering agents found in tap water that resists a small drop in pH. The pH lowers to a minimum pH of 2.7 after some time period while still absorbing nitrogen into the system. While other plasma systems running noble gases have seen a decrease in pH after water treatment, one major difference is that the pH for the air plasma system remains low. In other systems the pH returns back to its original after some time has.

This process of incorporating nitrogen species into water leads to the possibility of the device being used as an onsite fertilizer generator. It would allow for small amounts of water to be treated using only compressed air and electricity resulting in fertilizer that could then used almost immediately. The only thing that would need to be done to the water is to add a base to increase the pH to a level that would not harm any plants that were receiving the water. This is easily done by using baking soda. It is cheap and readily available and does not have any negative effects to worry about. This can be done at any point and can

actually be used to modify the amount of nitrate vs. nitrite in the water solution. There are many factors that contribute to the overall production in nitrates and nitrites in a sample of water including delivered power, airflow rate, distance between water surface and plasma, treatment time, sample volume, and when the addition of the baking soda was added.

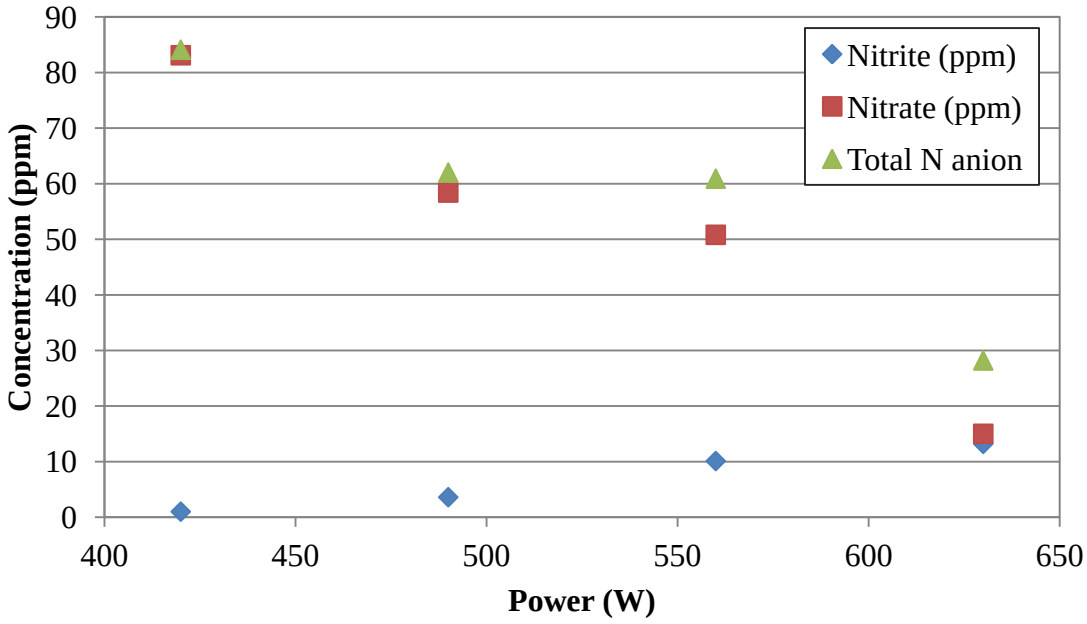

Figure 6.3: Nitrate and Nitrite Production with Input Power

Figure 6.3 shows the nitrate and nitrite levels for a variety of input powers. This experiment was done using tap water, and the total N was found by simply adding the two nitrate and nitrite concentrations together, as there is just one N atom in each of these molecules. The total nitrogen tends to decrease with an increase of the input power. This is counterintuitive as there is a higher electron density with higher powers that should result in more reactive species to form nitrate and nitrite in the treated water. However, nitrite production does increase while the nitrate concentration falls drastically. One possible explanation for this is the increased number of electrons effectively reduce the NO_3 to NO_2

and even more reduced forms such as NO. These measurements only account for NO_2 and NO_3 so the total N production could not be exactly accurate if these electrons are reducing these molecules down to NO. Distilled water was also used for many experiments, and the same data for distilled water is seen in Figure 6.4. The major difference between the distilled and tap water is that there is effectively no nitrite produce in the water. Furthermore, the total N concentration is similar at lower powers, but the nitrate concentration tends to decrease at a slower rate than it does for tap water.

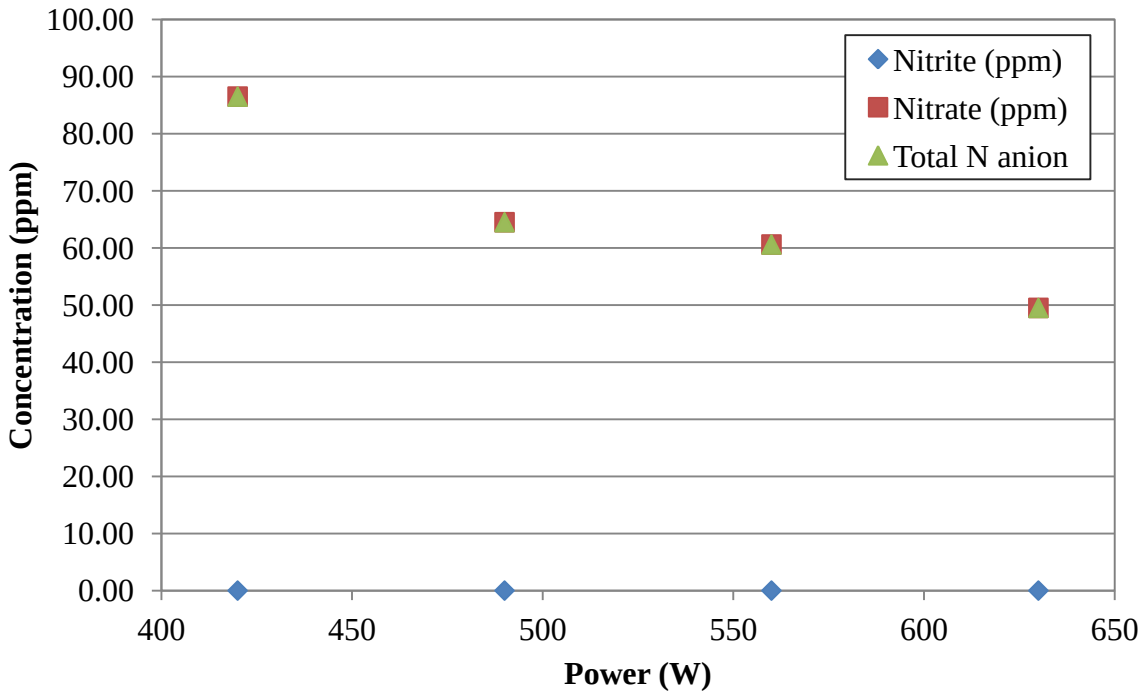

Figure 6.4: Nitrate and Nitrite Production with Input Power for Distilled Water

Another important parameter to consider is the flow rate of the air. There is a significant improvement in the nitrogen concentrations with increasing flow rates. Figure 6.5 shows the results from the air flow experiments. This experiment was done with distilled water with 150mL samples treated for 3 min. By increasing the flow rate by a factor of 1.7,

the total nitrate concentration increased by a factor of 4.8. This large improvement can be easily explained as the increased airflow allows for more interaction between the water and the reactive species. The increase in airflow decreases the time between the generation of the reactive species and the moment of interaction with the water surface. This results in a greater percentage of the species to be able to interact with the water. Also, the increased airflow tends to agitate the water surface creating ripples and other changes to the surface that changes the total amount of surface are exposed to the plasma. While this increase is beneficial, there comes a point where the plasma can no longer be sustained with too high of a flow rate, effectively capping the benefit of this effect. The easiest way to sustain higher flows is to increase the power, but this results in a decrease in the nitrate concentration absorbed in the water, indicating some region where the optimum amount of nitrogen is absorbed in the water. Also, the setup for these experiments also limits the maximum airflow as the water begins to splash up into the device causing the plasma to extinguish.

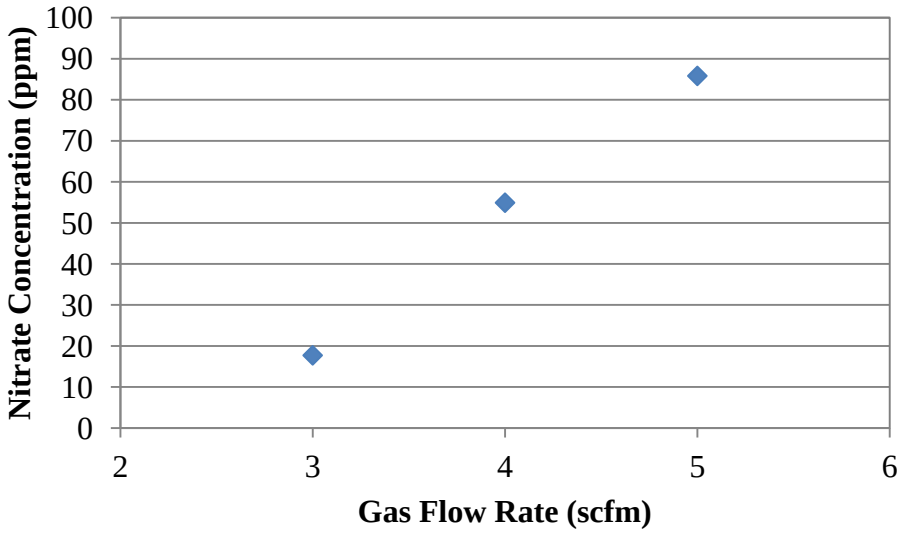

Figure 6.5: Nitrate Concentration with Air Flow Rate

Once it was clear that nitrogen could be absorbed in the water at a reproducible rate, the next goal was to try and optimize the process to allow for more efficient nitrogen production in the water. While conducting these experiments, the most noticeable problem with the system would seem to be the small amount of plasma and water interaction. As the only point where the two meet is at the surface of the water, and as mentioned before the radius of the plasma decreased during treatment, there is a not much surface area of the water in contact with the plasma. If the surface area of the water in contact with the plasma could increase then there could be an increase in the amount of nitrogen added to the water. To try and improve this interaction, it would be best to break the water up into small droplets that are inside the plasma drastically increasing the surface area of the water. To do this, an atomizing nozzle was installed inside the electrode with the exit at the surface of the electrode. As water would be fed through the center of the inner conductor, this could also help with cooling both the electrode and the inner conductor.

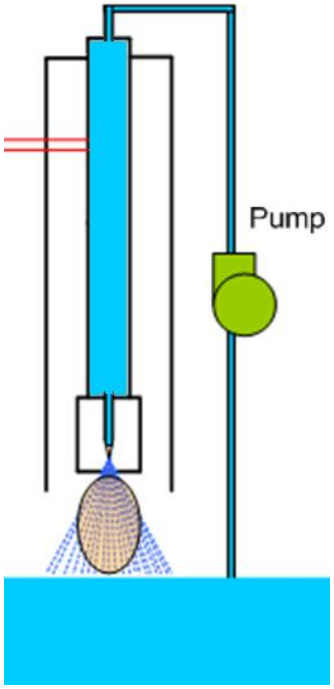

Figure 6.6: Schematic of Electrode Nozzle Design

Figure 6.6 shows the cross section of this design of the system. Another benefit to this system would be that water would be sprayed through the plasma into a reservoir where it could be recirculated through the plasma to obtain the desired level of nitrogen. This system was built, and was able to sustain a plasma while the nozzle was spraying. However, the water coming out of the nozzle seemed to act as a faraday cage. The thick wall of water droplets would screen out any of the RF fields in the device and prevent the plasma from being produced inside the conical spray. Instead, the plasma would form on the outside of the cone and then move around it as the cyclonic airflow in the device pushed it in a circle. There were some experiments performed, but as expected when observing the behavior, the nitrogen concentrations absorbed in the water were small and less than the previous method. Thus, any efforts with design were dropped and moved to other potential system improvements.

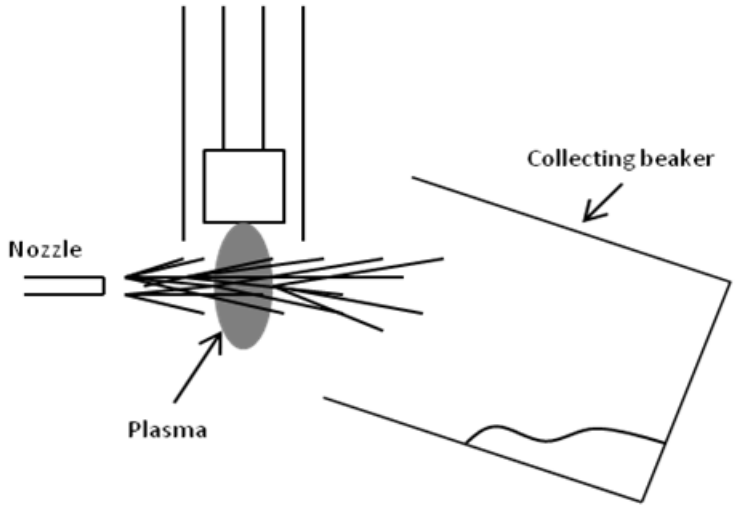

Figure 6.7: Setup for Spraying Water through the Plasma

The next effort to improve efficiency was to allow the plasma to form in atmosphere and then spray the water through the plasma. This was done by configuring the device so that the majority of the plasma extended out of the device, and spraying the water directly

into and through the plasma. Spraying was done with a standard garden sprayer that worked by pumping air into the container, that would force the water through a nozzle. Figure 6.7 shows the setup for how the experiments were conducted. The water is sprayed through the plasma into a beaker on the other side of the plasma. This water could then be put back into the sprayer to allow for multiple passes through the plasma.

A set of experiments to characterize the production of nitrite and nitrate were performed for both tap and distilled water for the following variable: Input power, air flow rate, number of passes through plasma, and the type stream. The type of stream variable is somewhat subjective, but the nozzle can change the shape of the stream coming out of it. There were effectively three types of water flow exiting the nozzle. When fully tightened the water was a fine mist sprayed in a wide cone, referred to here as stream 1. A fully open nozzle was almost a solid stream with some small droplets breaking apart in the stream, referred to here as stream 3. The last setting was in between the two and was a mixture of the two types of streams, stream 2. The following plots contain nitrate, nitrite and total N concentrations for tap water, and total N concentration for distilled water. With distilled water, no nitrites are measured so the total N and nitrate concentrations are the same.

Figure 6.8 shows the power sweep for both types of water. This was done with stream 2, 3scfm airflow, and 1 pass through the plasma. Initially, it seems that these concentrations are extremely low, but these experiments only take a couple of seconds to run 100mL of water as compared to the 3-5 minute exposure times for the batch method of treatment. Comparison of the two methods efficiencies are shown . Distilled water has the highest total nitrogen concentration at 630 W while the tap water has its maximum at 700W. Once again nitrite is produced in greater quantities than nitrate in tap water just as before. Figure 6.9 shows the effects of the type of stream on nitrogen concentration in the water for samples at 630W and 3scfm. For tap water, the highest concentration was with the misting spray and decreased as it became more of a full stream. This was only due to the decrease in nitrate as the nitrite concentration stayed about the same for all flow types.

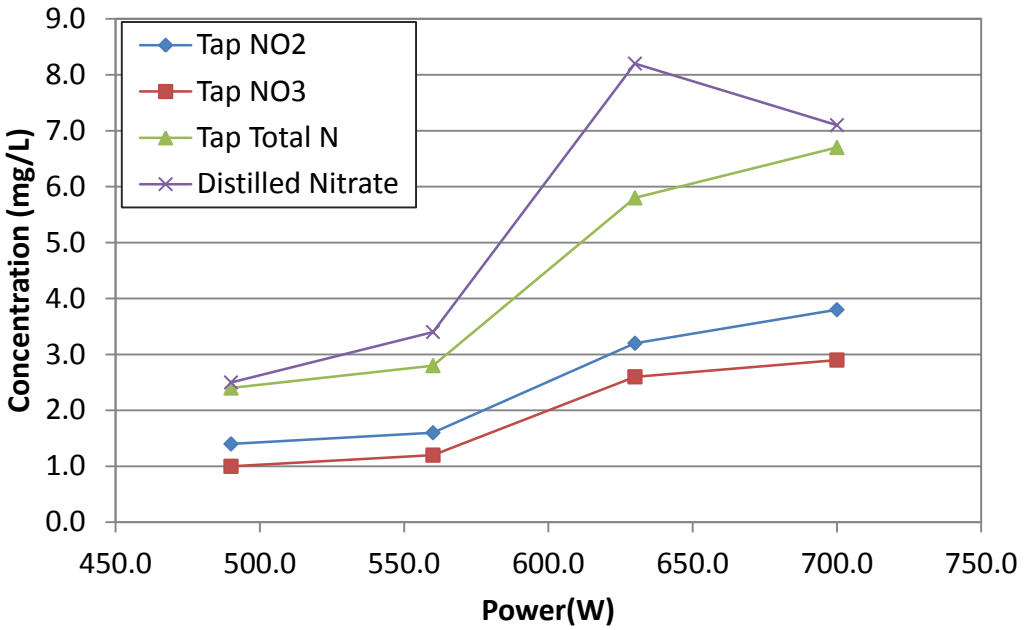

Figure 6.8: Power Sweep of Nitrogen Concentration for Tap and Distilled Water at 3 scfm and Stream 2

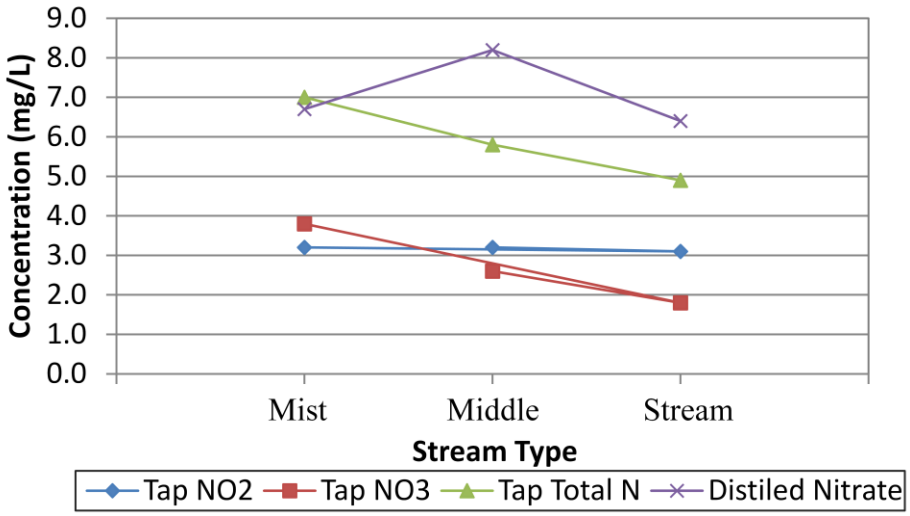

Figure 6.9: How Water Stream Effect Nitrogen Concentration

Figure 6.10 shows the concentration as a function of the number of times the water was sprayed through the plasma. As expected there is basically a linear increase in the amount of nitrogen in the water. This is completely true of the distilled water, but there is one anomaly in the tap water data. On the fourth pass through the concentration for both the nitrate and nitrite decreases. No physical explanation is known for why this would happen for this particular pass through the plasma. Therefore it is most likely due to some error when spraying the water. The spraying was done by hand so there were some times where the

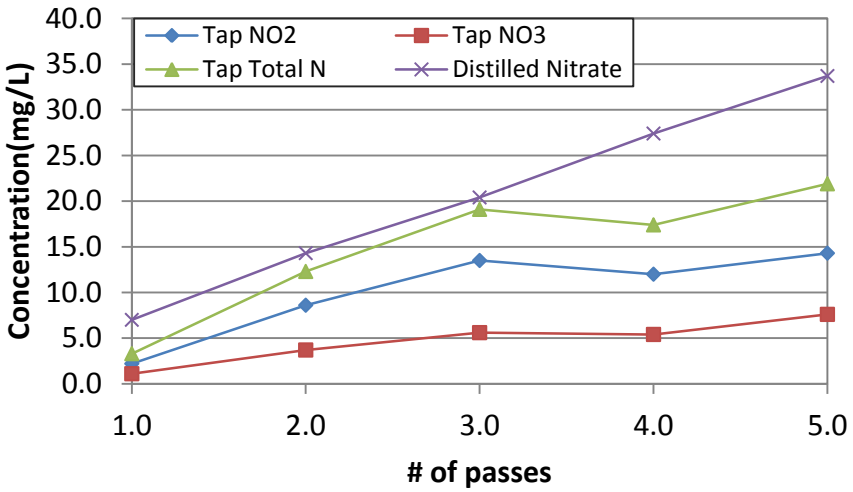

Figure 6.10: Effects of Number of Passes through Plasma on Nitrogen Concentration

spray was more consistent than others so this could have been one of the times where the plasma did not interact much with the spray. This does not quite explain why it would actually drop instead of just increasing by less though. The other experimental error that could cause this is if the previous water was not removed from the sprayer very well. There could also have be some clean water that was in the collection beaker as well that would dilute the nitrogen concentration. It is probably a combination of these errors that led to this one offset data point.

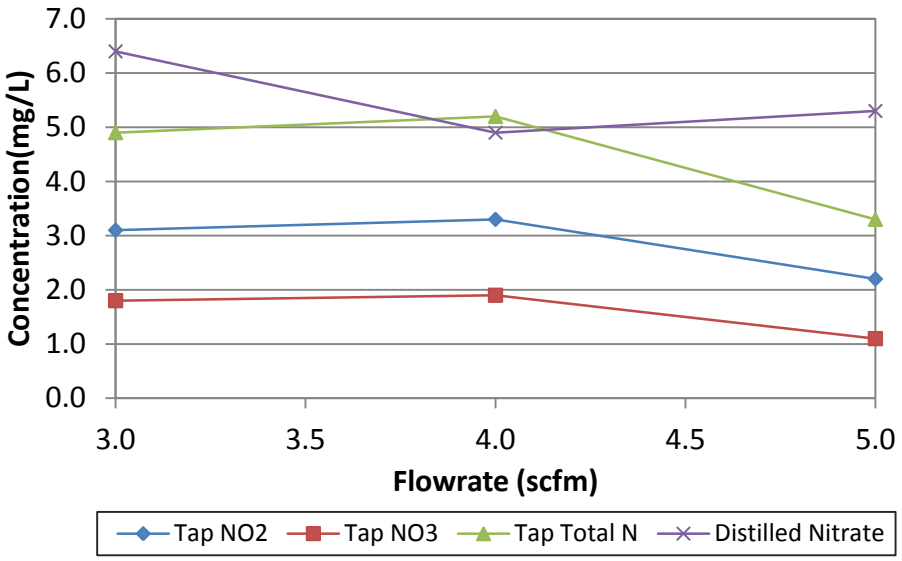

Figure 6.11: Effect of Flow Rate on Nitrogen Concentration

Figure 6.11 is the plot of concentration vs. air flow rate. From this it seems that flow rate does not have a huge impact on the concentrations. Overall lower flows around 3-4 scfm gave the highest concentrations. This is mostly due to how the air flow effects the plasma movement. For high air flows the plasma moves around more since it extending out of the device and does not have the outer tube to maintain the air inside the cylinder. This makes it difficult when spraying water to make sure the water is always in contact with the plasma, which in turn would reduce the concentration of the nitrogen absorbed into the water.

Overall, this process improved the efficiency of the absorption of the nitrogen into the water. To compare the efficiencies, the amount of energy used per kg of nitrogen in the water is calculated for each method. This is a simple calculation given by the following

$$\frac{Pow \cdot t}{conc \cdot V \cdot \left(\frac{14}{62}\right)} = 1.092 \times 10^4 \frac{kWh}{kg} \tag{6.1}$$

Where *Pow* is the input power of the device, t is the treatment time, *conc* is the concentration of the nitrate, *V* is the volume of the treated water and the last part of the denominator converts mass of nitrate to mass of nitrogen. A slightly different method is used to calculate

this quantity for the spray method because the experiments were not timed when they took place. The time it took to fill a certain volume was measured for each of the three types of water streams, allowing for the calculation of how much water is treated per unit time. The equation for energy use per kg nitrogen produced is

$$\frac{Pow}{conc \cdot R_{flow} \frac{14}{62}} = \frac{630W}{7\frac{mg}{L}16.67\frac{mL}{s}\frac{14}{62}} = 6.643\times10^{3}\frac{kW \cdot hr}{kg} \qquad (6.2)$$

where R_{flow} is the flow rate of the sprayer. This data was taken using the full stream sprayer so that is the value seen above. While both of these numbers are very large and impractical for any large scale process there were improvements made with the spray. A drop in the energy used per kg of nitrogen produced in water of about 0.6 was observed between the samples. This is almost a factor of two drop and without any extensive amount of optimization being done for this particular method. It does appear that increasing the surface area that comes into the contact is an integral part in increasing the amount of nitrogen deposited in the water. However, there are many other physical and practical complications that arise in the implementation of these ideas.

Table 6.1: Flow Rate for Each Type of Stream Type from Sprayer

Stream Type	Volume (mL)	Time(s)	Flow Rate(mL/s)
1 (mist)	350	53	6.60
2 (mid)	500	33	15.15
3 (full stream)	500	30	16.67

6.1.3 Fertigation

The first attempt to use this nitrate production was to create a water based fertilizer. As nitrate is the most important component of fertilizer, maximization of nitrate was the main concern. From the previous data this is clear that distilled water would be used as it

only allows the formation of nitrate without any nitrite being produced. However, one other factor needed to be addressed. The pH of the treated plasma water would drop to 2.8. This is a problem as this low of a pH could counteract any positive growth improvement caused by the nitrate in the water. To fix this baking soda is added to the treated water. This needed to be examined as adding in the baking soda at different times could result in different levels of nitrate and nitrite concentrations.

Table 6.2 lists the effects of adding 100mg baking soda to the 200mL of water. This addition was done both before plasma treatment as well as after for both tap and distilled water. For the tap water samples the presence of baking soda increased the overall nitrogen concentration while there was a difference between the nitrate and nitrite concentrations depending on when the baking soda was added. When it was added before treatment, the total nitrogen increased drastically, but this was mainly due to an increase in the nitrogen as without baking soda there was little nitrite produced but with it the concentration increased to 111.8 mg/L. When it was added to the sample after treatment there was little change in the nitrate concentration with an increase in the nitrite concentration. The distilled water behaved similarly as the tap water, with an overall increase in nitrogen production with the addition of baking soda and a higher level of nitrite when it was added before treatment.

Table 6.2: Effects of the Addition of Baking Soda at Different Times

Nitrite (mg/L)	Nitrate (mg/L)	pH	Description
1.9	67.6	3.18	Tap, no NaHCO3 addition
111.8	49.3	7.99	Tap, 96 mg NaHCO3 added pre-exposure
28.4	60.8	7.68	Tap, 104 mg NaHCO3 add post-exposure
0.2	49.3	2.88	Distilled, no NaHCO3 addition
39.3	16.9	8.02	Distilled, 96 mg NaHCO3 added pre-exposure
10.8	85.1	7.55	Distilled, 112 mg NaHCO3 added post-exposure

To maximize just nitrate production, the baking soda needs to be added after exposure, as this helps reduce the amount of nitrite in the solution. In order to minimize the nitrite production another experiment was done to see if waiting some amount of time before the addition of baking soda would be beneficial. For this experiment 150mL sample of distilled water was treated with the following parameters: 420W input power, 5 scfm flow rate, and a 5 minute treatment time. Then the original volume was separated into 20 mL samples where 20mg of baking soda was added to it at various time after the treatment was completed. Figure 6.12 shows the results from this experiment. Baking soda was added to the solution at 5 different times after plasma treatment was completed: immediately, 1 min, 10min, 56 min, and 870min. The nitrate and total N concentration is on the left vertical axis while the nitrite is on the right axis. Nitrite concentrations are significantly lower than nitrate concentrations and decrease with an increase in the time between treatment and addition. Both the nitrate and total N concentrations increase with the delay time. This indicates that in order to maximize both nitrate and nitrogen concentrations, waiting as long as possible before the addition of baking soda. Note that the x-axis is on a logarithmic scale so the decay in the nitrite levels is actually logarithmic, indicating that it takes much longer to actually reduce the nitrite concentration more than was presented here.

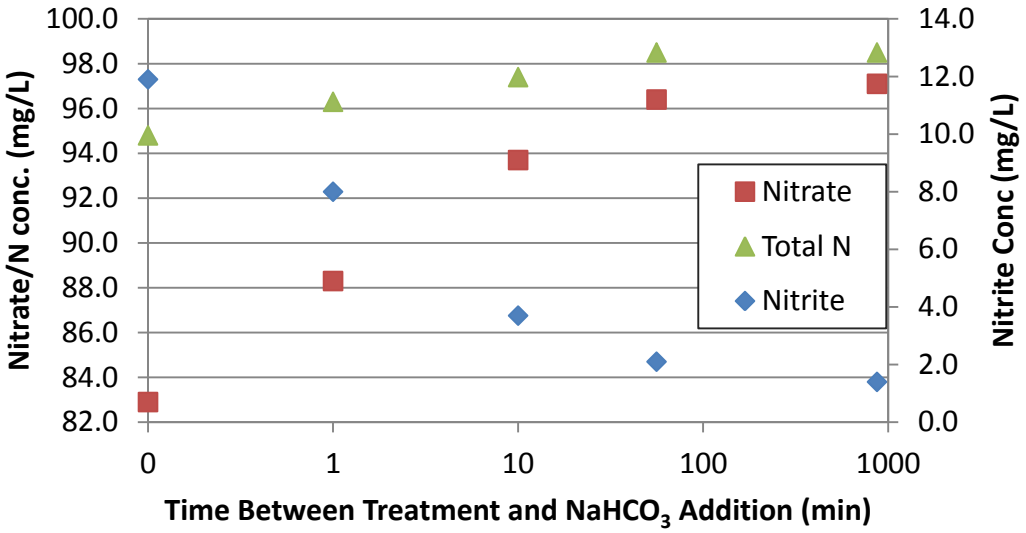

Figure 6.12: Effect of Delaying the Addition of Baking Soda to Treated Water

In order to produce this fertilizer, an 8 cup sample of distilled water was exposed to the plasma for a total of 80 minutes. This would bring the water's pH to 2.8 and the water would then be stored in a dark container. Then after waiting two days, 10mg per 150mL of baking soda was added to adjust the pH of the water to a level that would not be harmful to the plants, just above 6. This delay was chosen from the data presented in Figure 6.12 to reduce the nitrite concentrations while maximizing total nitrogen and nitrate concentrations. This produced a water sample that contained 113-120ppm nitrate and 4-6ppm nitrite, and was then used in the experiments involving the horticulture department and several different types of plants.

In a four week experiment, tomatoes, radishes, and marigolds were split into three different groups that would receive different watering regimens. There were also two phases for this experiment: germination and growth. In the germination phase, five seeds were planted in the soil and allowed to grow for the first two weeks. After this time, all but one plant was removed from the pot. The plant that remained was approximately the average size for that particular pot. For the second two weeks, this one plant was watered and allowed to

Figure 6.13: Plants During the Growth Phase: PP (top), CP (left), PP (right)

grow on its own in the growth phase. The first group of plants (CC) was the control group and was only given tap water throughout the entire experiment. The second group (CP) was given tap water for the germination phase, and then given plasma treated water for the growth phase. The final group (PP) was given plasma treated water for the entire experiment. Figure 6.13 shows how each of the plants were setup for the duration of the experiment. These photos are from the growth phase with the top being the control group, the CP group on the bottom left, and the PP group on the bottom right. For all groups, the plants in the photos are arranged from left to right, radishes, marigolds, and tomatoes. Even from these photos it can be seen that the control group has by far the smaller plant sizes. This is illustrated more so by Figure 6.14 which shows the final size of the plants at the end of the experiment, with radishes on the left, marigolds in the center, and tomatoes on the

right. In both the radishes and the marigolds it is very clear that both the CP and PP groups are much larger than the CC group. It is more difficult to see in the tomatoes as the CC group is almost as tall, but the other two groups were much large when looking at the size and number of leaves on the plants.

Figure 6.14: Comparison of Plant Sizes Between the Experimental Groups

In order to quantify the size differences in the plants, dry weight measurements of both the shoots and the roots of the plants were taken. The plants were removed from the soil and cleaned to remove any remaining soil in the roots. Then the plants were dried out so that the water content in the plant did not contribute to the weight measurements and only the weight of the plant material is recorded. Figure 6.15 and Figure 6.16show the results of these measurements for the shoot and root masses respectively. These are the average of the four

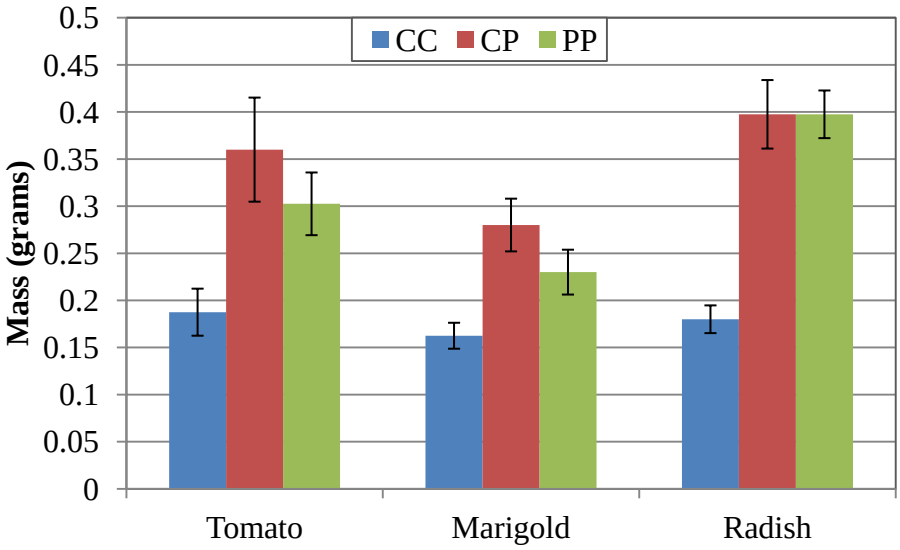

Figure 6.15: Average Shoot Mass for Each Plant Type and Group

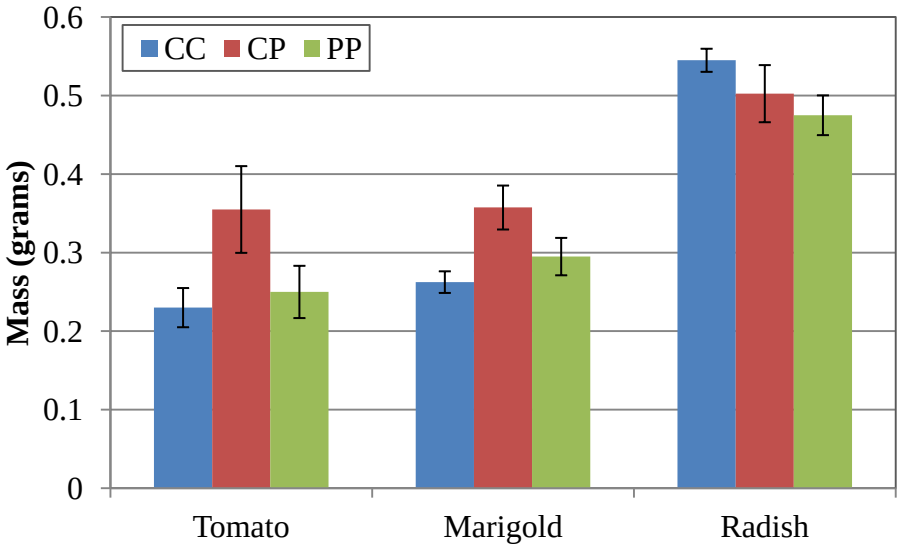

Figure 6.16: Average Root Mass for Each Plant Type and Group

plants for each group and type, and the error bars for the measurements are shown as well. When looking at the shoot mass, it is clear that the plants that have received the plasma

treated water are larger than the control group. Interestingly though the CP which only received the treated water for the last two weeks had more mass than the PP group for the tomatoes and the marigolds, while both groups were identical for the radishes. This leads to the conclusion that the plasma treated water may not be as helpful to the seedlings as it is to more developed plants such as those seen in the growth phase. The data for the root masses behave somewhat differently. The tomatoes and marigolds had similar differences between the three watering regimens with CP having the most mass, although the PP group was only slightly larger than the control group. Radishes had a very different response in the growth of the roots as the control group had the largest root mass, followed by CP and then PP. This is the only measurement where the control group outperformed either of the plasma treated water groups. This indicates that this extra growth tends to occur mainly in the shoots of the radish plants, and the fertilizer can actually have a detrimental effect on the roots. As the plants that had the plasma water during the germination phase are similar in root mass to the control group, it appears that the treated water has a detrimental effect on the growth rate especially during the early germination phase.

It was shown that this plasma device could create an effective fertilizer by exposing water to the air plasma. There is great potential in this, but there are still some serious issues with the device that must be resolved. Efficiency is the greatest challenge with this process. It takes nearly three hours to treat a gallon of water that results in even lower nitrate concentration than in conventional fertilizer water mixtures.

6.2 Chemical Removal

Another potential application of this device is for the removal of chemicals from a water stream. Preliminary results are presented here. This is one of the most promising applications with respect to technical competitiveness and scalability and is discussed extensively in the future work section of this dissertation. There are many industrial chemicals that are found in water waste streams that are difficult to remove using current technology. Two chemicals that are looked at for this device are 1,4 Dioxane and perfluorooctane sulfonic acid (PFOS).

6.2.1 1,4-Dioxane

1,4 Dioxane is an EPA priority pollutant. It can be found in industrial liquid waste and also in some contaminated ground water. It is a widely used solvent for organic compounds, causes liver damage and kidney failure, and has been shown to be a potential carcinogen for humans. Current methods for removal tend to be expensive and time consuming. Therefore there is a great desire to find a new process that would allow for efficient removal of 1,4-Dioxane from water. A method for the degradation of dioxane is through the use of UV and H_2O_2. Photoinduced oxidation occurs when the UV light breaks the bonds of the H_2O_2 to form OH radicals. There is then a series of chemical reactions with the dioxane and its intermediaries with not only the OH radicals but also oxygen and other compounds such as HO_2 [92]. As the plasma generates a significant amount of OH radicals, it presents a potential pathway to an efficient process for the degradation of 1,4-dioxane to less hazardous waste materials. While there are no observed HO_2 lines in the emission spectra, this would be assumed to be created in the same process as in the UV/ H_2O_2 process because there was nothing added to produce this molecule, it was simply a byproduct of the reactions taking place during the degradation. Some experiments have been done for the investigation into the effectiveness of removing 1,4-dioxane from water.

The setup for these experiments is the same as in Figure 6.1 with the plasma being applied to the surface of the water. 500mL sample containing an initial concentration of 377μg/L dioxane were treated for 3min. The input power was set at 420W with an air flow rate of 5 scfm. The samples were then treated for a total time of 26 minutes with several samples being removed throughout the treatment time. It is important to note that each time a sample was removed from the system a total of 40mL was taken. This would reduce the

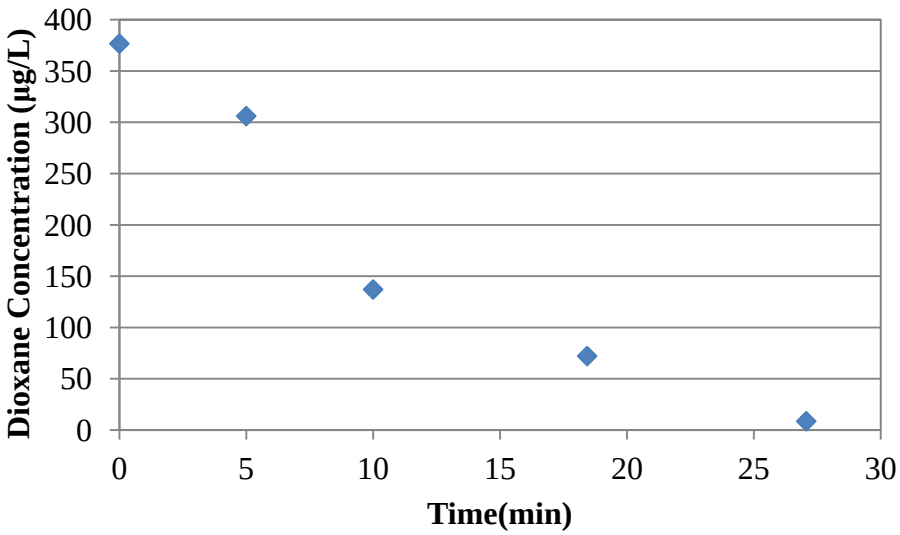

Figure 6.17: Dioxane Concentration after Air Plasma Treatment

overall sample volume and slightly increase the how quickly the dioxane is removed from the system. A total reduction in the amount of dioxane from 377 µg/L to 8.6 µg/L was achieved. While the dioxane was effectively removed from the water the length of time it took was large for a relatively small amount of water. 27 minutes to remove the dioxane would require an enormous amount of energy to scale this to a usable size. Therefore, any attempts to improve this efficiency are necessary. In an attempt to increase the efficiency, other gases were used to quantify their effectiveness in this process. The one gas with the most success is argon. Figure 6.18 compares the argon and air results using the same size initial sample. There are a few differences between the two runs: the argon only had a flow rate 4 scfm, and the delivered power was lower for the argon at around 350W. The argon is much more effective in the removal of dioxane, as the dioxane was completely removed after 5 minutes of treatment time. This result is interesting as OH does not appear to be produced in as great of quantities in the argon discharge as compared to the air discharge. This either indicates that the mechanism for the removal of dioxane when argon is used is not dependant on OH

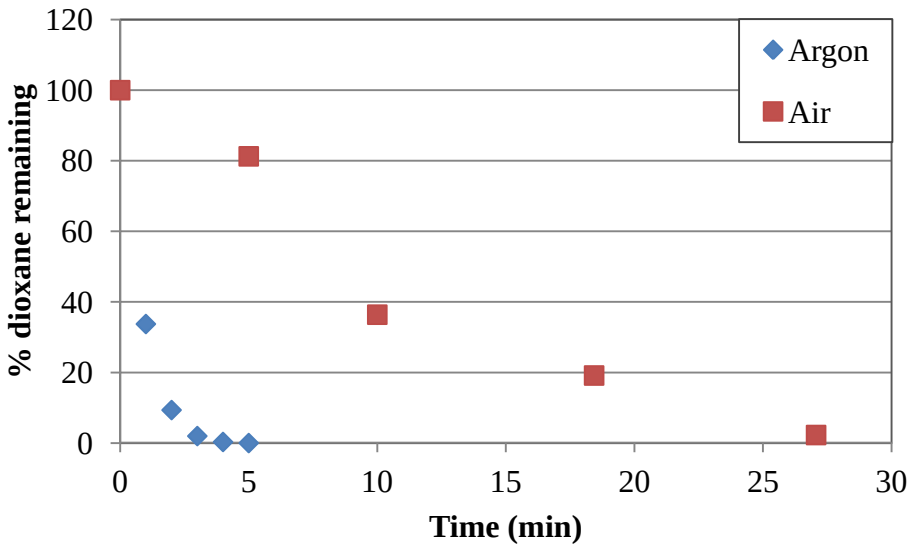

Figure 6.18: Percent of Dioxane Remaining after Treatment for Air and Argon Plasmas

radicals or that OH radicals are being produced via a different pathway. There was also another significant difference in the appearance of the discharges. When air is used, a small cylindrical plasma forms between the surface of the water and the electrode. However, when argon is used the plasma does not stay confined to this small area. It comes out of the tube and fills the space in the beaker with different plasma filaments that are rapidly moving around the device. This is the reason for the difference in power in the two experiments, as the argon plasma created an electrical mismatch. 350W was the most power that could be used while maintaining an acceptable amount of reflected power. Since there was a large volume of plasma, there would be more interaction with the water which would increase the effectiveness of the treatment. Also, this electrical mismatch resulted in large amounts of power being lost into heating the device which also raised the temperature of the sample significantly. An increase in temperature could have caused the degradation reactions to occur more readily increasing the effectiveness of the treatment.

6.2.2 PFOS

PFOS is the one of the resultant products from the waste stream for processes that use Perfluorinated compounds (PFC). These compounds are used for surface treatment agents in fire retardants, paper coatings and carpet cleaners. This widespread use results in these chemicals ending up in the environment. Many of the PFC precursors are degraded naturally to the compounds PFOS and perfluorooctanoic acid (PFOA) and have been detected in the environment. Both of these compounds are a concern as they are toxic to human organs, as well as the reproductive and immune systems. This resulted in PFOS being classified as a persistent organic pollutant. PFOS is difficult to break down due to its strong C-F bonds and most existing degradation processes fail to bread down PFOS. Some examples of current techniques being investigated for the degradation of PFOS include photocatalysis, sonolysis, and chemical oxidation by periodate or persulfate. It is not believed that the OH radical plays any significance into the direct degradation of PFOS; however it has been shown that with the addition of some external energy, the OH radical can effectively degrade PFOS [93]. Some experiments were done to test the effectiveness of this plasma source on the removal of PFOS, as the plasma produces high amounts of OH as well as producing some UV light along with any RF that could be reaching the contaminated water.

Several different experiments were conducted with PFOS using different feed gases including air, argon, and CO_2. Table 6.3 summarizes the results of the PFOS experiments. Two treatment techniques were used; the batch treatment from Figure 6.1 and the side spray technique. The top entries of the table are for the batch water experiment. The first line shows the initial level of PFOS in an untreated sample. There is a min and max listed because there is a 25% error in the measurements of the PFOS concentration. This shows that while there is some minimal removal of the PFOS for air, although it is still within the margin of error, the amount of time it took to reduce a 300mL sample from 31.6μg/L to 20.2 μg/L was 12 minutes which is prohibitively long. CO_2 had slightly worse removal although it did have a smaller ratio of treatment time to volume as the air. Both of these gases have showed that with this type of treatment method they are ineffective at the degradation of PFOS. Argon was the only gas that saw much success with this treatment as the average

amount of PFOS was reduced almost in half with a 400W treatment of a 100mL sample for 3min. It is interesting that argon, as a non reactive gas, once again showed a greater potential for the removal than air. The two lower parts of the table are the results from experiments where the plasma was ran in the device and the water was sprayed in the device, with argon representing the middle part and CO_2 at the bottom. The untreated water was sprayed through the device without a plasma to obtain initial PFOS levels in samples 5 and 8. Then argon was ignited in the device and the water sprayed in and collected at the exit of the device. Sample 6 is for one pass through the plasma and sample 7 is for a second pass through. Once again the PFOS levels are almost reduced in half for the water that passed through the plasma twice. CO_2 essentially had no effect on the PFOS levels when sprayed through the plasma.

Essentially, with the two methods used for water treatment, there was very little effectiveness in the removal of PFOS from the water. While there were some results with the argon plasma, there are some other difficulties with operating this system with argon that would need to be addressed. With the current results, there needs to be a significant change in the method for treating the water that would cause an increase in the degradation of PFOS. Otherwise, this plasma system does not have much potential for the moving forward with this process.

Table 6.3: Summary of PFOS Degradation Experiments

Sample #	PFOS (µg/L)	Min	Max	Experiment Description
1	31.6	23.7	39.5	Untreated; blank
2	16.5	12.375	20.625	Argon, 400W, 100 mL, 4 scfm, 3min
3	24.3	18.225	30.375	CO_2, 420W, 100 mL, 4 scfm, 3min
4	20.2	15.112	25.187	Air 420W 300mL 5.4scfm 12min
5	46.4	34.8	58	Passed Through Sprayer Untreated
6	40.3	30.225	50.375	Argon, 420W, 4 scfm, 1 pass
7	25.2	18.9	31.5	Argon, 420W, 4 scfm, 2 pass
8	26.9	20.175	33.625	Passed through Sprayer, untreated
9	30.5	22.875	38.125	CO_2, 420W, 4 scfm, 1 pass
10	25.4	19.05	31.75	CO_2, 420W, 4 scfm, 2 pass

6.3 Surface Treatment

Plasma surface treatment is a well established application for plasmas. From semiconductor development to textile modifications, plasmas have been used to alter the surfaces of many different materials. This has motivated efforts to identify several different surface treatment applications that can leverage the unique characteristic of this plasma source. Due to the relative high density of this plasma, there should be an opportunity to increase the interaction rates of some of these processes in comparison with other existing technologies used to perform this task. Two main surface treatments applications were explored: the removal of paint from the naval and air force ships and removal of photoresist from silicon wafer. The removal of paint was studied in the greatest detail while there were few experiments involving the photoresist.

6.3.1 Paint Removal

Extensive studies were done in the experimentation with plasma paint removal. These studies also included the use of high density polyethylene (HDPE) as this was has a

similar make up to the bulk of the paint material without many of the other fillers that could pose a problem in understanding the mechanism for paint removal. HDPE has a similar ratio of carbon to hydrogen atoms (1:2) and allows for a simple representation of the paint. Experiments were conducted using both HDPE samples as well as steel samples with actual paint on them.

6.3.2 HDPE Removal

Initial experiments began with HDPE samples. Several 4in squares of HDPE were cut into 1 in squares for the experiments. This allowed for many samples to be used and measured at once. It also allowed for the samples to be inserted into the tube. The device during these experiments only had a long tube on it that resulted in most of the plasma being inside the tube. The location of the electrode was not moved in order to maintain a solid while the plasma was operating. Experiments were simple and only involved weighing the samples with a microbalance before treatment, introducing the samples at varying distances from the plasma, and then once again measuring the mass of the sample. The difference in the two reading would give the total amount removed due to the plasma interaction. Table 6.4 shows the data obtained in these experiments. Exposure time was closely monitored to avoid ignition of the sample during treatment. Prolonged exposure due to slow sample rastering would result in sample melting or combustion. The data is taken for a variety of distances from the electrode, gas flow rates, powers, and exposure times. The final column gives the calculated removal rates of HDPE based on the exposure time and mass difference measured. The entries that do not have a distance were done after the end of the device had been cut off. This data corresponds to the plasma extending out of the device, in contrast to the other samples where the plasma remains inside of the device and the samples are put into the end of the device. All samples were about 2.5cm away from the electrode for these experiments. One of the major difficulties with these experiments was the HDPE tended to ignite for prolonged exposure to the plasma. This seemed to occur more readily when the plasma was inside of the device. This most likely occurs due to the increased gas temperature as the all of the heated gas remains in a small volume. When the end of the

device is removed, the plasma becomes smaller as the gas can diffuse out in all directions and contributes to a drop in gas temperature. Thus, the samples treated outside of the tube were less likely to catch fire.

Table 6.4: HDPE Removal Data

Initial Mass (g)	Distance from Elec (in)	Exposure Time (s)	Flow Rate (scfm)	Power	Final Mass (g)	Mass Difference (mg)	Removal Rate (mg/s)
5.3822	4.5	60	5	560	5.3822	0	0
7.9622	4.5	60	5	630	7.9622	0	0
5.7188	4.5	60	5	595	5.7187	0.1	0.1
5.3822	4.5	60	5	665	5.3821	0.1	0.1
5.35782	2.9	15	4.6	420	5.35777	0.05	0.2
5.382	4	30	5	595	5.3819	0.1	0.2
5.3821	4	30	5	525	5.382	0.1	0.2
5.692	3.6	20	5	420	5.69179	0.21	0.63
7.9591	4.3	15	5	665	7.95893	0.17	0.68
4.1221	3.85	5	4.6	525	4.12203	0.07	0.84
4.12235		10	6	455	4.1222	0.15	0.9
5.64877		10	6	420	5.64849	0.28	1.68
5.35839	3	20	4.8	420	5.35782	0.57	1.71
4.1275	3.1	10	5	420	4.12721	0.292	1.752
7.9623	3.7	30	5	525	7.9606	1.7	3.4
5.6986	4	30	5	595	5.6967	1.9	3.8
3.81462		10	7	490	3.81395	0.67	4.02
5.6967	3.6	15	5	595	5.69486	1.84	7.36
4.1222		5	6	490	4.12158	0.62	7.44
5.3403		10	6	455	5.33873	1.57	9.42
3.82095		10	5	420	3.81462	6.33	37.98

The samples that did ignite had significant amount of material loss, and ended up have very large removal rates. However, this is not a desirable mechanism for removing material, as the plasma is an inefficient method, if the removal is achieved by burning the

sample. As such, the experiments where the samples ignited were not included here. However, by looking at the data in Table 6.4 there is at least some modest removal of material in the absence of thermal conversion. With the maximum removal rate of 37.98mg/s occurring when the plasma could extend out of the device. This occurred surprisingly at the lowest power used in the experiments. These experiments were the most representative of the later process as the plasma would be required to extend out of the device to actually interact with any paint surface. It seems as though airflow and power can have a significant effect on the removal rates with both lower powers and lower air flow rates resulting in higher removal rates.

Understanding the mechanism for removal is important to understand how effective the plasma is at removing material. Initially, it was thought that the reaction with atomic oxygen in the plasma would oxidize the compounds in the paint. In previous work done with a blown arc discharge on the same paint samples, it was determined that there are several other reactions take place that contribute to removal as well [73]. These other reactions include atomic and molecular nitrogen species breaking the CH_2 bonds in the following reactions:

$$N + \left[R - CH_2 - R\right] \rightarrow CN + C_2 + H_2$$
$$N_2^* + \left[R - CH_2 - R\right] \rightarrow CN + C_2 + H_2$$

These reactions occur when the energy of the atomic or molecular nitrogen are high enough that the bonds are broken when collisions occur between the nitrogen and the paint. This indicates that the removal mechanisms would be more due to energy instead of novel chemistry generated in the plasma. Comparison with the gliding arc discharge used in [73] show removal rates much lower for the air treatment. In those experiments a maximum removal was obtained with air of 100mg/s while it averaged around 20-40 mg/s for most settings. The highest removal rate here is at 37mg/s which is similar than the majority of their data. The one large data point was found in [68] at a distance of only 2.5mm from the exit of the device. This is much closer than was attainable here and could contribute to the differences seen in the removal rates

6.3.3 Paint Samples

After reviewing the data from the HDPE experiments and determining the plasma was removing the material, the next step was to begin experiments of actual paint samples. These samples were 4in by 6in steel plates that were coated on both sides with the paint. At this point new end tubes had been made for the device such that the end of the device was close to the electrode, allowing the samples to have direct contact with the plasma. Several techniques for treatments were explored to determine the most appropriate action for treatments. Initially spot testing the samples was done to see how much material was removed, and how it affected the samples. After confirming material was removed, more rigorous tests involving moving the substrate during treatment were performed. This allows for a more consistent treatment time where there is fresh material being removed at any given time. This initially began with simply slowly sliding the samples through the plasma. A significant problem arose during this process though. Although the plasma was able to remove all of the paint and expose the bare metal, once the plasma was exposed to the bare metal surface it would always try to stay in contact with the metal. Figure 6.19 shows and

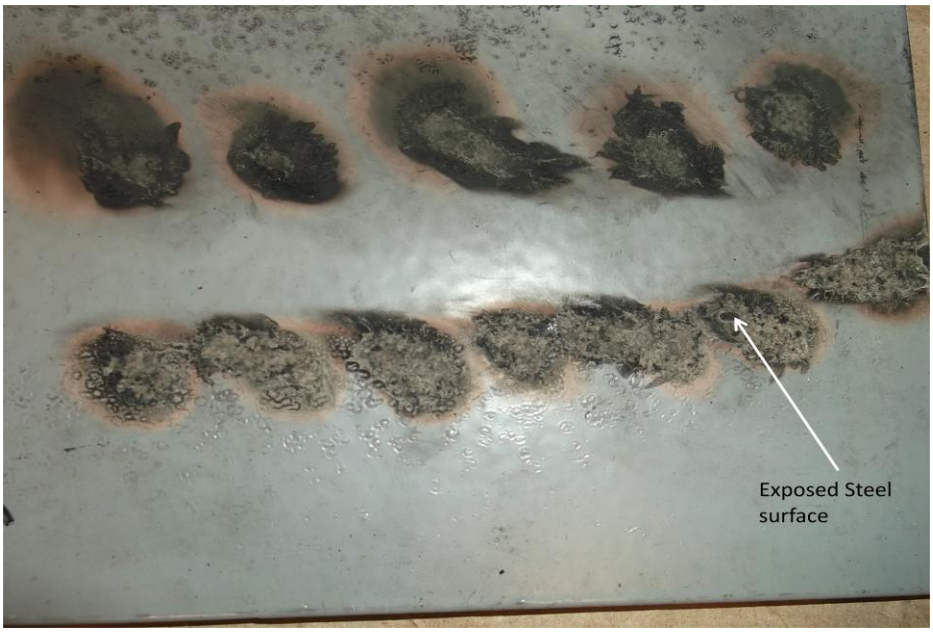

Figure 6.19: Paint Samples Exposed to Plasma

example of a sample of the haze grey freeboard treated by the plasma source. It shows the plasma tends to focus on one point, until it then moves too another point. In the picture one point where there is significant exposure of the steel can be seen. This illustrates how the plasma interacts preferentially with a particular spot on the sample resulting in patches of treated sample instead of one continuous line. In fact the plasma would actually curve to this spot so that even if the original center of the plasma was 1-2 cm away the plasma would still be making contact with the location with some of the paint removed. Although this treatment of just spots occurred most of the time, there were times when a small straight line was able to be produced. This was based on the speed of the sample moving through the plasma coupled with the distance between the sample and the electrode of the device.

As the experiment was conducted by hand, moving the samples at a constant rate was difficult to maintain on a run to run basis. Another noticeable effect on the paint is the charring surround each of the interaction spots. This is due to the high gas temperature of the plasma that exceeded the combustion limit for the surface. As the paint has a similar make up with regards to carbon and hydrogen it is expected to see some thermal damage to the paint. An attempt to remedy this problem was tried using a simple motor spinning the sample while the plasma was interacting. This created a ring of treatment. However, due to the strength of the motor and the weight of the samples it was difficult to maintain a slow and steady speed. A fast speed could be maintained, but it appeared to result in only minimal interaction with the sample. In addition to this, the RF interference in the device caused problems with the motor and caused it to act erratically.

Despite some of these problems, measurements for the amount of material removed were necessary to quantify how efficient this process is and if it is a viable method for the removal of this paint from the steel surface. This experiment was performed by simply turning on the plasma, then placing a sample next to the plasma and slowly pushing it through the plasma. The time the sample was spent in contact with the plasma was recorded. By measuring the weight difference between the samples, a rate for the amount of material removed could be calculated. A variety of parameters were examined to determine how it affected removal rates. Different gases were used to determine if gas chemistry had a

significant impact on removal rates. The gases used in this experiment were air, CO_2, and N_2. Airflow is also considered as this can change the total number of reactive species that could be reaching the sample. There is another set of three parameters that are directly linked. These all correspond to the distance the sample is from the plasma. Figure 6.20 illustrates two of these distances, with the third simply being the sum of the other two. The first distance, ET, is the distance between the electrode where the plasma forms and the end of the device. The second distance is the distance between the end of the device and the surface of the sample. It is important to make this distinction and not just use one of the distances to characterize the interaction. The most obvious shortcoming of using just the distance from the device to the plate is the case where the electrode is recessed from the end of the device. In this case, very little or no plasma was present at the device exit resulting in no interaction between the substrate and the plasma. At this point it could seem like the main parameter to use is the distance between the electrode and the sample is the most important. This is not necessarily the case as these distances affect other aspects of the plasma.

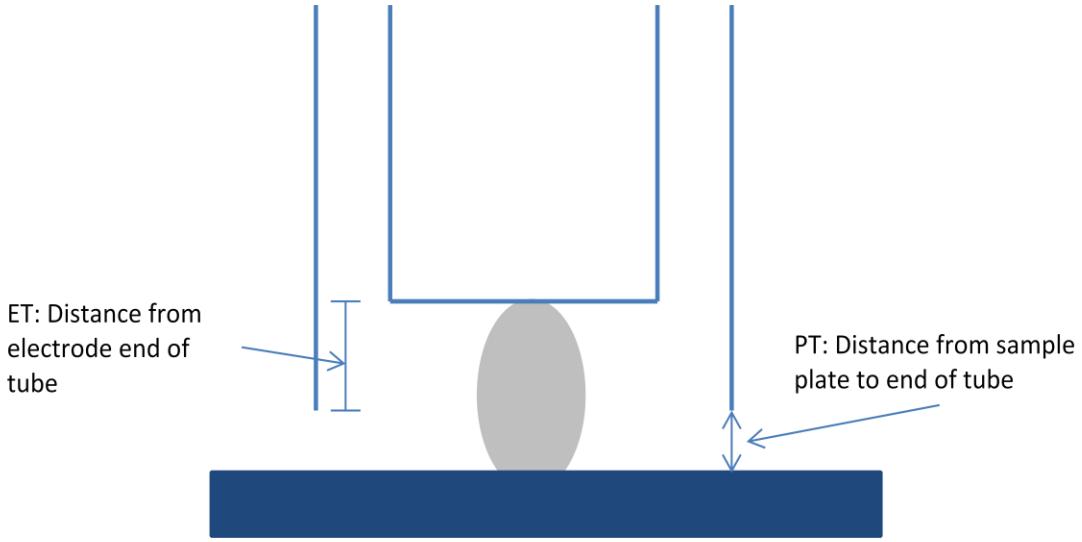

Figure 6.20: Cross Sectional Representation of Plasma Treatment of Sample

An important aspect of this device is that airflow has a very significant effect on the plasma. High airflows can extinguish the plasma while two low causes small plasma to form between the electrode and the side walls. When the electrode is extremely close to the exit the plasma is much smaller and moves around the electrode in an unpredictable fashion. This is mostly due to the air being able to expand in all directions and not being forced to proceed down the tube of the device. This has an effect on the treatment and must then be accounted for. However, any negative effects could be compensated for due to the plasma being denser and having more reactive species closer to the electrode. This is why a combination of these lengths must be examined. The amount of data for each setting is relatively small due to the small number of samples that were available for the experiment. Also, a sample could at most be used for a total of 6 experiments as a fresh clean paint surface was desired for each run resulting in three passes on each side of the sample

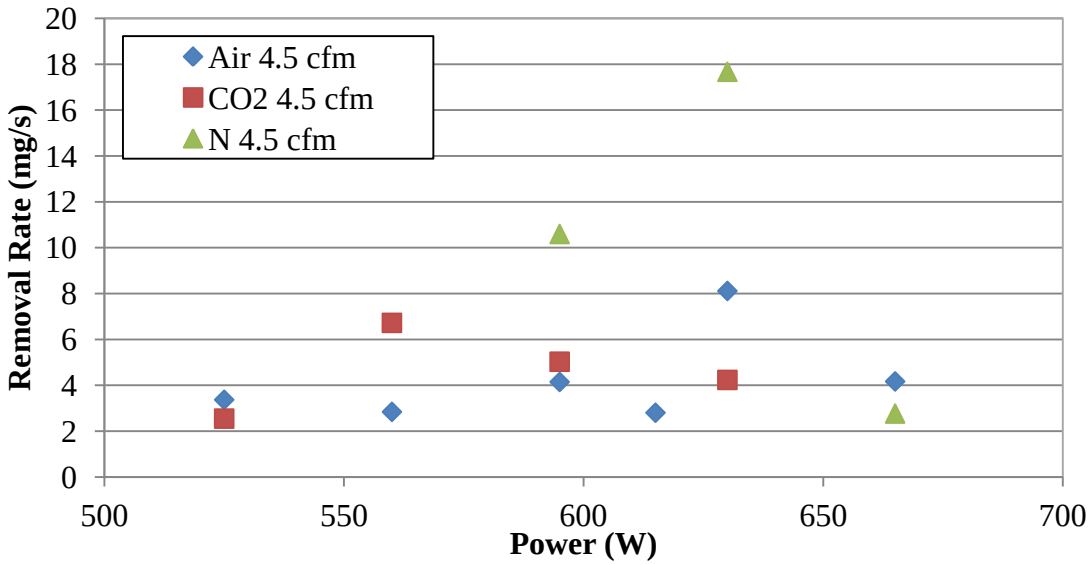

Figure 6.21: Removal Rate of Paint as a Function of Power for Different Gases

Figure 6.21 shows the removal rates for the three gases used in this experiment: Air, Nitrogen, and CO_2. These measurements were made with the plate 1.68 cm from the electrode. While there is significant variation in the total rate recorded here, Nitrogen shows that it has the highest removal rate up to a certain power. Both the air and nitrogen show similar trends even with the significant shift in total removal power. This is expected as air is made up mostly of nitrogen, so the plasmas should behave in similar fashions. However, as the air plasma is fed in with a compressed air line that has significant humidity, the OH peaks dominate the air discharge while they are not seen in the nitrogen discharge. This indicates that the nitrogen species in the discharge are responsible for the removal of the paint, while the OH molecules either contribute nothing or could hinder the process. A peak is reached at an operating power of 630W and the drops of significantly once the power is raised to 665W. This abrupt drop off of the removal rate after 630W is partially due to the phenomenon seen in Figure 6.19. As the power is increased the removal rate still does increase. This allows the plasma to penetrate fully through the paint and then couple to the steel plate. At this point the plasma must be moved significantly away from this spot before it begins to interact with another point on the sample. This caused the plasma to be removing no material for large portions of the time the sample was being moved through the plasma, resulting in the large drop in the removal rate. CO_2 had a slightly different response where it reached a maximum at 560W however it still had a much lower maximum rate than nitrogen.

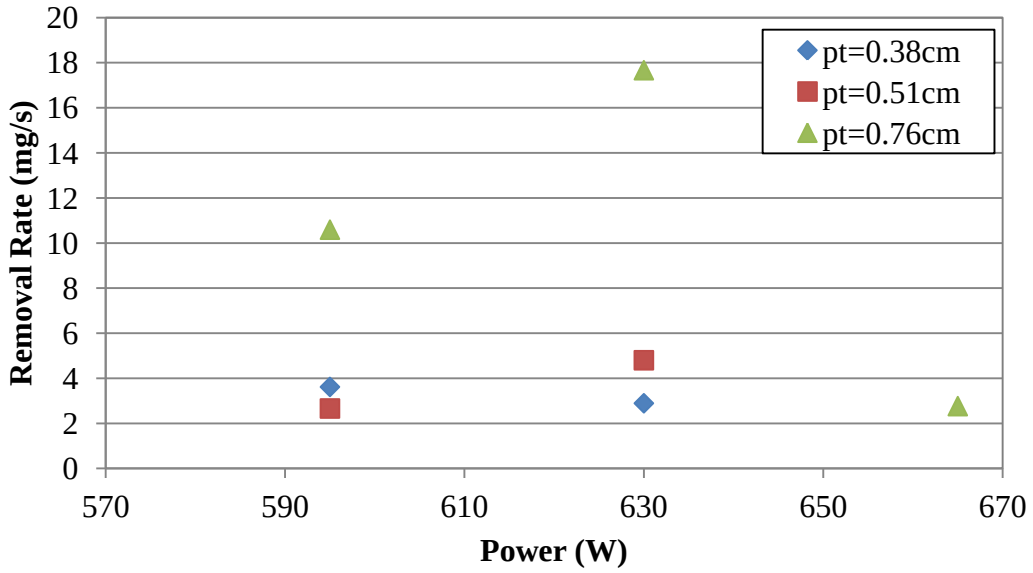

Figure 6.22: Removal Rates for Nitrogen for Various Distances between the Plate and the End of Device

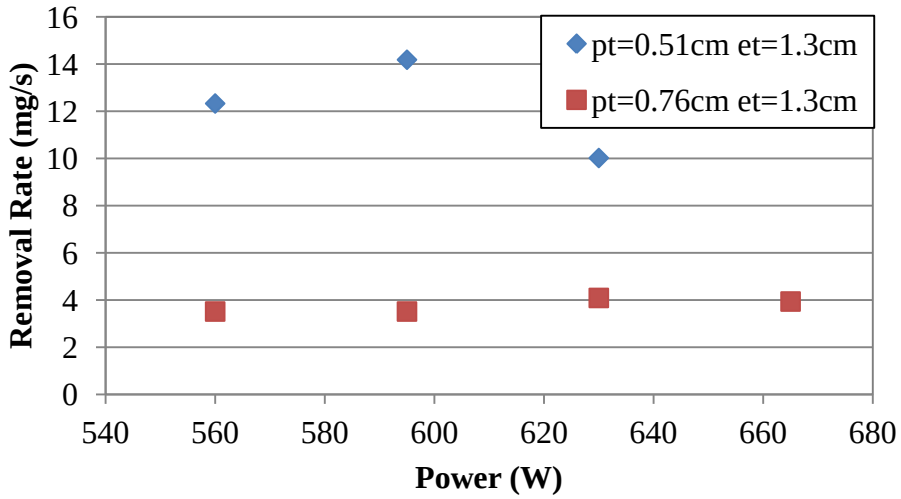

Figure 6.23: Removal Rate for Air for Multiple Distances between Plate and Device

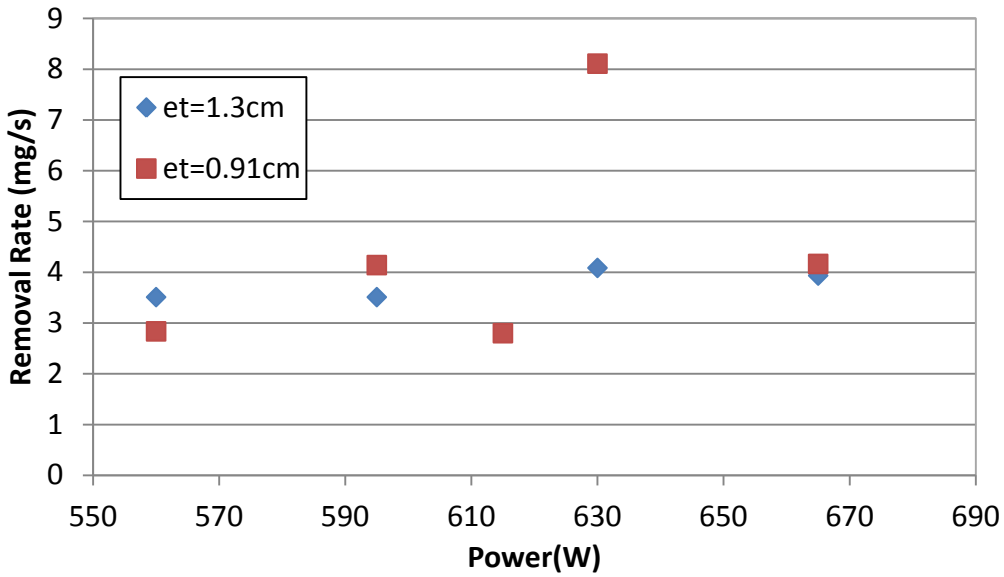

Figure 6.24: Removal Rate for Air at 4.5 scfm with pt=0.76cm and Multiple et Distances

Figure 6.22 shows data for experiments run using nitrogen. In this experiment the distance between the end of the device and the electrode were held constant at 0.89cm while moving the distance between the end of the device and the sample. Interestingly, the best results occurred for the furthest distance. This is most likely due to the closer distances coupling to the plate after quickly removing the paint. This is also supported by the case when the power is increased for pt = 0.76 cm and the removal rate falls to very similar levels as the other distances. Figure 6.23 shows the removal rate for air with the distance et=1.3cm and varying the plate to tube distance. Here it is seen that as the device gets closer, there is an increase in the amount of material removed. This is expected as the sample can then interact with the more active regions of the plasma. Figure 6.24 shows removal rates for air with the distance between the tube and sample constant at 0.76cm while changing the distance from electrode to tube. There is little difference between the two data sets except for the one point at 630W. This is the same power where a maximum was seen before. However, in this case the maximum was not seen when the electrode was too recessed into the tube. This indicates that at some point the total distance from electrode becomes important.

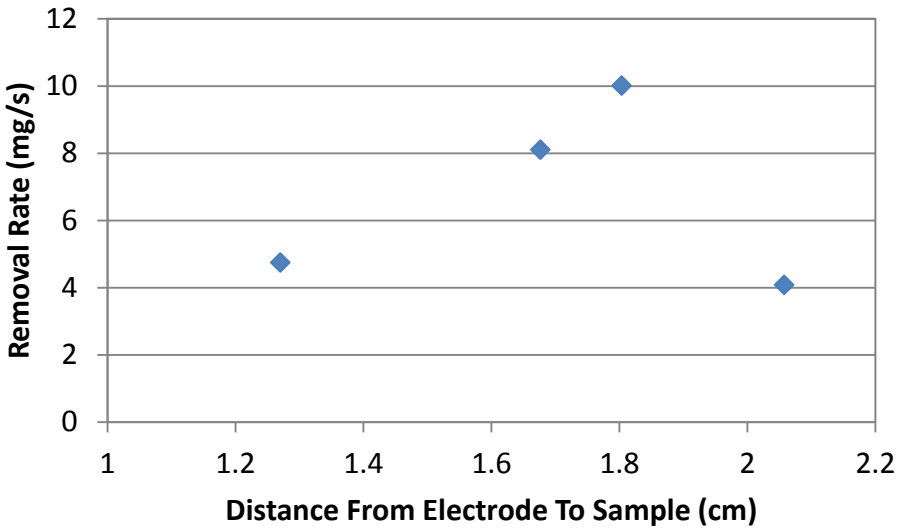

Figure 6.25: Removal Rate vs. Total Distance between Electrode and Sample

Figure 6.25 shows the relationship between the total distance from electrode to sample and removal rates. These experiments were run at 630W, which usually recorded the highest removal rates, with air at 4.5scfm. It shows an increase in removal rate as this distance is increased, until a point where the distance is too large and the most reactive region of the plasma is no longer interacting with the sample. Once again this overall increase in removal with increasing distance could be due to the coupling that occurs at close distances once material has been removed from the surface.

One more parameter to look at is how air flow rates effect the removal of material. For this, three data points were used at 4.5, 5.5, and 6.5 scfm using air. Two input powers were used, 595 and 630W. Figure 6.26 does not give any definitive answer to the effect of air flow rate. There is very little variation in the lower power experiment, and the trends actually tend to do exactly the opposite from one another between the two experiments. This would seem to indicate that air flow rate does not contribute significantly to the removal rate, although a more extensive set of experiments would be necessary to confirm this assessment.

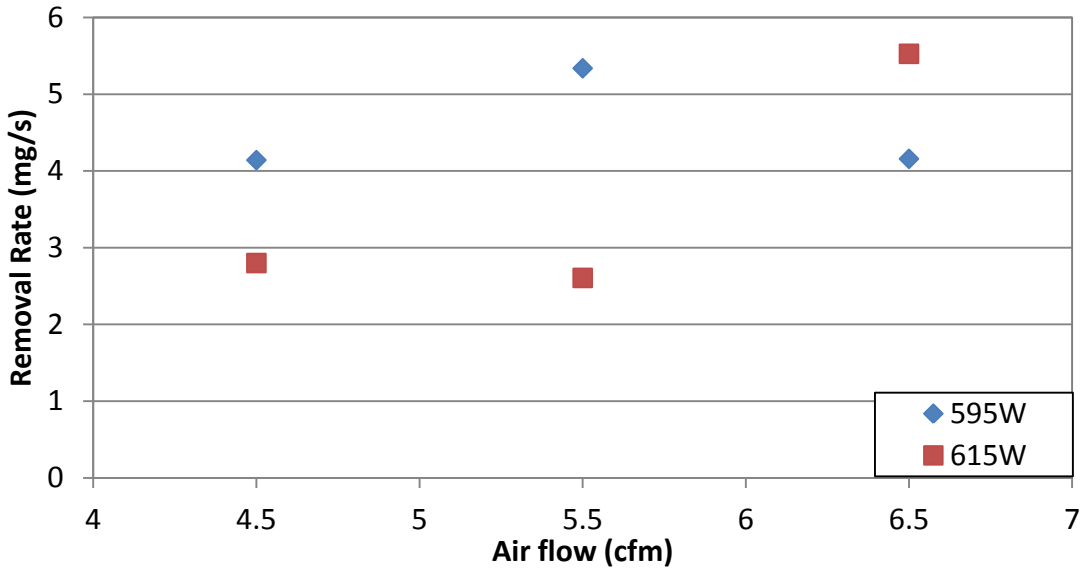

Figure 6.26: Removal Rate for Air with Varying Flow Rate

There is one other important detail to note about these experiments. As these were performed by hand moving the plates manually through the plasma there was a significant amount of variation in the speed at which the plates were moved. Figure 6.27 shows a plot of all the data taken. This includes different gases and distances from the plate. The goal of this figure is to determine how much of an impact movement speed effects the removal rate. Overall the data is spread out with all speeds having at least some points with low removal rate. However, there is still a slight trend where the total removal rate increases with increasing movement speed. This information is highly qualitative and does not give a definitive explanation to how this affects the process, especially since there is the large scattering of data seen in Figure 6.27. This simply illustrates how this parameter which was unable to be controlled tightly would also have an effect when trying to optimize this process. Although it seems that faster is better, there would obviously be a point at which increasing the speed would become detrimental, but this speed was not definitively indicated by this data.

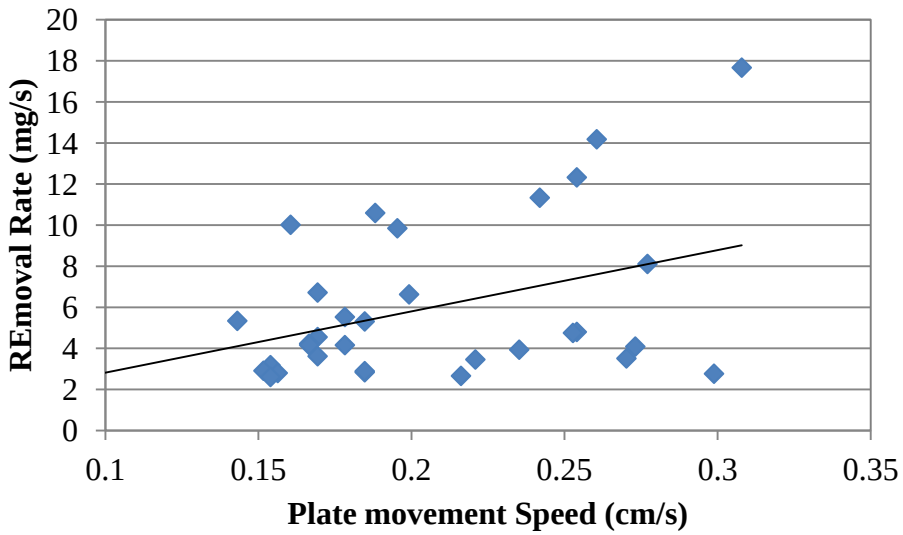

Figure 6.27: Removal Rate vs. Plate Movement Speed

In conclusion, it was shown that this device has the capability to remove paint from the surface of steel. Rates of 17.7mg/s and 14.2 mg/s were obtained using nitrogen and air respectively. These are modest numbers that show some potential in comparison with other technologies as this was in a very early stage of development during these experiments. It was determined that the distance between the plate and the electrode had a significant effect on the removal rate and that an optimum distance near 1.8cm was found. Also moving the plate further from the end of the device had a significant reduction in the effectiveness. This is mainly due to less gas interacting with the plasma and forming fewer molecules responsible for the material removal. There were also some problems, including charring of the material and the affinity for the plasma to interact with the steel once it was exposed. It was unclear if the charring of the paint would have any more effect on the surface of the steel. The plasma interaction with the steel also prevented a large portion of the interaction time with the paint and could cause a significant alteration of the removal rates if this problem was remediated. Furthermore, it was determined that the effects of the plasma that removed the paint were mainly due to physical and thermal effects instead of chemical effects. Therefore, the addition of the plasma added little to benefit to the overall removal of

the paint causing it to not be a superior technique that would improve performance of existing technology.

Chapter 7: Conclusions and Future Work

An atmospheric plasma with the potential for various applications has been developed and investigated thoroughly. The plasma is unique in how the discharge is prevented from transitioning into an arc discharge. The ballasting effect discussed in chapter 3 allows for the stable production of this discharge that is absent of both streamers and arcs. This is driven by the frequency of the generator that causes the plasma impedance to increase while the electron density increases. Having a glow plasma at atmospheric pressure is important for any future applications that may be sensitive to the high energy contained in arcs in some plasma systems. This also allows for a more uniform distribution of electrons, ions and reactive species.

A range of diagnostics was performed to characterize the plasma including OES and electrical measurements. OES allowed for identification of the active species in the plasma as well as estimates for the rotational temperature of the OH molecules in the plasma. Gas identification helps to determine mechanism for different processes in the plasma. This knowledge helps to direct experiments for different applications as the identification of OH molecules sparked ideas for water treatment for dioxane. Similarly, the presence of NO_x species also indicated the potentials for the use of the source in fertigation. Rotational temperatures can be assumed to be close to the actual gas temperature in the plasma and were found to be between 3000K and 5000K. Electrical measurements were done to calculate electron densities on the order of 10^{11}-$10^{13}cm^{-3}$ for the air plasma. Similar densities were calculated for nitrogen and carbon dioxide while there was drop by a factor of 10 for the density of the helium plasma.

Several applications were explored for this device concerning both surface and water treatment. Surface treatment applications included the removal of paint from ships and photoresist from silicon wafers. Only preliminary data was taken for photoresist removal that showed at least comparable removal rates to existing technology. This would be promising due to the lack of expensive equipment necessary for operation except for the effects the plasma had on the wafer. As the plasma has a high gas temperature, the wafers

are heated during treatment, and as soon as the plasma is removed the wafers break from thermal shock. Paint removal was examined more extensively and shown that there was indeed removal of paint from the metal surface of up to 18mg/s. While this was a significant amount, the total value was still below the rates necessary. This fact along with the determination that the mechanism for paint removal was related to the physical energy and not due to the unique chemical conditions presented by the plasma ceased any further investigation to the process.

Water treatment applications have seen a bit more success and further developments are still being considered and worked on. There were two main pathways for applications in water treatment: addition of chemicals, and degradation of existing compounds. The former has received the most attention here in the form of depositing nitrites and nitrates into both tap and distilled water. Repeatable processes that produced 120ppm nitrate water indicate that an industrial type process could be made with consistent output. However, energy use is a significant problem with the cost as it takes approximates 6600 kW-hr to produce a kg of Nitrogen in water. This results in at least a factor of a 100 difference between this and commercial production. As this is only the early steps of developing this technology, it is believed that this difference could be made up but much work would be necessary. Degradation of chemical compounds also saw some limited success. Dioxane was removed almost completely, only about 2% remained, but the treatment time was too long for the sample volume. It does appear that the OH radicals present in the plasma are most likely the cause of this degradation. However, more efficient methods would need to be developed in order to maximize the interaction with the OH radicals as they do not penetrate very far into the water. PFOS degradation had mixed results as there was effectively no removal of PFOS when air was used. There was some removal when using argon but it is still not clear what is causing this degradation. The removal of PFOS from water systems is still in the early stages for most systems that attempt to remove it. Therefore, more efforts to improve upon the results seen as well as an understanding of the removal mechanism will still be pursued in the future.

While the device has been shown to have several different potential applications, none have proven to be definite improvements over existing technology. The most promising of all of the applications is the treatment of water. The device may not be able to handle large enough amounts of water to compete with very large scale water treatment processes, but it has potential in dealing with concentrated volumes of difficult to remove chemicals such as PFOS and dioxane. The largest barrier to this is still efficiency in both the treatment volume and the amount of power used. Currently improvements are being made to the system to try and increase the effectiveness of treatment. Optimization of the process where water is sprayed through the plasma should be done. A process that would allow for greater control over the water flow rate and the characteristics of flow of water out of the spray could be done. This would involve characterizing the both the size and the speed of the water droplets that interact with the plasma to determine what is the most effective for treatment.

Another method for the treatment of water that has just recently had some success is the development of a water electrode. Here the surface of the electrode is actually the water being treated. This allows for the most intense region of the plasma to be in direct contact with the water to increase the interactions responsible for the degradation of any compound in the water. There have been initial tests where the reduction of PFOS in solution with water has been achieved by a factor of 10. These are only preliminary data and must be examined further to determine the mechanism for the degradation of PFOS as well as overall efficiency of the process. This design also allows for continuous delivery through the plasma as well as recirculation. In this design the device points upward to maintain a pool of water on the electrode. A pump then slowly pumps water through the center of the inner conductor which pushes the water slowly over the edges of the electrodes. The water then flows down the center of the device and out the back of the device. The water is the either collected for study or recirculated through the plasma for additional exposure.

Preventing damage to the surface of the electrode is also critical for the further development of the source. Currently with the aluminum electrode, there is significant damage done to the electrode allowing the formation of aluminum oxide in the plasma. This

alters the makeup of the plasma and would have an impact on the effectiveness of any application. The water electrode mentioned previously work as a solution to this as the water on the surface will only evaporate and be replaced with more water from the pump. Other solutions include trying out other materials for the electrode such as brass or titanium. Either the whole electrode or just the surface of the electrode could be made out of these metals as long as there is good electrical contact without gaps that would allow for light up within the electrode. Price of the material would dictate heavily which design to implement.

More work needs to be done to identify the quantities of the different reactive species present in the plasma. While the molecular composition of the plasma was determined through optical emission spectroscopy, these experiments only gave qualitative information. This allows for the knowledge of what is in the plasma but not how much. One major constituent in the plasma is the OH radical. To know the densities of this radical would greatly increase the ability to improve the efficiency of any process relying on the production of this radical. To obtain this information, UV absorption spectroscopy could be used to measure actual OH densities [94]. This would allow a greater understanding of where in the plasma the OH radicals form and help in deciding exactly how to use the plasma in an application. As OH radicals have the highest intensity emission in this plasma, it is assumed that their concentration will be relatively high which is why this would be the first molecule to be experimented with. However, once this has been done, the same techniques, although with different wavelengths of light could be used to determine other potential reactive species that might exist in the plasma such as NO and N_2 [95,96]. Being able to observe the trends in degradation rates compared to the concentrations of different reactive species is a crucial step to determining the actual reaction responsible for the degradation. Ultimately this is the goal of any application experiments as this allows for customization of the plasma to that particular application.

REFERENCES

1 Pappas D 2011 Status and potential of atmospheric plasma processing of materials J. Vac. Sci. Technol. A29 020801

2 Laroussi M 2002 Nonthermal decontamination of biologicalmedia by atmospheric-pressure plasmas: review, analysis, and prospects IEEE Trans. Plasma Sci. 30 1409–15

3 Lerouge S, Wertheimer M R and Yahia L H 2001 Plasma sterilization: a review of parameters, mechanisms, and limitations Plasmas Polym. 6 175–88

4 Fridman G et al 2006 Blood Coagulation and living tissue sterilization by floating electrode dielectric barrier discharge in air Plasma Chem. Plasma Process. 26 425–42

5 Jiang C et al 2009 Nanosecond pulsed plasma dental probe Plasma Proc. Polym. 6 479–83

6 Locke B R et al 2006 Electrohydraulic discharge and nonthermal plasma for water treatment Indust. Eng. Chem. Res. 45 882–905

7 Suchentrunk R et al 1999 Plasma surface engineering—innovative processes and coating systems for high-quality products Surf. Coat. Technol. 112 351–7

8 Chen F Introduction to Plasma Physics and Controlled Fusion 2nd Edn (New York, NY: Plenum Press) 1984

9 Kuo S P, Koretzky E and Vidmar R J 1999 Temperature measurement of an atmospheric-pressure plasma torch Rev. Sci. Instrum. 70 3032–4

10 Schutze A et al 1998 The atmospheric-pressure plasma jet: a review and comparison to other plasma sources IEEE Trans. Plasma Sci. 26 1685–94

11 Bourdet-Mericam N, Laroussi M and Karakas A 2009 Experimental investigations of plasma bullets *J. Phys. D: Appl. Phys*. 42 055207

12 Chirokov A, Gutsol A and Fridman A 2005 Atmospheric pressure plasma of dielectric barrier discharges Pure Appl. Chem. 77 487–95

13 Roth J R, Rahel J, Dai X and Sherman D M 2005 The physics and phenomenology of the one atmosphere uniform flow discharge plasma (OAUGDP™) reactors for surface treatment applications J. Phys. D: Appl. Phys. 38 555–67

14 Al-Shamma'a A I et al 2001 Design and construction of a 2.45 GHz waveguide-based microwave plasma jet at atmospheric pressure for material processing J. Phys. D: Appl. Phys. 34 2734–41

15 Park J, Henins I, Herrmann H W and Selwyn G S 2000 Neutral bremsstrahlung measurement in an atmospheric-pressure radio frequency discharge Phys. Plasmas 7 3141–4

16 Kekez M M, Barrault M R and Craggs J D 1970 Spark channel formation J. Phys. D: Appl Phys. 3 1886

17 Sakiyama Y and Graves D B 2008 Cold atmospheric plasma: charged species and their interactions with cells and tissues IEEE Trans. Plasma Sci. 36 1441–57

18 Starikovskaia S M 2006 Plasma assisted ignition and combustion J. Phys. D: Appl. Phys. 39 R265

19 Lu X P and Laroussi M 2006 Dynamics of an atmospheric pressure plasma plume generated by sub microsecond voltage pulses J. Appl. Phys. 100 063302

20 Staack D et al 2009 Stabilization of the ionization overheating thermal instability in atmospheric pressure microplasmas J. Appl. Phys. 106 013303

21 Heintze M, Zedlitz R and Bauer G H 1993 Analysis of high-rate a-Si:H deposition in a VHF plasma J. Phys. D: Appl. Phys. 26 1781–6

22 Kim J H, et al. Electron density and temperature measurement method by using emission spectroscopy in atmospheric pressure nonequilibrium nitrogen plasmas, *Phys. Plasmas* 13, 093501 (2006)

23 Dong L Direct measurement of electron density in microdischarge at atmospheric pressure by Stark broadening. *Appl Phys Letters* 86, 161501 (2005)

24 Motret O et al. Rotational temperature measurements in atmospheric pulsed dielectric barrier discharge—gas temperature and molecular fraction effects *J. Phys. D: Appl. Phys* 33 (2000)

25 B. Eliasson and U. Kogelschatz, Modeling and applications of silent discharge plasmas *IEEE Trans. Plasma Sci*., vol. 19, pp. 309–323, (1991).

26 Williamson J M et al. Gas temperature determination in a N2/Ar dielectric barrier discharge by diode-laser absorption spectroscopy and resolved plasma emission *J. Phys. D: Appl. Phys* 37 (2004)

27 Kennedy, A. F. a. L. A. Plasma Physics and Engineering. (Taylor & Francis Group, 2011).

28 Wang X et al 2010 Microstructure and initial growth characteristics of nanocrystalline silicon films fabricated by very high frequency plasma enhanced chemical vapor deposition with highly H2 dilution of SiH4 J. Appl. Phys. 107 124313

29 Eliasson, B and Kogelschatz U Nonequilibrium Volume Plasma Chemical Processing, IEEE Trans Plasma Sci, 19, No 6 (1991)

30 E. Neagu, "The influence of annealing time on thermally stimulated discharge current of corona-charged polymers," *Mater. Lett*., vol. 21, 1, pp. 119–125, (1994)

31 Madani M R and Ajmera P K, "Characterization of silicon oxide films grown at room temperature by point-to-plane corona discharge," *J. Electron. Mater*., vol. 22, 9, pp. 1147–1152, (1993)

32 R. W. Smith, D. Wei, and D. Apelian, "Thermal plasma materials processing—Applications and opportunities," *Plasma Chem. Plasma Process*., 9, 1, pp. 135S–165S (1989)

33 Nemchinsky V A, "Dross formation and heat transfer during plasmaarc cutting," *J. Appl. Phys. D*, vol. 30, pp. 2566–2572, 1997.

34 Kim H and Hong S H, "Comparative measurements on thermal plasmajet characteristics in atmospheric and low pressure plasma sprayings," *IEEE Trans. Plasma Sci*. vol. 23, pp. 852–859, Oct. 1995.

35 Jeong J Y et al, “Etching materials with an atmospheric-pressure plasma jet,” *Plasma Source Sci. Technol.*, vol. 7, no. 3, pp. 282–285, (1998)

36 Walsh J L, Kong M G Contrasting characteristics of linear-field and cross-field atmospheric plasma jets. *Applied Physics Letters* 93, 111501 (2008)

37 Xi Min et al Surface modification of aramid fiber by air DBD plasma at atmospheric pressure with continuous on-line processing *Surface and Coatings Tech*. 202 (2008)

38 Park J et al Discharge phenomena of an atmospheric pressure radio-frequency capacitive plasma source *J. Appl. Phys*. 89 20 (2001)

39 Gonzalez-Aguilar J et al A Theoretical Study of a Cutting Air Plasma *IEEE Tran on Plasma Sci.* 27 1 (1999)

40 Moisan M et al Low-temperature sterilization using gas plasmas: a review of the experiments and an analysis of the inactivation mechanisms *Int J of Pharmaceutics* 226 (2001)

41 Kogelschatz U, “Advanced ozone generation,” in Process Technologies for Water Treatment, S. Stucki, Ed. New York and London: Plenum, 1988, pp. 87-120.

42 Deryugin A et al Ozone Production and de-NOx Modeling in Dry Air Electrical Discharges Plasma Chemistry and Plasma Processing, 17, 1 (1997)

43 E. Garate, K. Evans, O. Gornostaeva, I. Alexeff, W. Kang, M. Rader, and T. K. Wood, “Atmospheric plasma induced sterilization and chemical neutralization,” Proc. IEEE Int. Conf. Plasma Science, p. 183, June 1998.

44 W. P. Menashi, “Treatment of surfaces,” U. S. Patent 3 383 163, 1968

45 Kogelschatz, U. "Atmospheric-pressure Plasma Technology." *Plasma Physics and Controlled Fusion* 46.12B (2004): B63-75.

46 Bakken, J. A. "High Temperature Processing and Numerical Modelling of Thermal Plasmas in Norway." Pure and Applied Chemistry 66.6 (1994): 1239-246

47 Lelievre, J., N. Dubreuil, and J.-L. Brisset. "Electrolysis Processes in D.C. Corona Discharges in Humid Air." Journal De Physique III 5.4 (1995): 447-57.

48 Locke, B. R., M. Sato, P. Sunka, M. R. Hoffmann, and J.-S. Chang. "Electrohydraulic Discharge and Nonthermal Plasma for Water Treatment." Industrial & Engineering Chemistry Research 45.3 (2006): 882-905.

49 Traylor, M. J., Pavlovich, M. J., Karim, S., Hait, P., Sakiyama, Y., Clark, D. S., and Graves, D. B. (2011). "Long-term antibacterial efficacy of air plasma-activated water." Journal of Physics D: Applied Physics, 44(47), 472001.

50 Kishimoto N et al. Applicability of Ozonation Combined with Electrolysis to 1,4-Dioxane Removal from Wastewater Containing Radical Scavengers *Ozone: Science and Engineering*, 29 13-22 (2007)

51 Nakanishi, J., R. Makino, H. Kawasaki, A. Kishimoto, and M. Gamo, 1,4-Dioxane (Tokyo, Japan: Maruzen, 2005) (in Japanese).

52 DeWalle, F.B. and E.S.K. Chian, ''Detection of Trace Organics inWell Water Near a Solid Waste Landfill'', *J. AWWA*, 73:206–211(1981).

53 Abe, A., ''Distribution of 1,4-Dioxane in Relation to Possible Sources in the Water Environment'', *Sci. Total Environ*., 224:41–47 (1999).

54 Klecˇka, G.M. and S.J. Gonsior, ''Removal of 1.4-Dioxane from Wastewater'', *J. Hazardous Materials*, 13:161–168 (1986).

55 Gmehling, J. and U. Onken, Vapor-Liquid Equilibrium Data Collection Aqueous-Organic Systems, *Chemistry Data Series*, Vol. 1, Part 1 (Frankfurt, Germany: Dechema, 1977).

56 Galloway J N and Cowling E B Reactive Nitrogen and the World: 200 Years of Change *AMBIO: A Journal of the Human Environment*, 31(2):64-71. (2002)

57 Smil, V. 2001. Enriching the Earth. The MIT Press, Cambridge, MA. 338 pp

58 Jenkinson D S The impact of humans on the nitrogen cycle, with focus on temperate arable agriculture *Plant and Soil* 228: 2-15 (2001)

59 Dawson C J and Hilton J Fertiliser availability in a resource-limited world: Production and recycling of nitrogen and phosphorus. *Food Policy* 36 S14-S22 (2011)

60 Vecitis C D et al Treatment technologies for aqueous perflluorooctanesulfonate (PFOS) and perfluorooctanoate (PFOA) *Frontiers of Environmental Science & Eng in China* Vol 3, 2 (2009)

61 Ahrens L et al Polyfluorinated compounds in waste water treatment plant effluents and surface waters along the River elbe, Germany *Marine Pollution Bulletin* 58 1326-1333 (2009)

62 Sundstrom D W, Klei H E. Wastewater Treatment. Englewood Cliffs: Prentice-Hall, 1979

63 Key, B. D et al Defluorination of organofluorine sulfur compounds by Pseudomonas sp. Strain D2. Environ. Sci. Technol. 32, 2283–2287 (1998).

64 Schultz, M. M et al Fluorochemical Mass Flows in a Municipal Wastewater Treatment Facility.Environ. Sci. Technol. 40 (2006)

65 Cheng J et al Sonochemical Degradation of Perfluorooctane Sulfonate (PFOS) and Perfluorooctanoate (PFOA) in Groundwater: Kinetic Effects of Matrix Inorganics *Environ. Sci. Technol.* 44, 445-450 (2010)

66 Schweitzer P A Paint and Coating: Applications and Corrosion Resistance (Taylor & Francis Group, LLC, 2006)

67 Bill Ross, J. B., Chris Fromme. A Semi-Autonomous Robot for Stripping Paint from Large Vessels. The International Journal of Robotics Research 22, 617-626 (2003).

68 Alan Echt, K. H. D., and R. Leroy Mickelsen. Automated Abrasive Blasting Equipment for Use on Steel Structures. Applied Occupational and Environmental Hygiene 15, 713-720 (2000).

69 Beth Rosenberg, L. Y., Scott Fulmer. Ergonomics of abrasive blasting: A comparison of high pressure water and steel shot. Applied Ergonomics 37, 659-667 (2006).

70 (ISO), I. O. f. S. in Part 4: Types of surface and surface preparation 22 (ISO, Geneve, Switzerland, 1998).

71 Momber, A. Colour-based assessment of atmospheric corrosion products, namely of flash rust, on steel. Materials and Corrosion 61, 1-10 (2010).

72 in Detailed Specification: Paint, Epoxy-Polyamide, General Specification For (2009).

73 McWilliams, A Characterization of Atmospheric Pressure Plasma Torch and the Surface Interaction for Material Removal (2012)

74 Institution, W. H. O. & Ships, U. S. N. D. B. o. Marine Fouling and Its Prevention. Vol. Chapter 1 (George Banta Publishing Co., 1952).

75 Godyak V A 1986 Soviet Radio Frequency Discharge Research (Falls Church, VA: Delphic Associates Inc.)

76 McKay K, Iza F and Kong M G 2010 Excitation frequency effects on atmospheric-pressure helium RF microplasmas: plasma density, electron energy and plasma impedance Eur. Phys. J. D 60 497–503

77 Vidmar R On the Use of Atmospheric Pressure Plasmas as Electromagnetic Reflectors and Absorbers *IEEE Trans. Plasma Sci.* 18, 4 (1990)

78 Laux C O et al 2003 Optical Diagnostics of Atmospheric Pressure Air Plasmas Plasma Sources Sci. Technol. 12 125-138

79 Pozar D 2005 Microwave Engineering 3rd edn (Hoboken, NJ: John Wiley & Sons Inc)

80 Steer M 2013 Microwave and RF Design A systems Approach 2nd edn (Edison, NJ: SciTech Publishing)

81 Madsen M. J. et al Measuring the Molecular Polarizability of Air *American Journal of Physics* 79, 428 2011

82 Lieberman M A and Lichtenberg A J 2005 Principles of Plasma Discharges and Materials Processing 2nd edn (Hoboken, NJ: Wiley Interscience)

83 Mamen J et al Spectral Structure of the Aluminum Dust Flame 20th *International Colloquium of the Dynamics of Explosions and Reactive Systems* (2005)

84 Zhang S and X-W Hu 2005 New Microwave diagnostic theory for measurement of electron density in atmospheric plasmas Chin. Phys. Let. 22 168

85 Dorn H P et al Investigation of OH absorption cross sections of rotational transitions in the $A^2\Sigma^+$,υ'=0 $X^2\Pi$, υ"=0 band under atmospheric conditions: Implications of tropospheric long-path absorption measurements *J Geophys Res.* 100 NO. D4 (1995)

86 Garamoon A A and El-Zeer D M 2009 Atmospheric pressure glow discharge plasma in air at frequency 50 Hz Plasma Sources Sci. Technol. 18 045006

87 Park J, Henins I, Herrmann H W and Selwyn G S 2001 Discharge phenomena of an atmospheric pressure radio-frequency capacitive plasma source J. Appl. Phys. 89

88 Aguilera J A and Aragon C A comparison of the temperatures and electron densities of laser-produced plasmas obtained in air, argon, and helium at atmospheric pressure *Appl. Phys. A* 69

89 Beegle L W et al Effects of drift-gas polarizability on glycine peptides in ion mobility spectrometry *Int J. Mass Spectrometry* 216 3 257-268 2002

90 Y Liang *et al* 1994 High harmonic generation in atomic and diatomic molecular gases using intense picosecond laser pulses-a comparison *J. Phys. B: At. Mol. Opt. Phys.* **27** 5119

91 Poulsen R. G. 1977 Plasma etching in integrated circuit manufacture—A review *J. Vac Sci. Technol*. 14 266 S475-S478 1999

92 Stefan M AND Bolton J 1998 Mechanism of the Degradation of 1,4-Dioxane in Dilute Aqueous Solution using the UV/Hydrogen Peroxide Process *Environ. Sci. Technol.* 32 1588-1595

93 Tang H et all 2012 Efficient degradation of perfluorooctanoic acid by UV–Fenton process *Chemical Engineering Journal* 184 156-162

94 Hibert C et al 1999 [OH (X)] measurements by resonant absorption spectroscopy in a pulsed dielectric barrier discharge *J. Apply. Phys*. 85

95 Pipa A V et al 2008 Absolute production rate measurements of nitric oxide by an atmospheric pressure plasma jet (APPJ) *J. Apply. Phys*. 41

96 Babayan S.E. et al 2002 Characterization of the Active Species in the Afterglow of a Nitrogen and Helium Atmospheric-Pressure Plasma *Plasma Chem and Plasma Process* 22 255-269